POLYTECHNIC OF TURIN

College of Chemical and Materials Engineering

Master of Science Course in Materials Engineering for Industry 4.0

Master of Science Thesis

Microstructural Optimisation of a Ni-based Superalloy through an Integrated HIP-Quenching Route and Quantitative Grain Boundary Serration Analysis

Thesis supervisor:
Prof. Daniele Ugues
Prof. Emilio Bassini

Candidate:
Federico Cotti Paltro

March 2026

1. Introduction 6
1.1. Ni-based superalloys 7
1.1.1. Strengthening mechanism 8
1.1.2. Solid solution strengthening 9
1.1.3. Precipitation Hardening 10
1.1.4. Coherency and misfit stresses at the γ/γ′ interface 13
1.1.5. Other second phases 14
1.1.6. Grain boundaries 15
1.2. Additive Manufacturing Technology (LB-PBF) 19
1.3. HIP 21
2. Materials and Methods 26
2.1. SAM and heat treatment strategy 26
2.2. Metallographic preparation of samples 27
2.3. Optical Microscope analysis 27
2.4. Scanning Electron Microscopy (SEM) 28
2.5. Grain Boundary Roughness Evaluation Method 28
2.6. Grain Size Analysis 30
2.7. Gamma prime (γ′) volume fraction analysis 30
2.8. Hardness Test using Brinell scale 31
3. Results and discussion of SAM 34
3.1. DSC of As-Built SAM sample 34
3.2. Microstructural evaluation of SAM As Built 35
3.3. Microstructural analysis of standard Hipped samples 36
3.3.1. Samples HIP treated -100MPa-20°C/min 37
3.3.2. Samples HIP treated -150MPa-20°C/min 53
3.3.3. HIP-treated samples at 100 MPa vs 150 MPa -20 °C/min 66
3.3.4. Samples HIP-Quench treated 100MPa – 120 °C/min 68
3.4. Formation mechanism of SGBs 80
3.5. Completion of the heat treatment 83
4. Conclusion 91

Abstract

In this work, an innovative heat treatment process was investigated for a nickel-based superalloy, which is manufactured by Laser Powder Bed Fusion (PBF-LB). Alloys requires Hot Isostatic Pressing (HIP) as a post-processing step, which involves the simultaneous application of high temperature and high isostatic gas pressure. Typically need the following heat treatments (such as annealing or aging) to be performed in a separated low- pressure furnace. In contrast, the new approach, here explored, allows to run the HIP and solution treatment within a single processing stage in a single furnace. The aim is to significantly reduce the overall processing time and production costs by combining the healing effect of HIP and the most expensive heat treatment i.e. the solution annealing. The initial focus of the experimental investigation was based on three super solvus temperatures combined with two different pressure levels, namely 100 MPa and 150 MPa, at a cooling rate of 20 °C/min. Microstructural characterization revealed that in spite of marginal improvements in densification and microstructural homogeneity, promoted by higher pressure, the increased processing costs were not justified by the benefits.

Consequently, following experiments were conducted exclusively at 100 MPa, keeping the same temperature conditions while increasing the cooling rate to 120 °C/min in order to assess its influence on microstructural evolution. Through the development of a semi-automated image study method, a detailed microstructural analysis was performed for all processing conditions, including porosity evaluation, grain morphology assessment, and quantitative characterization of grain boundary serration. Grain boundary serration refers to the formation of tortuous boundary paths, which is a highly desirable morphological feature because it physically inhibits grain boundary sliding, resulting in a significant improvement in high-temperature creep resistance of nickel-based superalloys. By means of this approach it was possible to systematically evaluate grain boundary morphology, which is directly related to the creep resistance of nickel-based superalloys. The results highlighted a progressive reduction in grain boundary serration with increasing cooling rate. After HIP-quenching the samples an aging process at different temperatures was applied. The combined analysis of γ' phase volume fraction and hardness measurements enabled the identification of the optimal aging condition resulting in the most favourable microstructural configuration. In conclusion, it was demonstrated that the HIP-quenching approach represents a promising and efficient alternative to conventional multistep heat treatment processes for additively manufactured superalloys. The application of this route leads to a significant reduction of processing times, as well as to the production of a much finer microstructure compared to traditional methods. This microstructural refinement represents a strong encouragement for the adoption of the integrated route, as it can further enhance the material's high-temperature strength by means of a more effective interaction between the γ' precipitates and dislocations.

1. Introduction

Superalloys are distinguished from other metallic materials by their ability to exhibit high strength, good fatigue and creep resistance, excellent corrosion resistance and the capacity to operate at elevated temperatures for extended periods. They were developed during the Second World War and in the early 1950s in order to withstand the service temperatures in the hot sections of jet turbine engines, which austenitic stainless steels could no longer tolerate. These hot sections (blades, vanes and combustion chambers) represent more than 50% of the total engine weight. With the introduction of new compositions and processing techniques, new generations of superalloys were created, finding applications from aerospace and power generation to specialised sectors like motorsport. [1] Their most notable features include maintaining high mechanical strength near their melting point, typically up to 80% of the absolute melting temperature. They also possess excellent resistance to hot corrosion and oxidation, making them ideal for high-temperature applications up to 1000°C. Therefore, thanks to their combination of high mechanical strength, long-term microstructural stability, and tolerance to severe operating environments, superalloys are indispensable in the hottest and most stressed regions, when the material integrity being crucial for both safety and efficient system operation.[2] In these applications, it is necessary to favour not only a ductile and resistant structure to avoid brittle fracture, but also one that exhibits good behaviour under high-temperature deformation. The creep shear strain rate $\dot{\gamma}$ shows an Arrhenius-type dependence on temperature, proportional to the volume diffusivity, of activation energy Q_v and the pre-exponential term $D_{0,v}$.

$$\dot{\gamma} \propto D_{0,v} \exp\left\{-\frac{Q_v}{RT}\right\} \tag{1.1}$$

Consequently, the crystalline structure with low diffusivity and a high activation energy value is beneficial for creep behaviour. Given these considerations, the crystalline structure most suitable for use as the matrix is the face-centred cubic (FCC) structure, as shown in Figure 1.1.[3]

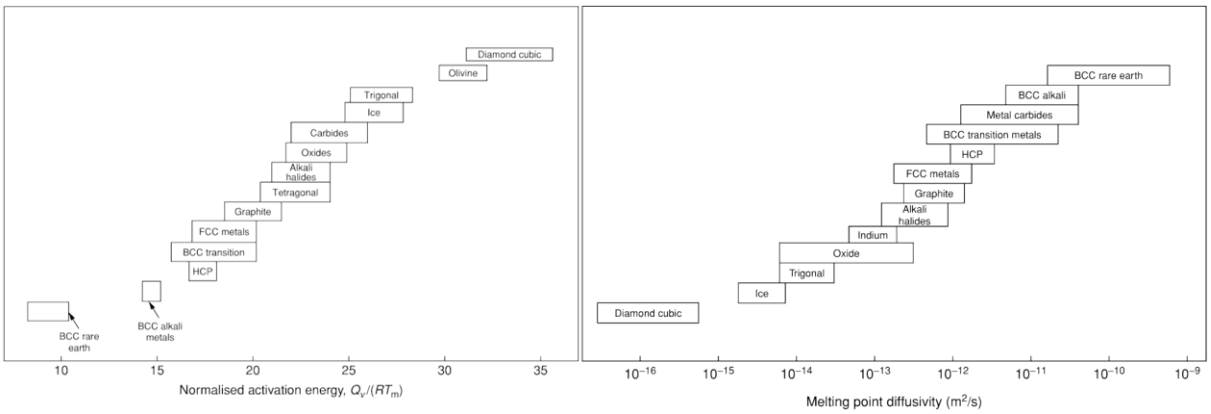

Figure 1.1: Comparison of diffusion properties across different crystal classes: normalised activation energy for diffusion Q_v/RT_m(left) and diffusivity at the melting point (right), both as a function of crystal structure.[3]

The three major classes of superalloys are:

- Ni-based superalloys.
- Ni-Fe-based superalloys.
- Co-based superalloys.

The common feature in these alloys is their FCC crystal structure, also called the gamma phase (γ). Ni-based alloys can remain stable in the FC structure from room temperature to the melting point. In contrast, the structures of pure iron and cobalt have different allotropy transformations. [2] Pure cobalt at room temperature exhibits a hexagonal close-packed (HCP) structure and transforms into a face-centred cubic (FCC) structure at temperatures above 780 °C. However, the addition of alloying elements is used to stabilise the FCC austenitic structure between room temperature and the melting point. Nevertheless, the absence of precipitates in these alloys prevents a significant increase in strength, making them less desirable than nickel-based alloys for high-load applications. Because of their higher melting point, they can operate at higher temperatures under moderate stress, boasting very high resistance to oxidation and hot corrosion. Given these characteristics, hey are used for static, low-stress parts such as combustion chambers [1]. To increase the mechanical properties and corrosion resistance of Fe-based alloys, quantities of Ni exceeding 20% by weight are added, increasing the expansion of the austenitic phase range and stabilizing it at room temperature. Furthermore, the addition of Cr allows the formation of a passivating Cr_2O_3 oxide layer that provides greater protection, significantly improving the alloy's resistance to oxidation at high temperatures. Although Fe-based alloys cannot match the thermal stability and oxidation resistance of Ni- and Co-based alloys, iron remains desirable int terms of cost reduction. Consequently, nickel-base superalloys are widely used in the most demanding applications, such as hot gas path components in land-based and aeronautical gas turbines, because they outperform other superalloy classes.[1]

1.1. Ni-based superalloys

Nickel is a metallic chemical element, belonging to group VIII of the fourth period, with a density at ambient conditions of 8.907 g/cm³. The crystal structure of nickel is face-centred cubic as shown in Figure 1.2. Unlike iron and cobalt, it does not exhibit allotropic transformations. It maintains a face-centred cubic structure, stable from room temperature up to its melting point at 1455 °C, which represents a practical upper limit to the usable service temperature for the superalloys. Nickel is the main component of the matrix, not only for its ductility and toughness but also for the ability to solubilise a wide variety of alloying elements. In particular, the continuous matrix, known as γ, is an austenitic phase (FCC) that typically contains a high concentration of solid solution elements. Nickel-based alloys can be strengthened through solid solution mechanisms for lower-temperature applications or through precipitation hardening for higher-temperature uses. In the latter case, hardening results from the precipitation of second phases. Therefore, stability of the second-phase morphology, grain structure, and the distribution of particles such as carbides and borides are essential for preserving the exceptional properties of these alloys under severe operating conditions. [4]

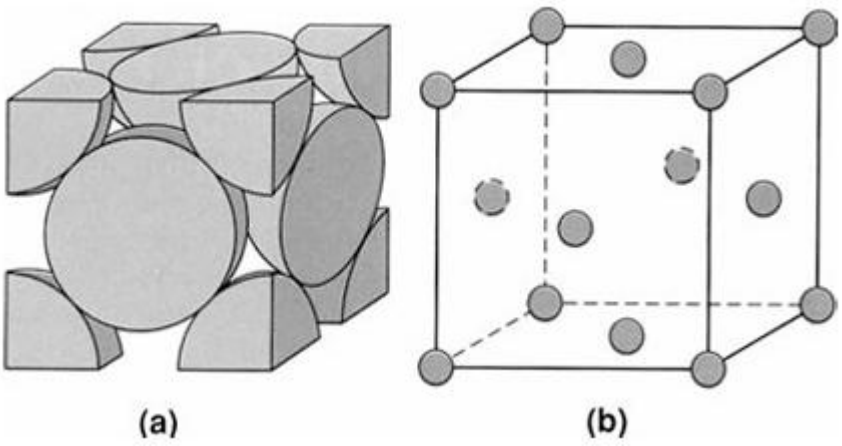

Figure 1.2: Crystal structure of Nickel: (a) close-packed atomic arrangement represented by spheres; (b) schematic representation of the face-centered cubic (FCC) unit cell. [3]

1.1.1. Strengthening mechanism

The development of Ni-based superalloys for critical applications requires the understanding of their chemical composition to optimise mechanical strength and long-term creep resistance. The improvement of the mechanical and thermomechanical properties of these superalloys results from the synergistic interaction of multiple strengthening mechanisms: (i) solid solution strengthening of the FCC matrix; (ii) precipitation-hardening through intermetallic γ' Ni_3 (Al, Ti) and/or γ'' Ni_3 (Nb) phases; (iii) coherency and misfit stresses at the γ/γ' interface; (iv) grain boundaries conformations and the introduction of stable carbides and borides. Owing to these reinforcement mechanisms, alloying elements can perform various functions, such as dissolving into the γ matrix, inducing precipitation of secondary intermetallic phases, forming carbides or borides, or passivating the surface. Additionally, the same element can perform several of the roles just mentioned simultaneously. Therefore, even if these superalloys are composed of only a few phases, their overall composition remains highly complex. Table 1.1. Understanding the relationship between chemical composition, microstructure, and high-temperature performance is crucial for designing new-generation superalloys with enhanced high-temperature performance.[4]

Table 1.1: Effects of alloying elements on the microstructure and mechanical properties of γ′-strengthened Ni-based superalloys.[2]

Effect	Alloying elements
Solid-solution strengtheners	Co, Cr, Fe, Mo, W, Ta, Re
Carbide form:	
MC	W, Ta, Ti, Mo, Nb, Hf
M_7C_3	Cr
$M_{23}C_6$	Cr, Mo, W
M_6C	Mo, W, Nb
Carbonitrides: M(CN)	C, N
Forms γ' Ni_3 (Al, Ti)	Al, Ti
Raises solvus temperature of γ'	Co
Hardening precipitates and/or intermetallics	Al, Ti, Nb, Ta
Oxidation resistance	Al, Cr, Y, La, Ce
Improve hot corrosion resistance	La, Th
Sulfidation resistance	Cr, Co, Si
Improves creep properties	B, Ta
Increases rupture strength	B
Grain-boundary refiners	B, C, Zr, Hf
Retard γ' coarsening	Re

1.1.2. Solid solution strengthening

Elements such as Cr, Co, Mo, W, and Re tend to partition into the γ matrix, which enhances the mechanical properties of Ni-based superalloys by inducing solid-solution strengthening and thermomechanical behaviour. In addition, these elements decrease the stacking fault energy, which represent the energy required to form a partial dislocation per unit area. Low values of this energy increase the width of the stacking fault, limit the mobility of dislocations within the γ matrix, make it more difficult to change slip planes, and consequently favour creep resistance. Moreover, solid-solution strengthening arises from the presence of solute atoms in the γ matrix, since these elements have atomic sizes that can differ by up to 28% from nickel. As a consequence, lattice distortions caused by foreign atoms locally perturb the elastic field and generate pinning forces on dislocations. [5] In this situation, the contribution of solid solution strengthening to the mechanical strength of Ni-based superalloys can be quantified by referring to the formulations developed by Fleischer for highly diluted solutes, while the Labusch model is used when the concentration of elements in solution increases and the elastic fields of the solutes begin to overlap. In general, these models can be reduced to a single expression.

$$\sigma_{ss} \propto \sum_i G\, \epsilon_i^p\, c_i^q \tag{1.2}$$

In this formula, G is the shear modulus of the matrix, ϵ_i is the size mismatch parameter, ci the atomic concentration of solute i and the exponents p and q typically take values characteristic of $p \approx 1, q \approx 1/2$ in Fleischer's model and e $p = 3/2, q = 2/3$ in Labusch's model. [6]

1.1.3. Precipitation Hardening

A key strengthening mechanism in Ni-based superalloys involves the formation of intermetallic secondary phases through precipitation. Unlike solid solution strengthening alloys, precipitation hardening systems require carefully designed heat treatment sequences to achieve their full mechanical potential. In practice, a combination of solution treatment followed by ageing promotes the nucleation of fine, uniformly distributed precipitates within the matrix. When the matrix consists of the Ni-rich γ phase, increasing the aluminium content favours the formation of a secondary phase designated as γ′ (Ni_3Al), which represents the dominant strengthening phase in nickel-based superalloys. This intermetallic compound grows coherently within the γ matrix and adopts an ordered $L1_2$ crystal structure, which shares crystallographic compatibility with the surrounding matrix. Titanium can replace more than half of the aluminium sites within the γ′ lattice, resulting in the compound Ni_3 (Al, Ti), the most commonly γ′ variant in commercial alloys. Additional elements, such as niobium and tantalum, similarly can substitute for aluminium within the γ′ structure. However, excessive substitution beyond a critical threshold can compromise the coherency between γ′ and the matrix, generating significant lattice misfit and elastic strain. These effects promote localised stress concentrations and interfacial sliding, potentially leading to the degradation of both the mechanical stability and the strengthening efficiency of the precipitate phase. [7]

The high-temperature behaviour of Ni-based superalloys is strongly governed by the volume fraction, size and morphology of the γ′ phase. The primary goal of the ageing step is to promote the development of a cuboidal γ′ morphology dispersed within the matrix, with coherent interfaces and narrow γ channels separating adjacent cuboids as shown in Figure 1.3. This specific dual-phase microstructure is the responsible for the remarkable mechanical performance of these alloys during prolonged thermal exposure.[5]

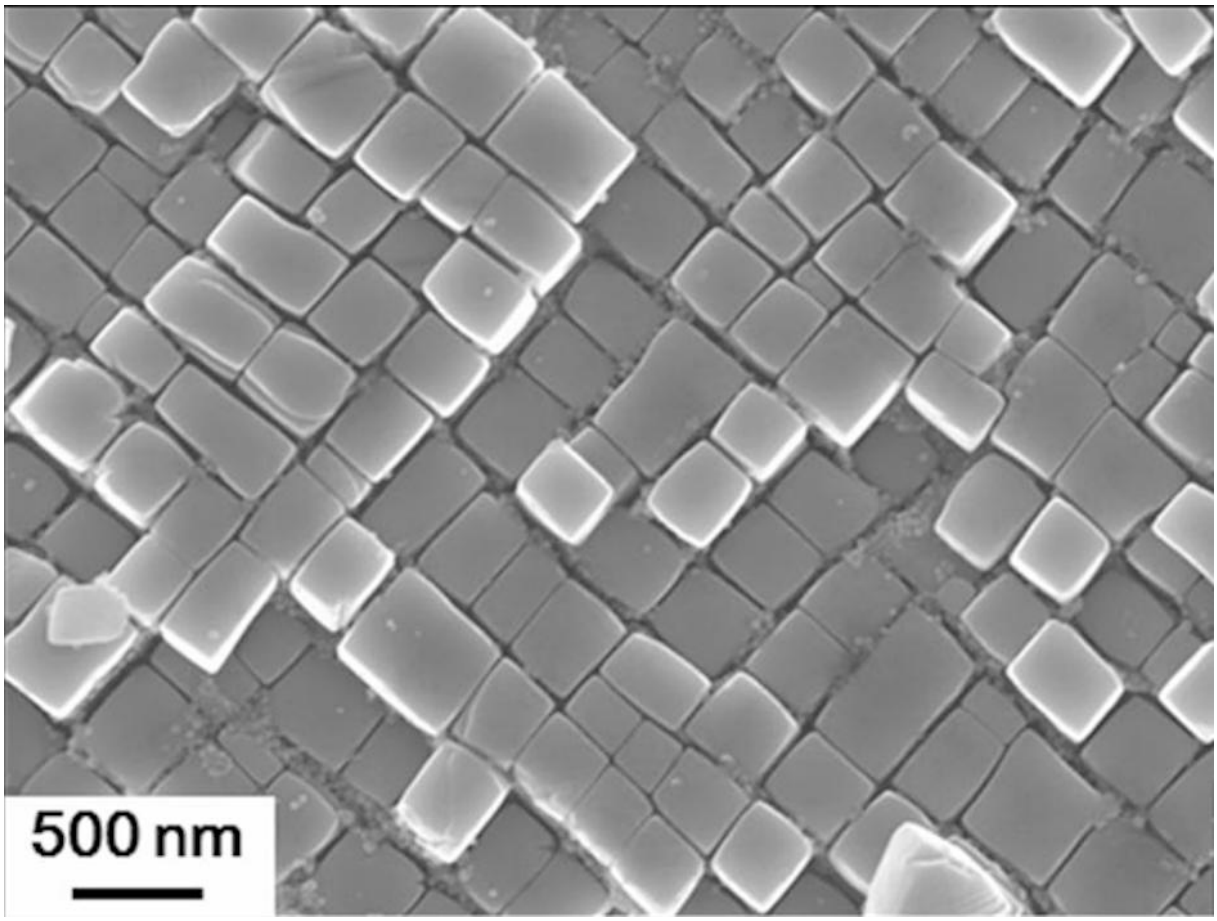

Figure 1.3: Dual-phase microstructure γ/γ' of ni-based superalloy after aging[8]

Precipitate size plays a critical role in governing the hardening response. When γ′ particles are small and fully coherent, dislocations can penetrate them through a shearing mechanism. Under the applied shear stress, dislocations nucleate within the γ matrix and, upon entering the ordered γ′ lattice, generate a high-energy planar defect known as an anti-phase boundary (APB), arising from the local disruption of chemical periodicity. To reduce the associated energy penalty, deformation proceeds through the coordinated motion of dislocation pairs: the leading dislocation is temporarily arrested at the γ/γ′ interface until the trailing dislocation enters the precipitate and restores the ordered arrangement by annihilating the APB. Figure 1.4 (a). Beyond a critical particle size, the operative deformation mechanism transitions from shearing to bypassing, and a reduction in hardness is typically observed. When γ′ precipitates are sufficiently coarse, dislocations can no longer shear through them and instead bow elastically between neighbouring particles through the Orowan looping mechanism. As the dislocation curvature increases under the applied stress, the line tension eventually becomes unsustainable, causing the dislocation to bypass the precipitate and leave behind a closed loop encircling it. This mechanism becomes increasingly effective as the inter-particle spacing decreases. Figure1.4 (b). [9]

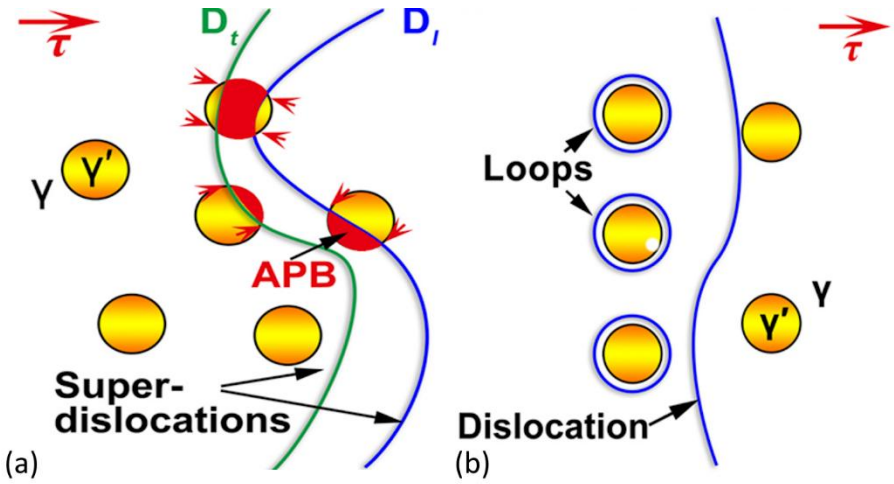

Figure 1.4: Dislocation interaction mechanisms in γ′ strengthened superalloys: (a) anti-phase boundary (APB) shearing mechanism and (b) Orowan looping mechanism.[10]

In general, a higher γ′ volume fraction translates into greater mechanical strength and a reduced creep rate, provided that the precipitate morphology and size are appropriately tailored. A distinctive feature of Ni-based superalloys is the yield strength anomaly: when the γ′ volume fraction exceeds approximately 40%, the flow stress increases rather than decreases with rising temperature, reaching a peak at around 800 °C. [9]The volume fraction of the γ' phase also plays a decisive role in terms of which manufacturing processes is feasible. Alloys with relatively low to moderate γ′ contents can typically be processed through conventional deformation techniques such as forging or rolling. However, as the γ′ fraction approaches 40-45% in wrought alloys, the material becomes increasingly resistant to plastic deformation, exhibiting a markedly brittle response that makes thermomechanical processing progressively more challenging. At high γ′ volume fractions, conventional forming operations cannot be used, and components must instead be produced through alternative routes such as investment casting or powder metallurgy technologies.[11]

In high-temperature Ni-based superalloys, strength mainly comes from the precipitation of cubic Ni_3Al γ′ particles. A different strengthening mechanism is used in Inconel 718, one of the most widely employed superalloys in industry, where the dominant hardening phase consists of tetragonal Ni_3Nb γ″ precipitates. This alloys class is inherently constrained to moderate temperature service, as exposure above approximately 650 °C triggers the decomposition of the metastable γ″ phase into the thermodynamically stable δ phase. This transformation is accompanied by a loss of structural coherency and a significant deterioration in mechanical strength, effectively limiting their use to high temperatures. [12] These precipitates are coherent with the matrix and their structure is shown in Figure 1.5.

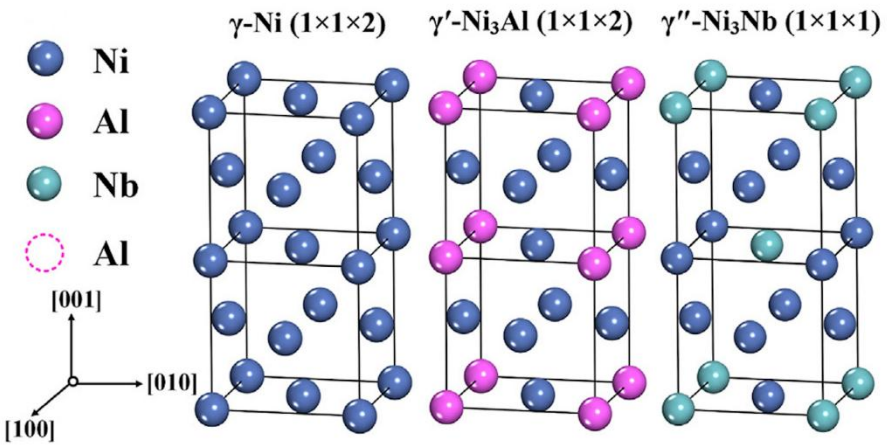

Figure 1.5: Crystal structures of the three principal phases in Ni-based superalloys: γ-Ni (FCC matrix), γ′-Ni_3Al , and γ″-Ni_3Nb. [13]

1.1.4. Coherency and misfit stresses at the γ/γ′ interface

The γ′ precipitates share the same lattice as the austenitic matrix, but a slightly difference in lattice parameter exists between the two phases. At the interface, both lattices undergo elastic distortion to maintain crystallographic continuity. The degree of this structural incompatibility is quantified by a parameter known as the lattice misfit δ, defined as:

$$\delta = \frac{\alpha_{\gamma'} - \alpha_{\gamma}}{\left(\frac{\alpha_{\gamma'} + \alpha_{\gamma}}{2}\right)} \tag{1.3}$$

The parameter $\alpha_{\gamma'}$ and α_{γ} denote the lattice constants of γ′ phase and γ phase, respectively. The lattice mismatch between the interface plays a crucial role in the determination of mechanical properties of these alloys, since the associated elastic distortion contributes significantly to their strengthening response. This is due to the control of γ′ precipitates into periodic arrays of ordered and defined cuboids during the ageing treatment. The lattice misfit can be either positive or negative, depending on the relative values of the lattice constants of the two phases. The variation of misfit magnitude induces considerable changes in the γ/γ′ microstructure. When the lattice misfit approaches zero, the reduction in elastic strain energy favours the formation of nearly spherical precipitates, as this morphology minimises interfacial energy. As the misfit increases, however, the growing elastic strain and lattice distortion energy promote a transition towards a cuboidal morphology, as the system seeks to minimise the total interfacial energy,[14] as illustrated in Figure 1.6.

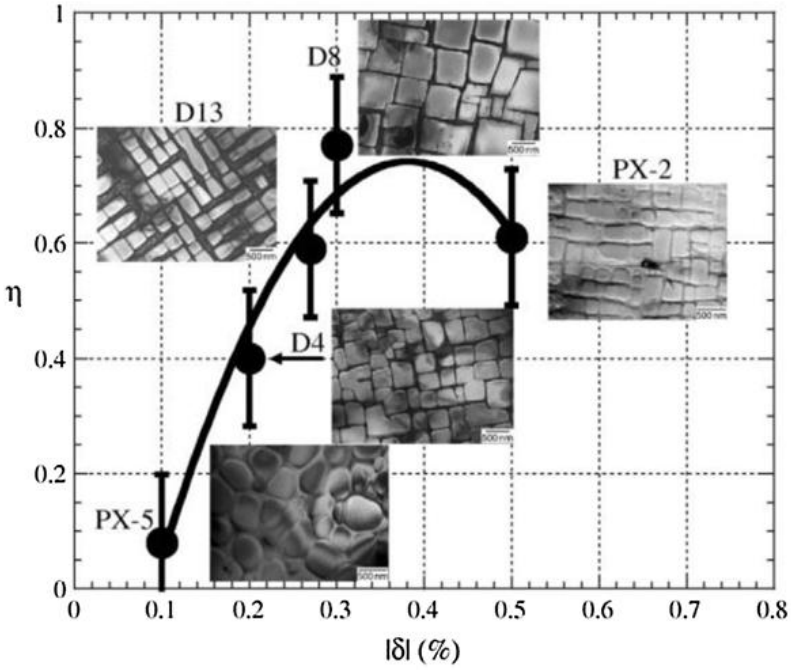

Figure 1.6: Effect of variation of the lattice misfit on the γ′ structure.[14]

Conversely, an excessively large lattice misfit promotes irregular coarsening of γ′ particles. This is due to the progressive loss of interfacial coherency that destabilise the microstructure resulting in a degradation of the alloy creep performance. During creep, dislocations tend to glide along the γ/γ′ interface, bowing into the narrow matrix channels separating adjacent γ′ cuboids. The resistance to dislocation motion is therefore directly governed by the geometry of these channels. When these channels are narrow and constrained, dislocations find it increasingly difficult to propagate through the microstructure, which translates into a meaningful improvement in the creep resistance of the alloy.[14]

1.1.5. Other phases

Carbides and borides are used to improve resistance to high temperatures by stabilising the grain boundary and controlling its growth at operating temperatures. These phases tend to precipitate preferentially at the grain boundary but can also nucleate within the grains of the γ matrix. The most commonly observed carbide classes are MC, $M_{23}C_6$ and M_6C. Primary MC carbides are the precursors of all other carbides, forming directly during liquid phase cooling, and are typically rich in elements such as Hf, Ta, Ti, Nb and Cr, with a CFC structure that makes them thermodynamically stable and tough. $M_{23}C_6$ carbides, typically rich in Cr, precipitate mainly along grain boundaries at lower temperatures around 760°C after prolonged exposure to high temperatures during ageing heat treatments or in service. This phenomenon occurs due to the reaction of MC carbides with the γ matrix:

$$MC + \gamma \rightarrow M_{23}C_6 + \gamma' \quad (1.4)$$

The following reaction promotes the formation of additional γ' phase, which has a positive impact on the mechanical performance of superalloys by increasing the main strengthening phase. The semi-continuous distribution of $M_{23}C_6$ carbides along the edges can play a beneficial role in inhibiting grain boundary sliding and hindering crack propagation. Conversely, if $M_{23}C_6$ is arranged in the form of a continuous thin film decorating the grain boundary, it can lead to the degradation of the properties of superalloys, having a strong embrittling effect. [22]

Boron plays a dual and highly complex role in Ni superalloys. This element is added in very low percentages, typically around 0.03–0.06%. [18] This can segregate at grain boundaries, increasing grain boundary cohesion and reducing the diffusivity of elements. Studies show the capacity to inhibit the formation of continuous Cr-rich $M_{23}C_6$ carbide films along grain boundaries and promote the precipitation of fine Cr-rich M_5B_3 distributed uniformly along grain boundaries. Precipitation of M_3B_2 and M_5B_3 provides an additional pinning effect at grain boundaries, improving resistance to creep and stress rupture. Conversely, excessive boron promotes the formation of brittle phases, degrading high-temperature performance.[23], [24]

Topologically close-packed (TCP) phases are complex intermetallic compounds that may precipitate in nickel-based superalloys under specific compositional and thermal conditions. Their formation is generally undesirable, as they significantly degrade mechanical performance. These phases typically exhibit structures similar to plate-like, needle-like, or lath-shaped morphologies. The most common TCP phases observed in Ni-based superalloys are the σ, μ, and Laves phases, which are rich in of elements as Cr, Mo, W, Nb, and Ta. The compositional control is required during alloy design to limit TCP phase stability. TCP phases are detrimental mainly for two reasons. First, their formation depletes the γ matrix of key solid-solution strengthening elements, thereby reducing creep resistance. Second, they are intrinsically brittle and often act as preferential sites for crack initiation and propagation. In polycrystalline materials, TCP phases commonly precipitate along grain boundaries, where they may form continuous networks that severely degrade the mechanical properties. Among the TCP phases, the σ phase is considered the most harmful due to its pronounced brittleness and plate-like or needle-like morphology. To suppress TCP phase formation, modern alloy design strategies focus on the balance of strengthening and TCP forming elements and optimizing elemental ratios.[21]

1.1.6. Grain boundaries

In general, Hall-Petch's law suggests that a fine grain size increases mechanical properties and fatigue resistance, but grain boundaries (GB) are often considered a weak point in polycrystalline superalloys under creep conditions. This is because when the grain boundary can no longer effectively withstand shear stresses, a phenomenon known as Grain Boundary Sliding (GBS) is triggered. Furthermore, they act as a preferential path for the diffusion of vacancies with possible void formation and crack nucleation, which tend to propagate along the grain boundary, leading to intergranular fracture. [15] Studies have shown that rupture life in creep condition is proportional to grain size. Figure 1.7.

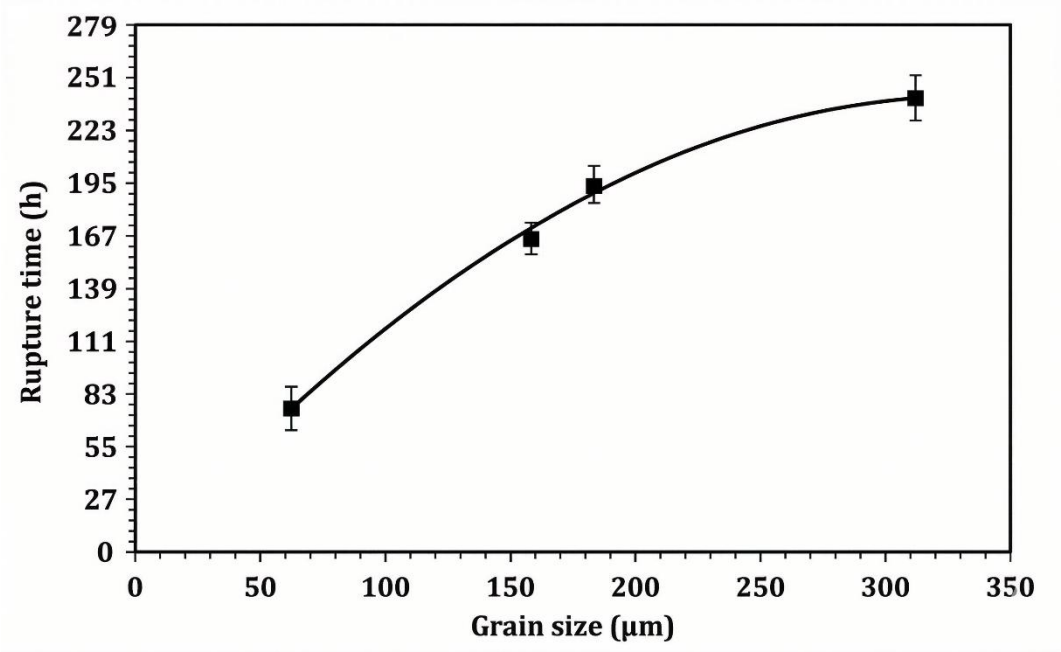

Figure 1.7: Rupture time as a function of grain size, showing a progressive increase in creep life with increasing grain size for Ni-based superalloy.[16]

To reduce the detrimental effects of grain boundaries at high temperatures, the precipitation of carbides and borides is optimized. Thanks to their pinning effect, these stabilize the grain boundaries, slowing down the relative sliding of the grains and stabilizing their structure during prolonged exposure to high temperatures. On the other hand, these microstructural features may act as preferential sites for the nucleation of brittle phases and the initiation of cracking propagation during high-temperature exposure. A design strategy for chemical composition and heat treatment is necessary to achieve a balance between grain size and grain boundary chemistry, including the controlled precipitation of stable MC and $M_{23}C_6$, avoiding the formation of a continuous network of carbides along the GB that result in embrittlement. [5] The morphology of the grain boundaries is also crucial to extend creep life and enhance high-temperature ductility in alloys. Consequently, strengthening grain boundaries through controlled serration, as shown in Figure 1.8, has been widely studied.

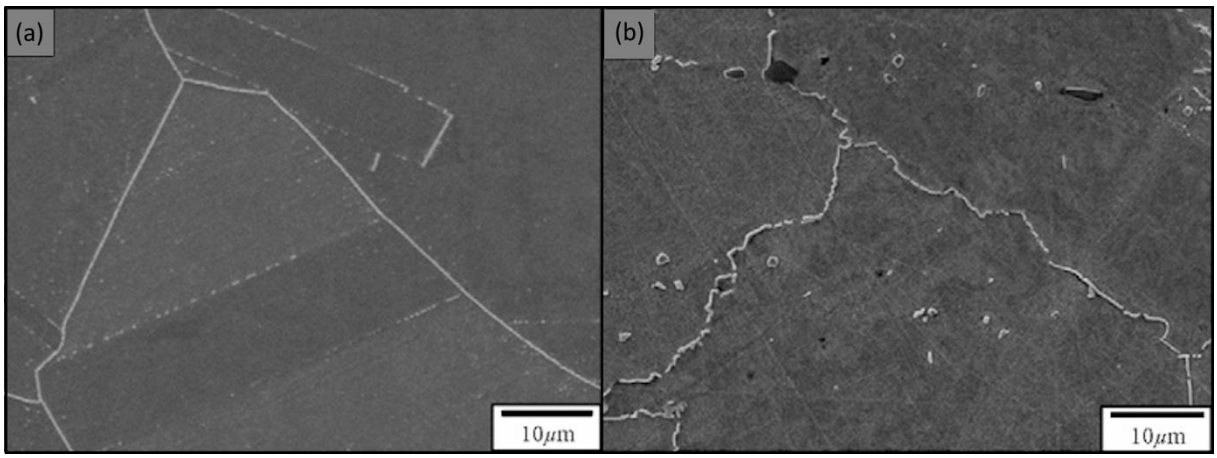

Figure 1.8: SEM micrographs of two characteristic grain boundary morphologies observed in Ni-based superalloys: (a) straight grain boundaries and (b) serrated grain boundaries.[17]

The primary mechanism responsible for the formation of serrated grain boundaries is associated with the controlled precipitation of γ′ particles along grain boundaries. This process is strongly influenced by several thermodynamic, kinetic, and microstructural parameters, including solution treatment temperature, cooling rate and alloy chemical composition. Higher concentrations of γ′-forming elements such as Al and Ti increase the driving force for intergranular precipitation, driving the secondary γ′ precipitates to grow vertically from the grain boundary into the γ matrix, and gradually coarsening, promoting a more pronounced serration effect[18], as shown in Figure 1.9.

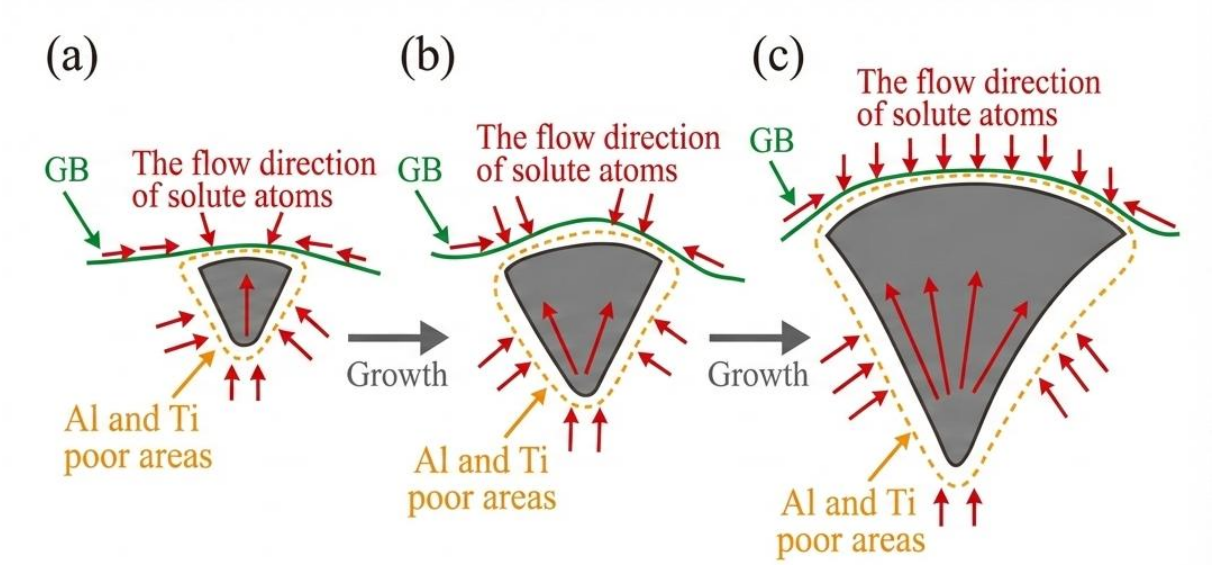

Figure 1.9: Schematic illustration of the grain boundary serration mechanism driven by solute atom redistribution: (a) initial growth stage zones; (b) intermediate growth stage; (c) advanced stage.[19]

Tian et al.[19] conducted a detailed study on the mechanisms governing the development of serrated grain boundaries in a high-performance Ni-based superalloy (GH4742). Their work reveals that not only the chemical composition and thermal history, but also the size, distribution, and shape of γ′ precipitates influence the development of grain boundary serrations. Specifically, coarse γ′ precipitates exhibiting a fan-like morphology were found to promote the formation of high-amplitude grain boundary serrations. This behaviour is mainly attributed to the strong interaction between the growing γ′ phase and the migrating grain boundary, which locally modifies the boundary mobility leading to a more marked undulation as shown in Figure 1.10. In contrast, faster cooling rates lead to the formation of finer and more uniformly distributed γ′ precipitates, resulting in significantly lower serration amplitudes. The study demonstrates that the formation of serrated grain boundaries is strongly influenced by the spatial arrangement of γ′ precipitates along grain boundaries.

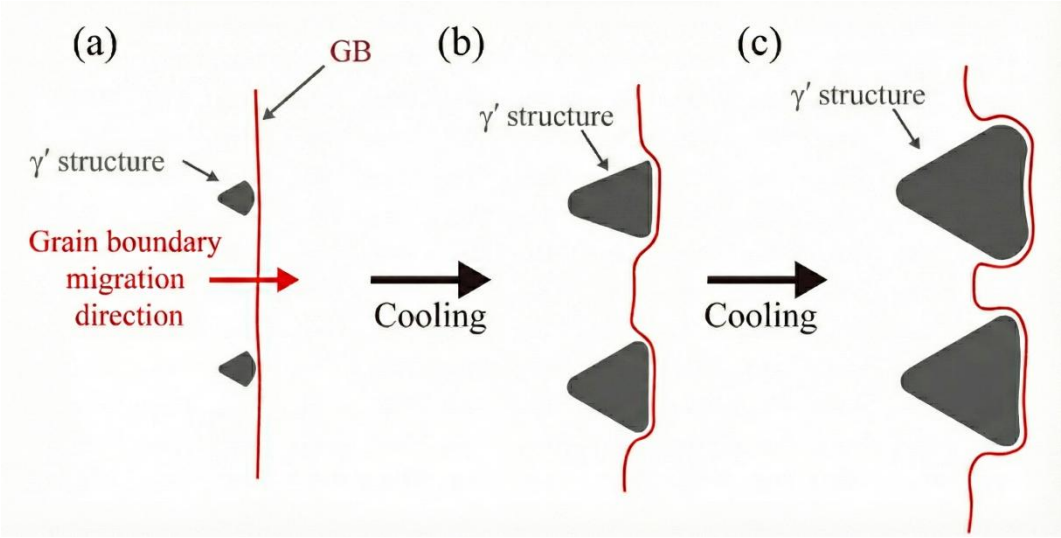

Figure 1.10: schematic grain boundary migration motion in the different stage:(a), (b), (c).[19]

As a preliminary estimation, the characteristics of grain boundaries can be quantified in terms of amplitude and wavelength, as shown in Figure 1.11.

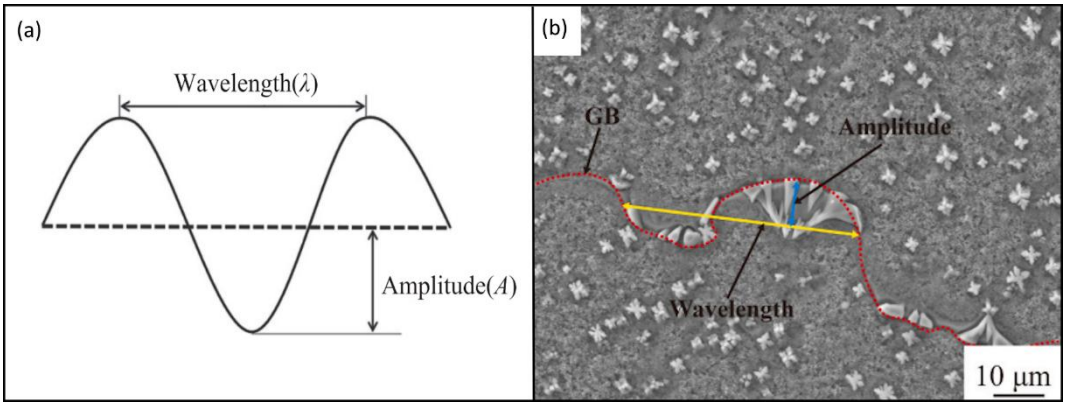

Figure 1.11: Characterisation of serrated grain boundary morphology: (a) schematic illustration of the geometrical parameters wavelength (λ) and amplitude (A); (b) SEM micrograph showing these parameters on a serrated grain boundary (GB).[20]

Starting from this point, more recently also Yu Zhang [20] has reported consistent conclusions, introducing a quantitative methodology for the characterization of grain boundary morphology following different thermal histories. Their approach highlights a strong correlation between the precipitation of secondary phases along grain boundaries and the resulting degree of boundary serration. Specifically, a reduction in cooling rate was shown to promote a progressive increase in both the wavelength and amplitude of the serrated grain boundaries, indicating a continuous intensification of the serration phenomenon. This quantitative framework therefore provides a powerful tool for establishing meaningful correlations between grain boundary morphology and high-temperature mechanical performance. However, accurately modelling the actual trajectory of a grain boundary as a periodic and regular waveform remains challenging, owing to the significant variability in both wavelength and amplitude, as well as the highly irregular and tortuous nature of the mean boundary path.

In this context, the present thesis proposes a novel evaluation methodology based on parameters derived from surface roughness analysis, aimed at quantitatively assessing the degree of grain boundary serration.

1.2. Additive Manufacturing Technology (LB-PBF)

The LB-PBF (laser beam powder bed fusion) additive manufacturing technique is one of the most established in the AM sector. It is used for the production of parts with complex geometries, allowing for the functional design of the component to be manufactured without tools and minimising waste. The key drivers for using this technology include the ability to reduce the weight of the component, improve cooling efficiency (particularly in the internal channels of moulds and turbines) or enhance heat dissipation by utilising lattice structures to increase the specific surface area. For this reason, they are attractive to sectors such as aerospace, energy and biomedical applications, as they enable customisation of and prostheses and promote the osseointegration of prostheses. This technology consists of depositing a layer of powder onto a build platform while, using a lens system, a high-power-density laser source selectively melts the powder according to a designed pattern. Such geometric information is contained in a digital model of the component. The cycle is repeated layer by layer until the part is fully fabricated[25], as shown in Figure 1.12.

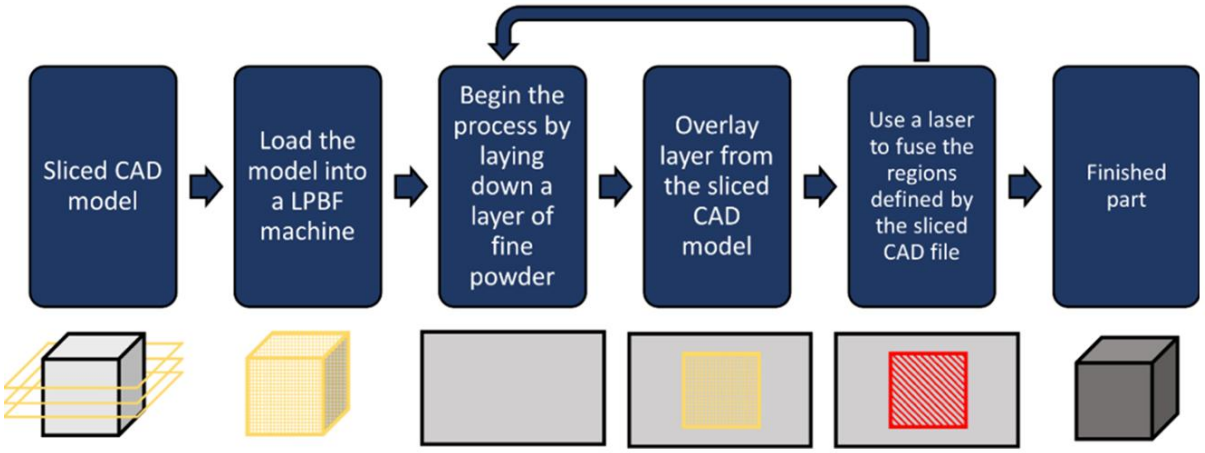

Figure 1.12: Standard build sequence for an L-PBF machine.[25]

Process parameters such as laser power, scan speed, hatch distance and layer thickness must be optimised in order to achieve the best possible final properties of the component. The control of these variables influences the thermal gradient, the stress distribution and the presence of porosity in the final part. In the case of Ni-based superalloys, the thermal history of the material during printing is extremely different from that of traditional metal forming processes. Cooling rates typically range between 10^6 and 10^8 K/s, resulting in highly directional cooling. Consequently, the as-built microstructure is characterised by columnar grains and melt pools along the build direction and more laser tracks in the transverse plane, as shown in Figure 1.13. This extremely high cooling rate suppresses γ' precipitation in the as-built condition; so that only at the nanometre scale can clusters of this phase be observed.[26]

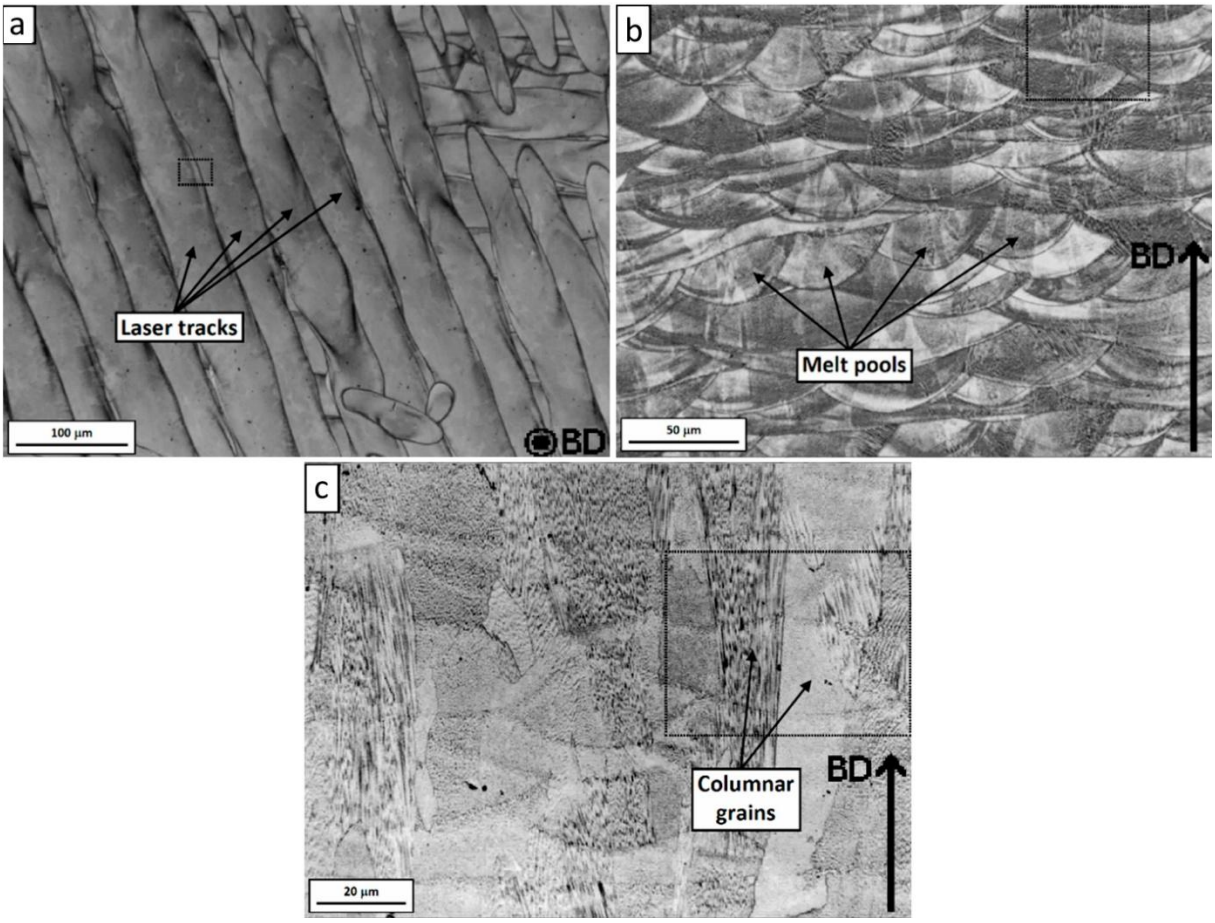

Figure 1.13: Optical micrographs of L-PBF sub-structure: (a) laser tracks in the XZ plane (BD parallel to build direction, (b) melt pool boundaries in the XY plane, (c) columnar grains growing epitaxially along the build direction (BD) in the XZ plane.[26]

Process parameters not only influence the thermal history of nickel-based superalloys, but they are also responsible for the formation of characteristic defects within the final component. Porosity is one of the most common defects and can occur in various forms, as illustrated in Figure 1.14(a). Spherical pores may result from gas trapped within the powder particles during atomisation or from air that may be caught inside during the printing process. Another type of defect consists of unfused voids, characterised by an irregular morphology resulting from insufficient laser energy to achieve complete fusion and bonding between the layers. When the energy density is too high, instability in the molten pool can generate vapour cavities known as ‘keyholes’, which collapse and become trapped during solidification. Among the defects observed in components manufactured using LB-PBF, cracks represent the most critical threat to the structural integrity of the part during service. [27] See Figure 1.14 (b).

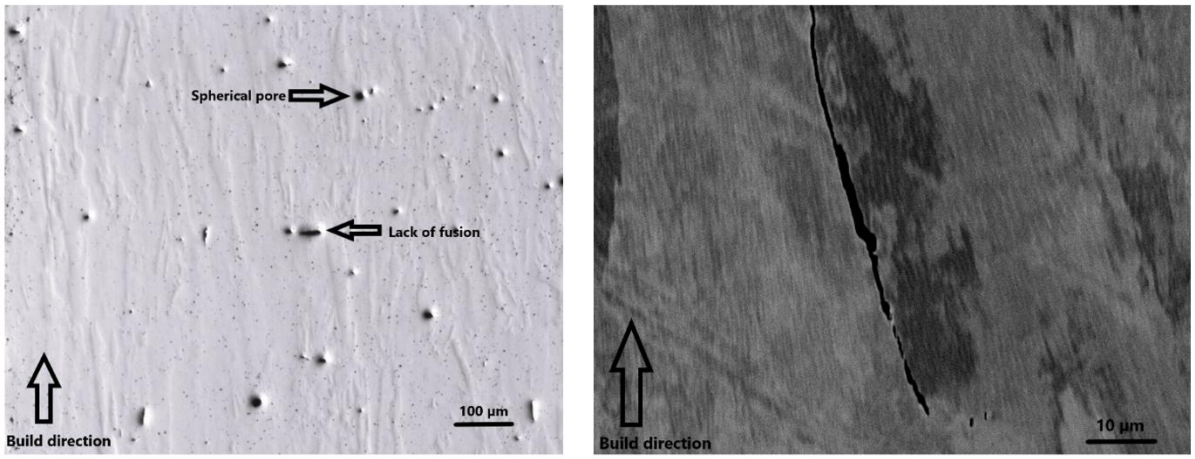

Figure 1.14: Defects observed in L-PBF-manufactured Ni-based superalloy: (a) light microscopy image showing spherical gas pores and lack-of-fusion voids distributed along the build direction; (b) SEM micrograph revealing an intergranular crack propagating parallel to the build direction.[27]

Various cracking mechanisms can occur. For example, solidification cracking occurs within the molten pool during solidification, where the presence of liquid films along the grain boundaries, combined with residual tensile stresses, leads to hot cracking. On the other hand, Liquation cracking aries outside the melt, in the heat-affected zone, where local heating causes melting at the grain boundaries, promoting crack initiation under the effect of applied thermal stresses. Another mechanism is strain ageing cracking, which occurs during post-fabrication heat treatment, when stress relaxation and precipitation hardening take place simultaneously. The presence of residual tensile stresses during and after the printing process can exceed the material's yield strength, amplifying the susceptibility of these superalloys to cracking. This is particularly true for alloys with a high γ′ content (>40%), which are considered difficult to weld. In order to eliminate all these defects caused by incorrect optimisation of the pressing parameters, post-processing treatment, such as hot isostatic pressing (HIP), is required.[27], [28]

1.3. HIP

The HIP (hot isostatic pressing) process is a thermomechanical technique used to produce components that are virtually defect-free or applied to previously manufactured components with the aim of eliminating any residual porosity. The HIP process combines high temperatures with the application of isostatic pressure using an inert gas such as argon, in a setup as simplified in Figure 1.15., simultaneously inducing plastic deformation and a significant increase in diffusion. This condition promotes the closure of internal defects. Numerous studies on nickel-based alloys have shown that this treatment can drastically reduce the presence of porosity, particularly in components produced by additive manufacturing, leading to a significant decrease in pore size. This effect results in an improvement in mechanical properties, including fatigue and creep resistance. [29]

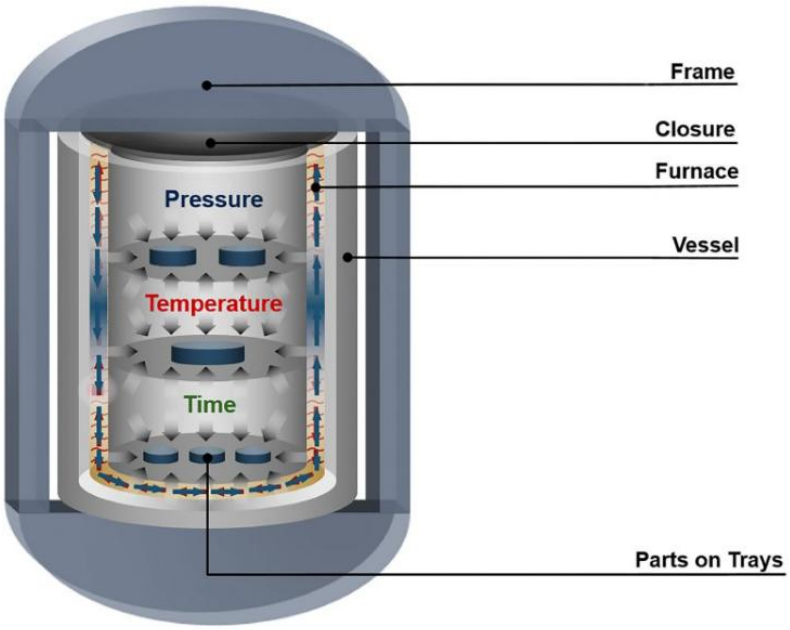

Figure 1.15: A simplified schematic picture of the Hot Isostatic Pressing equipment and process.[30]

During the high-pressure and high-temperature treatment, the material reaches conditions under which it plastically collapses around the larger defects, crushing them. In the final stages of closure, this process is driven by the reduction in the surface energy of internal discontinuities, which acts as the driving force for solid-state diffusion, resulting in a densification level of 99.98%. In the presence of open pores that emerge at the surface, the external pressure balances the isostatic pressure transmitted into the pore, via the gas, thus preventing the pore from closing. In some cases, where the interconnection between the pores and the surface is high, notch-type surface damage may occur. Although these defects can be eliminated with subsequent surface treatments, proper optimisation of the L-PBF+HIP parameters is necessary to minimise them. When gas, such as argon, is introduced during powder atomisation or the printing process, the pore diameter reduces, but if the is closed, the gas remains trapped at high pressure inside, as shown in Figure 1.16. [31]

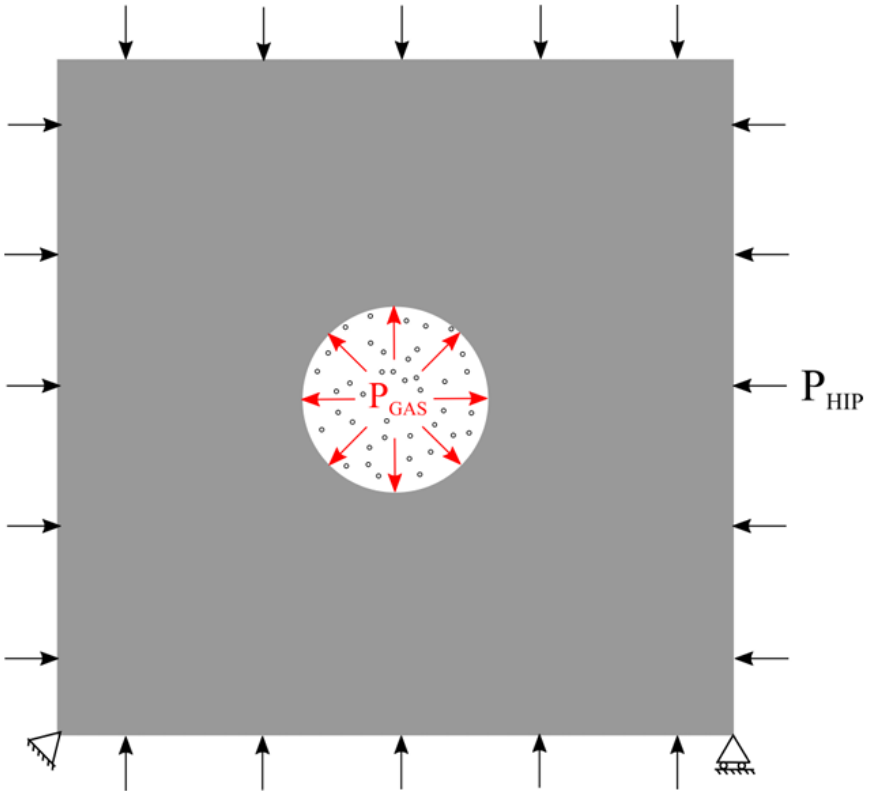

Figure 1.16: Illustration of a gas-filled spherical pore under external applied load P_{HIP}, where the internal gas pressure acting on the pore surface is represented as P_{GAS}.[32]

Following the HIP treatment, Ni-based superalloys require complex heat treatment steps, including solution annealing and one or more aging step. This sequence has the goal to controlling shape, size and volumetric fraction of γ′ phase. These parameters directly influence the final mechanical properties. After the closure of porosity by HIP the first step is the solution annealing, which plays a crucial role in the recovering the anisotropic microstructure inherited from the LB-PBF process, promoting a grain refinement and the transformation of fine, elongated grain toward a more equiaxial structure. The first ageing stage, carried out at temperatures below the γ′ solvus, promotes the growth of precipitates towards a thermodynamically stable cubic morphology. A second ageing stage is then used to maximise the hardening of the alloy through the formation of nanometric tertiary γ′ precipitates.[33] An example of a traditional cycle of heat treatment is shown in Figure 1.17.

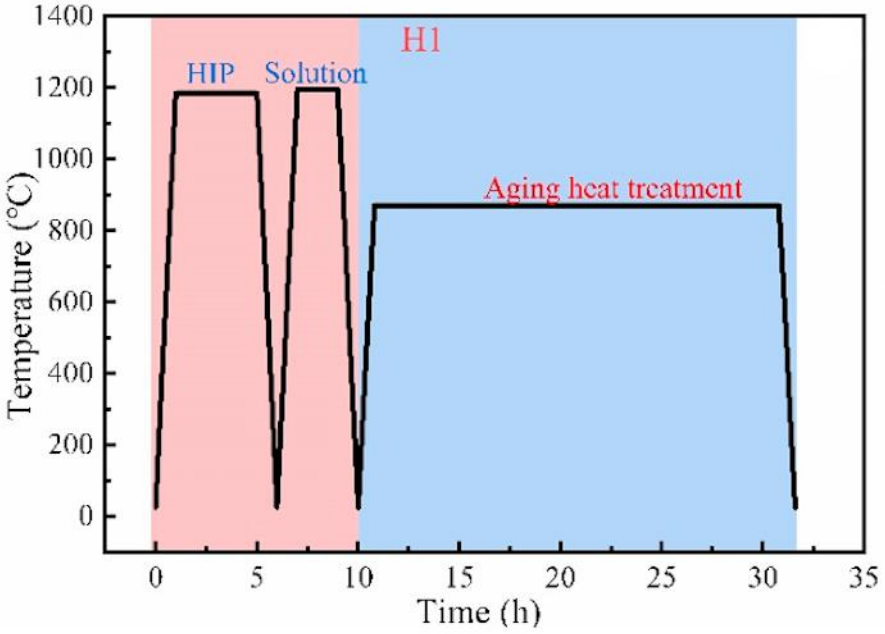

Figure 1.17: Traditional heat treatment cycle of a generic Ni-based alloys. [33]

The consideration of an approach that combines HIP and the heat treatment in a single step is particulary interesting. This strategy, can be followed by the development of HIP systems equipped with high-speed cooling systems (HIP-Quench), significantly reduce overall post-process times. Furthermore, maintaining pressure during the high-temperature holding phases prevents the nucleation or reopening of porosity, which may otherwise occur when heat treatment is performed separately after HIP, for example due to the expansion of trapped gases such as argon. These defects are defined as thermal induced porosity (TIP), particularly detrimental to the mechanical properties of nickel-based superalloys and must be avoided. With regard to γ'-reinforced Ni superalloys, it has been shown that a HIP-Q cycle including solution annealing and ageing can lead to the formation of a finer γ′ population and, in some cases, to a slight increase in the volumetric fraction compared to conventional treatments. An aspect of particular interest for this thesis concerns the possibility of verifying whether a similar approach, applied to superalloys produced by additive manufacturing, allows a higher volumetric fraction of γ′ to be obtained than that achievable with traditional cycles, with potential benefits in terms of mechanical strength and microstructural stability.[33]

2. Materials and Methods

2.1. SAM and heat treatment strategy

As mentioned in previous paragraphs, this thesis analyses the nickel-based superalloy supplied by Siemens Energy. The additive manufacturing employment allows a major freedom in planning; however, it also implies various metallurgical challenges linked to high thermal gradients, non-equilibrium microstructures and workability. The use of this superalloy in the energetic sector for turbine components in hot gas passages needs to endure high temperature conditions, high-cycle fatigue and highly corrosive environments. The SAM alloy project was developed with the aim to overcome these limits and in particular the low weldability of Ni superalloys with a high γ'; phase content and their susceptibility to cracking during the AM process. The SAM cube samples are produced by means of PBF-LB through EOS M290, while the printing parameters used are based on Siemens internal developments. Starting from the previously done study on this superalloy, the aim of this work is to develop an advanced processing route using the HIP-Quench treatment to reduce the steps and time of the entire standard heat treatment cycle. At first, two experimental data sets were considered and the HIP treatment was conducted on them at three different temperatures: 1180°C-1220°C-1240°C. They were also evaluated at two pressure levels, respectively 100Mpa and 150MPa. In these two experimental data sets a cooling rate of 20°C/min was used. Subsequently, the post HIP-treatment microstructural evolutions were assessed in order to choose the optimal parameters for the HIP-Quench procedure. Once the best set was chosen, the HIP-Quench was performed at a cooling rate of 120°C/m and the treatment was concluded with a final aging step.The HIP process paremeters are summarize in Table 2.1. Specifically, the forming process was designed to include two distinct temperature ranges. The first set involved lower temperatures, namely 600 °C and 800 °C, whereas the second set comprised higher temperatures, specifically 975 °C and 1000 °C. The duration of each heat treatment was fixed at four hours.

Table 2.1: Summary of the process parameters of the HIP-treated samples.

Sample	Temperature [°C]	Pressure [MPa]	Cooling rate [°C/min]
Sample A	1180	100	20
Sample B	1220	100	20
Sample C	1240	100	20
Sample D	1180	150	20
Sample E	1220	150	20
Sample F	1240	150	20
Sample G	1180	100	120
Sample H	1220	100	120
Sample I	1240	100	120

2.2. Metallographic preparation of samples

To enable the analysis of porosity and crystalline grain structure in the HIP-treated samples, the specimens were first sectioned using a circular saw in order to expose both a plane parallel to the building direction (XZ) and a transverse plane (XY). The sectioned samples were subsequently mounted in phenolic resin using a hot mounting press. The mounting process was conducted by heating the resin to 160 °C for 30 minutes, ensuring a complete polymerization and providing the sufficient mechanical stability for the subsequent grinding and polishing operations. As a result, circular mounted specimens were obtained. Mechanical surface preparation was then performed using silicon carbide (SiC) abrasive papers on a semi-automatic grinding and polishing machine, starting from a coarse grit (400) and progressively advancing to finer grits up to 1200. Each grinding step was intended to further refine the surface by removing deformation layers and scratches introduced during the previous stages, as well as to restore surface planarity altered during the cutting operation. To achieve a mirror-like surface finish suitable for porosity evaluation by optical microscopy, a final polishing step was conducted using 3 μm and 1 μm diamond suspensions applied on a low-nap synthetic polishing cloth, thereby minimizing surface relief and enhancing microstructural contrast. Once the optical microscope analysis was completed, 0.04 μm colloidal silica step was done to obtain a mirror-like surface. Additionally, the specimens were etched with Kalling's No. 2 solution; this operation enabled the SEM examination and sample grain size calculation. Furthermore, to reveal the fine γ' morphology and its gradual structural changes the specimens were electrolytically etched with 30% H_3PO_4 water solution, applying a voltage of 2.5V for ca. 5 s to look under FESEM and SEM Optical microscope.

2.3. Optical Microscope analysis

The metallographic samples were examined using a Leica MEF4 optical microscope. Observations were performed at magnifications ranging from 50× to 200×. For each cubic sample, a total of five micrographs were acquired from the core region for both the XY and XZ planes. In addition, two micrographs were collected from the extremities of each section to assess the presence of potential open porosity. Following acquisition, the micrographs were processed and analysed using ImageJ, an image analysis software widely employed for quantitative metallographic investigations. The images were converted into binary format, enabling a clear distinction between dense material and defect regions. In the resulting binary images, white areas correspond to defects such as pores, cracks or lack-of-fusion features, whereas black regions represent fully dense material. ImageJ analysis tools were then employed to identify and quantify individual defects by measuring geometrical parameters including area and aspect ratio. The latter was calculated from the major and minor axes of the equivalent ellipse surrounding each defect, providing an effective criterion to discriminate between different defect morphologies. Nearly equiaxed defects with aspect ratios close to unity were attributed to gas-induced porosity, whereas elongated features with higher aspect ratios were associated with cracks or lack-of-fusion defects. Additionally, the area fraction of defects was evaluated as the percentage of the total analysed image area, allowing a quantitative comparison of defect content across different samples and build orientations.

2.4. Scanning Electron Microscopy (SEM)

The samples were characterized by Scanning Electron Microscopy (SEM) using a Zeiss EVO 15 microscope. The SEM investigation was primarily aimed at a detailed examination of the microstructure, with particular focus on the morphology, distribution, and size of the γ' precipitates the presence of carbide phases, inside the grains and at the grain boundaries. Microstructural observations were performed employing both secondary electron (SE) and backscattered electron (BSE) imaging modes, which allowed the simultaneous assessment of surface morphology and compositional contrast. Images were acquired at magnifications ranging from 5,000× to 50,000×, depending on the characteristic dimensions of the features under investigation.

2.5. Grain Boundary Roughness Evaluation Method

The creep resistance of Nickel-based superalloys is strongly influenced by grain boundary morphology. Specifically, the phenomenon of grain boundary serration acts as an obstacle to grain boundary sliding by promoting a mechanical interlocking effect. To quantify the extent of this serration as a function of HIP process parameters (Pressure, Temperature, and cooling rate), a specific image analysis and data post-processing methodology were developed. This procedure is articulated in the following phases:

1. Profile Acquisition and Discretization

Starting from SEM micrographs acquired at high magnification, grain boundary profiles were isolated and digitized using the image analysis software ImageJ. For each sample, representative segments of the intergranular interface were selected, ensuring correct spatial calibration relative to the scale bar (pixel/μm). The profiles were manually traced using segmentation tools to guarantee that the extracted coordinates accurately followed the micro-oscillations induced by the γ' phase or carbides residing at the boundary.

2. Detrending and Waviness Removal

Since grain boundaries inherently exhibit macroscopic curvature unrelated to local serration, the direct application of standard roughness parameters would produce results biased by the grain geometry.

To isolate the specific serration component, a detrending algorithm implemented in Python was applied. The procedure involved:

- Calculation of the mean line (waviness): Performed via a 4th-order least squares polynomial regression, this specific order was identified as the optimal cut-off to filter the macroscopic grain morphology without attenuating the characteristic frequencies of the serration.
- Subtraction of the macroscopic curvature: The polynomial curve was mathematically subtracted from the acquired real profile, resulting in a linearized profile (roughness profile) containing exclusively the information related to the boundary surface roughness.

3. Calculation of Morphological Parameters

Quantitative indicators were calculated on the linearized profile by adapting definitions from the ISO 4287 standard to the specificities of microstructural interfaces:

- Average Roughness (R_a): Calculated as the arithmetic mean of the absolute deviations from the mean line, this parameter provides a to estimate of the average amplitude of the serration.
- Maximum Profile Height (R_z): Evaluated as the maximum deviation between the highest peak and the deepest valley of the roughness profile, this parameter indicates of the maximum extent of interlocking between adjacent grains.
- Tortuosity (τ): corresponding to the Profile Length Ratio (R_{Lr}) codified in the ISO 4287 standard (Geometrical Product Specifications - Surface texture), this parameter is defined as the ratio between the actual path length along the grain boundary $L_{(reale)}$ and the Euclidean distance between the endpoints of the analysed segment $L_{(lineare)}$

$$\tau = R_{Lr} = \frac{L_{real}}{L_{linear}} \tag{2.1}$$

This multiparametric approach allowed for the correlation of HIP treatment variations with the morphological evolution of grain boundaries, providing a quantitative evaluation output shown in Figure 2.1.

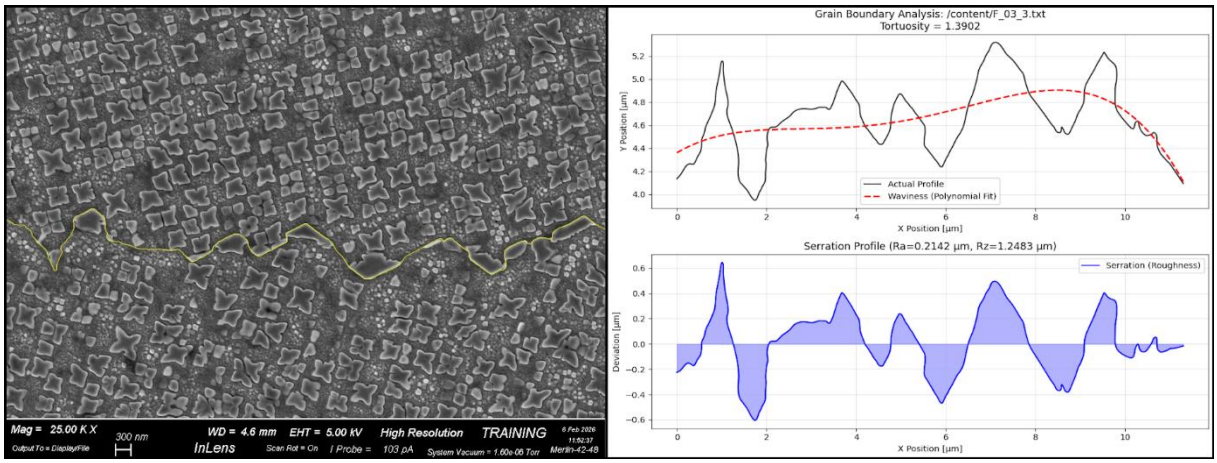

Figure 2.1: Graphical representation of the detrending procedure for grain boundary serration isolation.

2.6. Grain Size Analysis

The average grain size was evaluated through quantitative metallographic analysis performed on five micrographs acquired for each section of samples. Prior to the study, the samples were etched using Kaling's N. 2 solution, to clearly reveal the grain boundaries. Image analysis was performed using the ImageJ software, and grain size measurements were conducted in accordance with the ASTM E112-13 (2021) standard and following the lineal intercept method. In this approach, a set of test lines was superimposed onto each micrograph, and the number of intersections between the lines and the grain boundaries was systematically counted. Standard intersections between test lines and grain boundaries were counted as one intercept. To ensure accuracy, boundary conditions were weighted differently: intersections at line endpoints or tangential to grain boundaries were assigned a value of 1/2, whereas intersections with triple points were weighted as 1/3. This counting protocol was implemented to mitigate edge effects and prevent statistical overestimation. The mean lineal intercept length was determined by dividing the total length of the test lines by the total number of counted intercepts. With the same approach, the average grain size was measured by drawing lines along the building direction and along the longitudinal axis in order to evaluate how the aspect ratio varied with the variation of temperature and pressure.

2.7. Gamma prime (γ′) volume fraction analysis

The microstructural images used for the quantitative analysis were acquired by scanning electron microscopy using a backscattered electron (BSE) detector, in order to exploit the compositional contrast between the different phases present. The obtained micrographs were subsequently processed using ImageJ software following a standardized workflow. First, the images were converted to 8-bit grayscale format; then a threshold-based segmentation was applied and carefully adjusted to identify the γ′ phase relative to the matrix. When present, carbide particles were excluded from the analysis through manual masking, as their higher intensity in BSE images could interfere with the correct identification of the γ′ phase during the thresholding step. After segmentation, the micrographs were converted to binary format and further processed. A hole-filling operation was applied for the elimination of internal discontinuities within the particles, ensuring a compact representation of the γ′ phase. The separation of adjacent or partially overlapping particles was achieved using a watershed algorithm, with additional manual corrections applied when necessary. Finally, quantitative data were extracted using the particle analysis function, which provided information on the size and morphology of the detected features, as well as the total area fraction associated with the γ′ phase. Assuming equivalence between area fraction and volume fraction, the latter was taken as an estimate of the γ′ volume fraction, as reported in Figure 2.2.

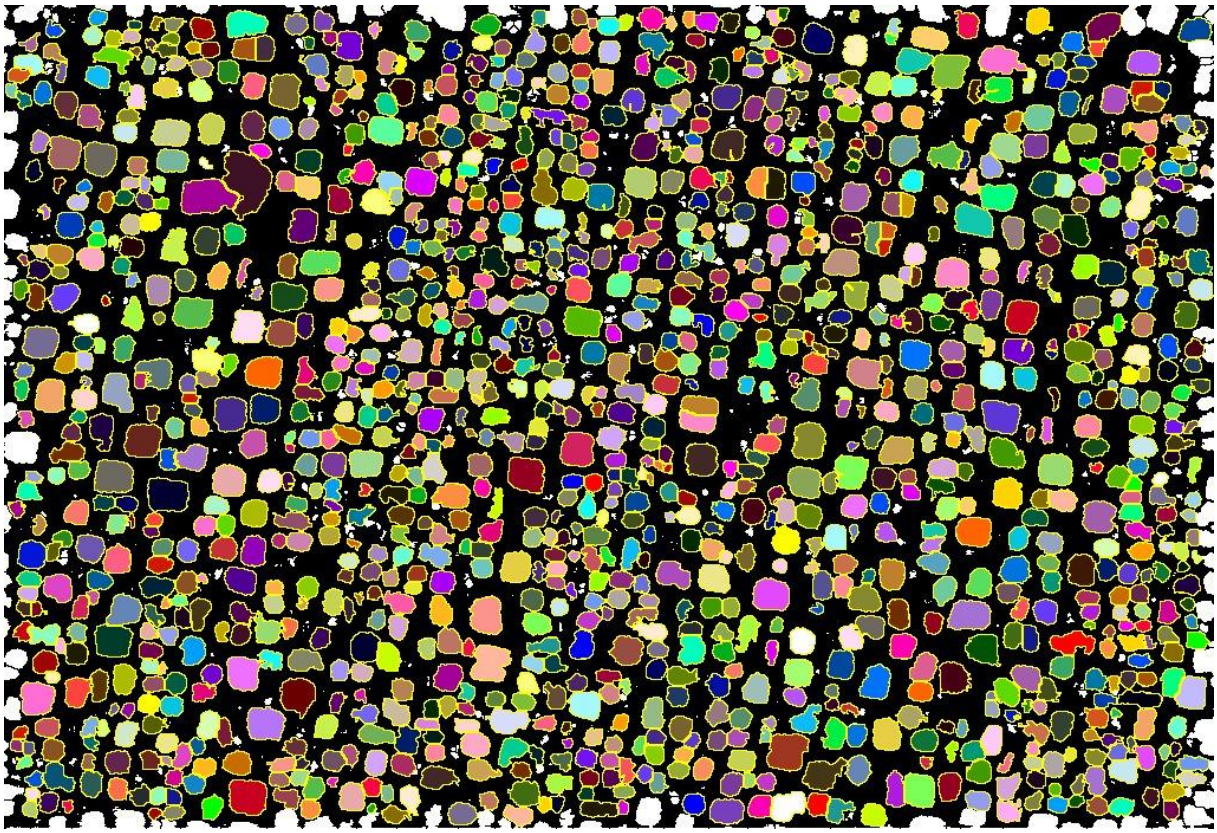

Figure 2.2: ImageJ output showing the segmented γ′ precipitate to evaluate the dimensional population and the volume fraction.

In some cases, the instrument resolution was insufficient to clearly resolve the extremely fine tertiary γ′ precipitates, thus preventing their direct and accurate quantification. For this reason, the evaluation of the γ′ phase volume fraction was conducted using the standard ASTM point-counting method. The procedure consists of superimposing a 9 × 9 grid onto SEM micrographs and counting the points intersecting the γ′ phase as units, while neglecting those falling out from this phase. The ratio between the number of points lying on the γ′ phase and the total number of grid points, multiplied by one hundred, provides an estimate of the γ′ volume fraction. Owing to the instrumental limitations in detecting tertiary γ′ precipitates, the measured volume fraction is expected to be slightly underestimated with respect to the actual value.

2.8. Hardness Test using Brinell scale

The geometry and dimensions of the specimens produced in this study did not allow tensile test; therefore, hardness measurements were performed to obtain indirect information on the mechanical behaviour of the material. Specifically, these tests provided a sufficiently comprehensive framework to assess the influence of the different heat treatments applied in this work. Brinell hardness values were determined for all specimens. These hardness measurements were conducted using an EMCOTEST stationary hardness testing machine (M4U 025). For each specimen, five indentations were performed. Brinell hardness testing was carried out in accordance with the ASTM E10-18 standard. Based on this standard, the hardness value is obtained by forcing a spherical indenter into the material surface under controlled loading conditions. After removal of the applied force, two perpendicular diagonals of the residual indentation are measured. The Brinell hardness number (HBW) is defined as the ratio

between the applied force and the curved surface area of the indentation, assuming a spherical geometry, as expressed by Equation (2.2):

$$HBW = \frac{2F}{\pi D\left(D - \sqrt{D^2 - d^2}\right)} \tag{2.2}$$

- F is the applied load (kgf)
- D is the diameter of the indenter (mm)
- d is the mean diameter of the indentation (mm).

3. Results and discussion of SAM

3.1. DSC of As-Built SAM sample

The critical temperatures associated with the main metallurgical transformations were identified through DSC analysis. Specifically, Figure 3.1 illustrates the graphs of the heating and cooling curves. Both tests show excellent overlap of the peaks coinciding with changes such as the precipitation of γ′, and its dissolution.

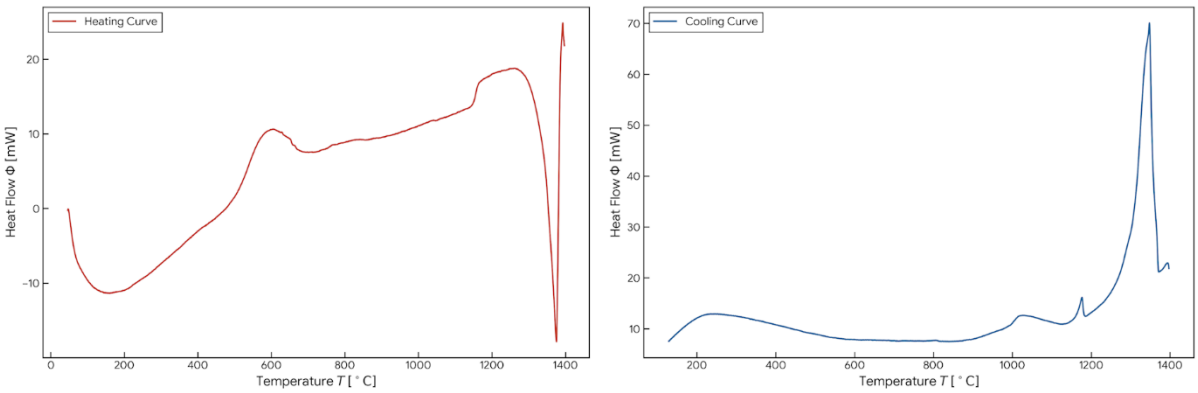

Figure 3.1: Differential Scanning Calorimetry (DSC) thermograms of the as-built sample. The red line on the left indicates the heat flow during the heating cycle, while the blue line on the right represents the cooling cycle.

A pronounced peak is observed at nearly 600 °C, which can be explained by considering the thermal history of the material. As a matter of fact, in the LPBF process, extremely rapid cooling rates are applied to the as-built specimens, leading to microstructural conditions comparable to those of a solution-treated material which has been subjected to severe quenching. Consequently, a highly supersaturated γ matrix is formed. Upon subsequent heating, when the alloy temperature enters the typical aging range, spontaneous precipitation of the γ′ phase takes place, accompanied by an initial stress relaxation within the material.[34] Analysing the DSC signal in the temperature range in which the solubilization takes place, an endothermic peak is to be noticed in the 1100 °C area, indicating the beginning of the γ′ dissolution process.

3.2. Microstructural evaluation of SAM As Built

In order to assess the baseline microstructural features of the SAM alloy in its initial condition, microstructural characterization was first performed on as-built specimens that had not undergone any post-processing heat treatment following fabrication by Laser Powder Bed Fusion (LPBF). After standard metallographic preparation, optical microscopy observations were carried out on cross-sections oriented both parallel to the building direction XZ plane and perpendicular to it XY plane. As illustrated in Figure 3.1, the micrographs reveal the presence of several process-induced defect types of characteristics of additively manufactured components. The average porosity fraction measured is approximately 0.26%, with an average equivalent pore diameter of 8.9 ± 1.7 µm.

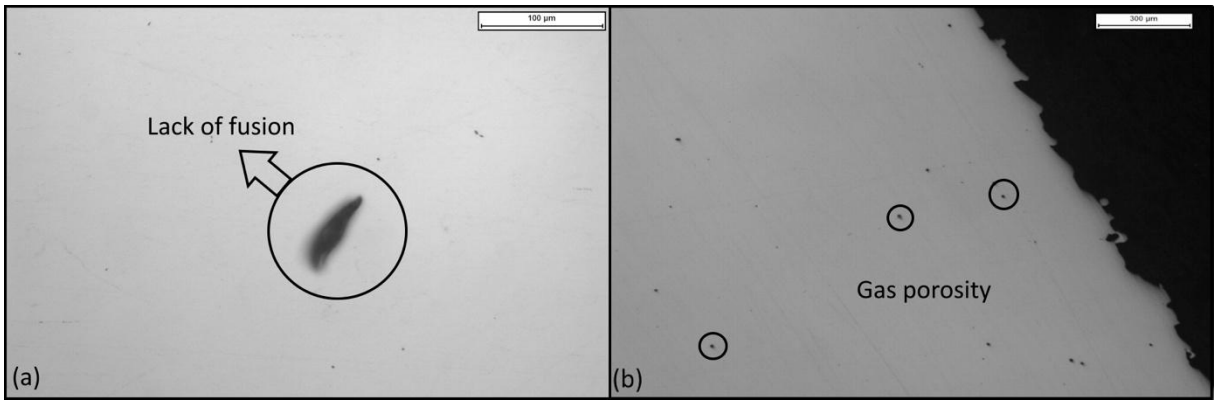

Figure 3.2: LOM images of the as-built SAM specimen: (a) Lack of fusion defect, (b) residual gas porosity

After etching, melt pool boundaries are clearly visible in the XZ section, as illustrated in Fig 3.3(a), which shows variable dimensions due to the layer-by-layer rotation of the scanning strategy. Nevertheless, within each individual layer, relatively uniform size and morphology are displayed by the melt pools. Conversely, observations on the XY plane reveal the laser scanning tracks, being rotated by approximately 67° between successive layers in order to mitigate the risk of interlayer delamination, as illustrated in Fig 3.3(b).

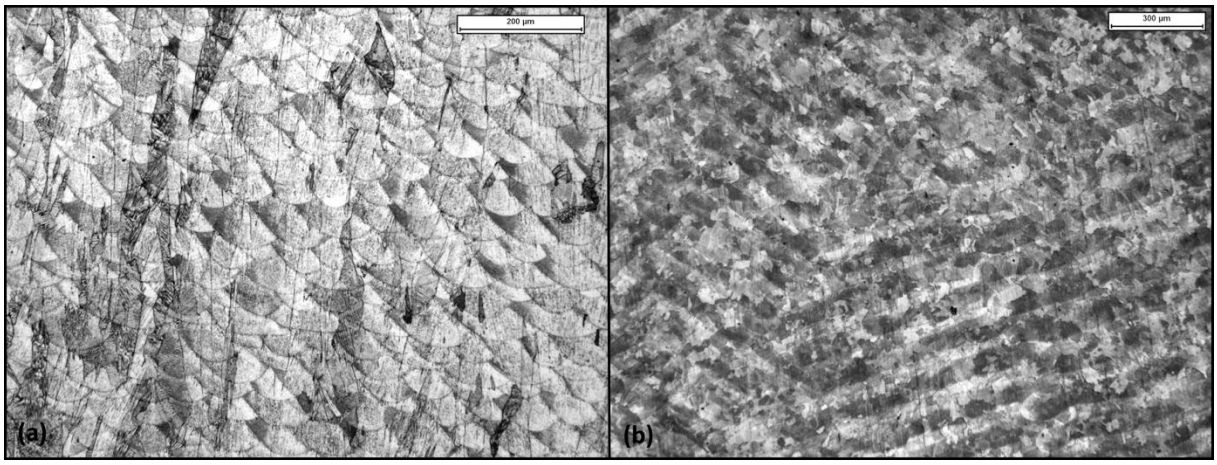

Figure 3.3: LOM images of the as-built sample after Kalling No. 2 etching: (a) melt pool morphology in the XZ cross-section, (b) XY plane microstructure revealing the influence of the scanning strategy.

Differently from conventional casting processes, the outcome of LPBF fabrication is a fine cellular microstructure with grains preferentially aligned along the build direction. Furthermore, the presence of the γ′ phase is not revealed by scanning electron microscopy (SEM) observations, as the extremely high cooling rates, associated with the LPBF process, inhibit its precipitation to sizes large enough to be resolved by SEM. Hardness tests performed on the sample yielded an average hardness value of 310.20 HBW, with a standard deviation of ±6.30 as observed in Table 3.1. In the absence of γ′ precipitation, the hardness can be primarily attributed to the fine grain structure and the resulting high grain density.

Table 3.1: Average and standard deviation values of hardness (HBW) for as built SAM sample.

	Av. Brinell H. [HBW]	St. Dev [HBW]
As Built	310.20	6.30

3.3. Microstructural analysis of standard Hipped samples

The aim of the present work is to assess the feasibility of the hot isostatic pressing process performed above the SAM γ′ solvus temperature. The process is considered effective provided that the two following conditions are fulfilled: the residual porosity removal, resulting in a fully dense or nearly fully dense material, and the grain microstructure improvement with respect to the as-built condition obtained through the AM process. For this purpose, three process parameters were considered: temperature, pressure and cooling rate, which are known to significantly influence the microstructural evolution of the material during the HIP treatment. In the light of previous studies performed on the SAM alloy, it was possible to identify a specific temperature window in which the exceedance of the γ′ solvus temperature is accompanied by the initiation of melting phenomena. Under these conditions, the segregation of alloying elements leads to local variations in the liquid composition. When cooling, these modifications promote the formation of an undesirable metastable phase characterised by a eutectic microstructure. Therefore, the systematic investigation of this temperature window during the hot isostatic pressing treatment aimed to assess the influence of the applied pressure on the formation and stability of this phase. In parallel, the analysis of the improvement in the grain microstructure was not limited to the evaluation of recrystallisation in terms of elimination of cellular and columnar structures and variations in average grain size. A dedicated methodology was also implemented to quantify grain boundary roughness, enabling the characterisation and the optimisation of grain boundary serration as a function of the applied processing parameters. The interest in achieving serrated grain boundaries stems from their potential beneficial effect on the alloy creep resistance, as they enhance the mechanical interlocking between adjacent grains. In addition, the γ′ phase volume fraction and particle size were systematically assessed in correlation with hardness measurement, aiming to identify microstructural conditions most suitable for the subsequent aging heat treatment.

3.3.1. Samples HIP treated -100MPa-20°C/min

The starting point for the investigation of different HIP treatment parameters was established based on the standard condition derived from previous work conducted on SAM, corresponding to a treatment temperature of 1180°C. While the processing pressure was kept constant at 100 MPa throughout all experiments, two additional temperatures were explored, namely 1220°C and 1240°C. The micrographs in Figure 3.4, acquired along both the XZ building direction and the XY plane of the 1180°C-treated sample, reveal the presence of residual porosity localized within the core region of the specimen. Figure 3.4(a) highlights the occurrence of three gas pores exhibiting an equivalent diameter of approximately 9 µm.

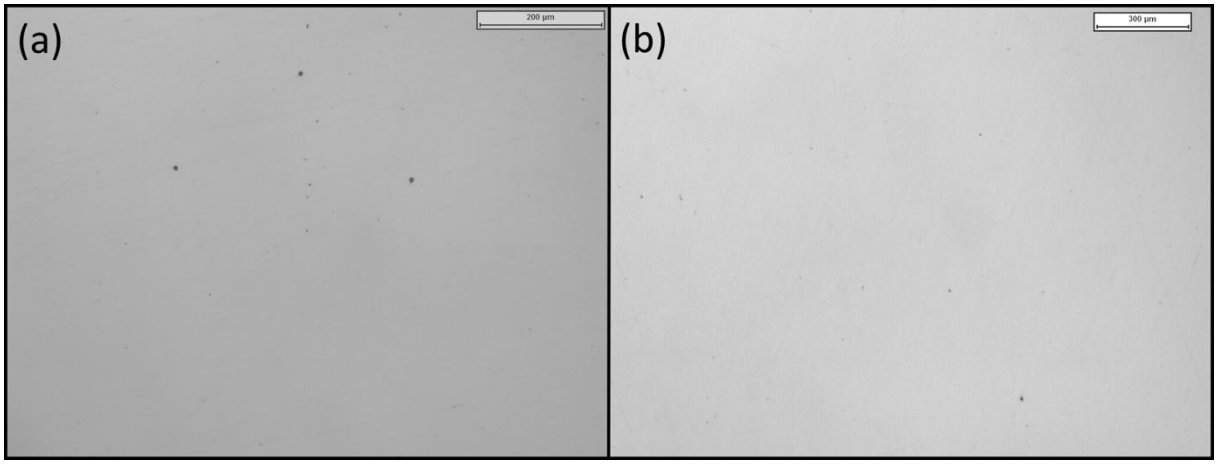

Figure 3.4: LOM images of the 1180°C HIP-treated sample in as polish condition: (a) XZ cross-section, (b) XY cross-section, showing residual gas porosity localized within the core region.

Based on optical microscopy observations, a comprehensive characterization of porosity was carried out. The analysis consist on the evaluation of pore size distribution, average porosity fraction, and aspect ratio, along with their respective standard deviations, on both the XY and XZ cross-sectional planes, for all three specimens belonging to the first experimental set. Given that no statistically significant differences were detected between the core and the near-surface regions, the quantitative analysis was exclusively performed on the core area. Notably, the sporadic occurrence of larger defects was predominantly confined to the subsurface region and can be attributed to the inherent characteristics of the HIP process, as illustrated in Figure 3.5, These defects are classified as open porosity and are expected to be fully eliminated during subsequent machining operations.

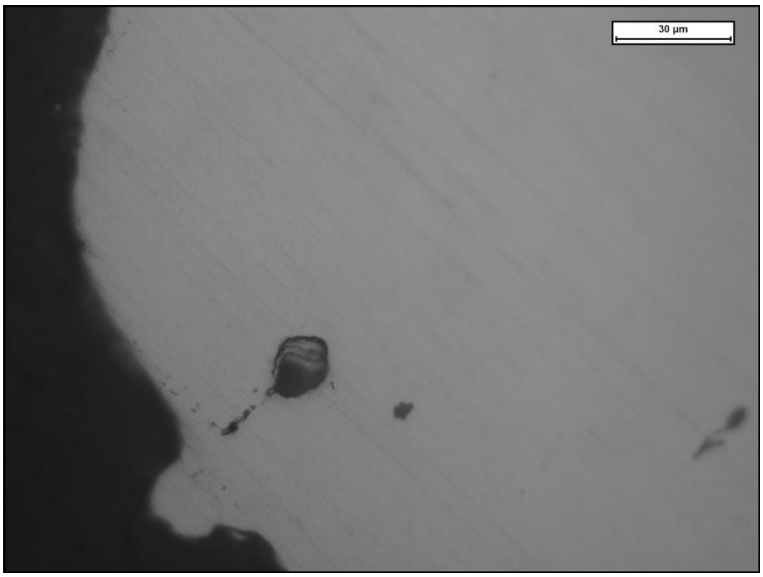

Figure 3.5: Optical micrograph of open porosity near the surface of a HIP-processed sample.

The effect of Hot Isostatic Pressing (HIP) temperature on microstructural porosity is illustrated in Figure 3.6. The graph presents the frequency distribution of equivalent pore diameters (d_{eq}) compared across three processing temperatures. The experimental data are fitted to log-normal distribution curves, which reveal a consistent log-normal trend in the evolution of the pore population. At the lowest temperature of 1180°C, the distribution exhibits a broad, flat profile associated with a relatively high mean diameter. A pronounced tail extending towards larger values (up to 15 µm) indicates the persistence of coarse residual porosity, suggesting that this temperature was insufficient to fully close the largest defects. As the HIP temperature increases to 1220°C and subsequently to 1240°C, two distinct phenomena are observed. First, the distribution curves progressively shift towards lower (d_{eq}) values, confirming the reduction in average pore size driven by enhanced densification kinetics. Second, a marked narrowing of the distributions is observed, with the curves transitioning towards a sharper, more peaked profile. This behaviour is particularly pronounced at 1240°C, where the distribution becomes highly concentrated within the 0.5-4.0 µm range. These findings suggest that higher HIP temperatures effectively reduce both the mean pore size and its statistical dispersion, resulting in the suppression of the largest and most critical defects. Table 3.2 shows the average defect analysis.

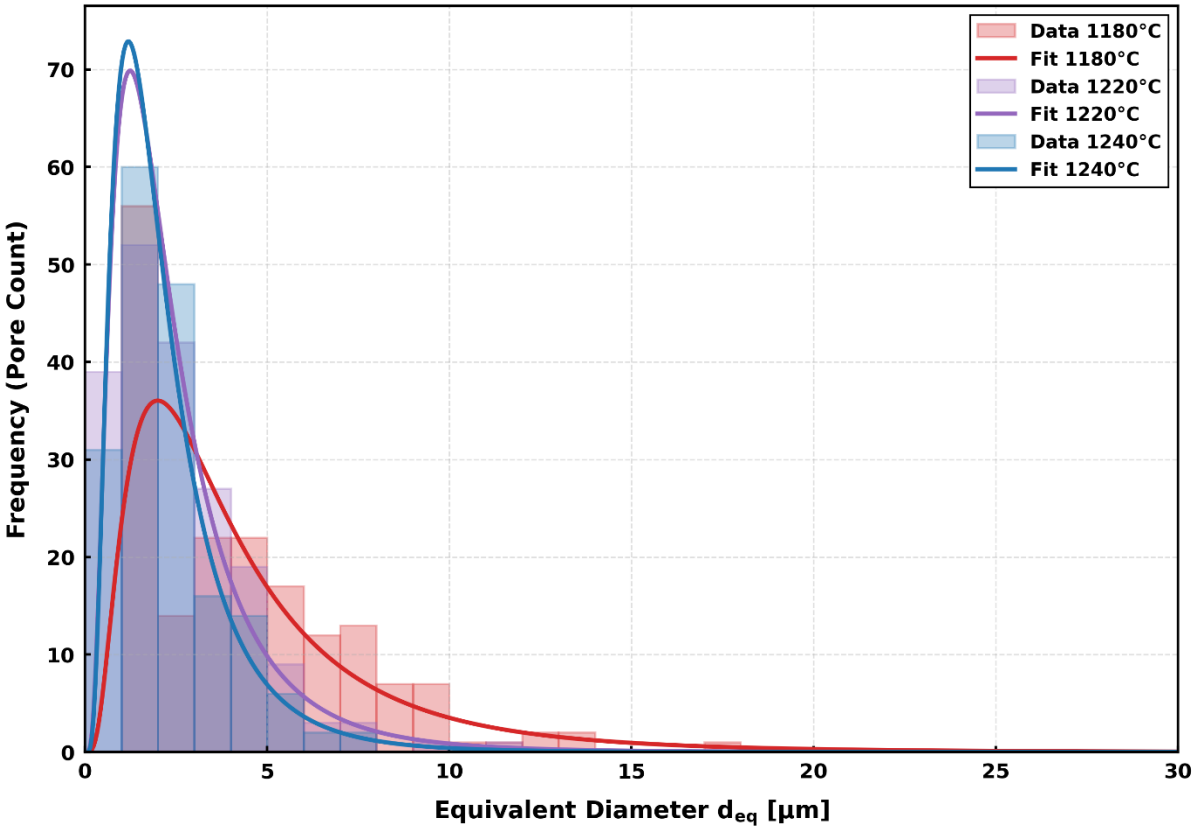

Figure 3.6: Frequency distribution of the equivalent pore diameter (d_{eq}) analysed on the XZ cross-section. The samples were treated by HIP at 100 MPa and three different temperatures: 1180°C, 1220°C, and 1240°C.

Table 3.2: Diameter defect analysis along XZ plane of samples HIP-treated at 100°C-20°C/min.

	Av. defects diameter [µm]	St. Dev [µm]
sample A (1180°C)	4.662	4.34
sample B (1220°C)	2.563	1.77
sample C (1240°C)	2.265	1.419

Along the XY plane, as shown in Figure 3.7, a trend similar to one observed for the previous plane, can be identified across the three temperature conditions. Although the modal peak of the distributions at 1180°C and 1220°C is located at an equivalent diameter (d_{eq}) of approximately 1.5 µm, it is still possible to detect defects, extending up to 14-15 µm. This suggests the presence of macroscopic pores that are not fully closed. With the increase of temperature to 1240 °C, the pore size distribution becomes markedly narrower and shifts towards lower values, with a frequency peak around 1 µm, indicating a more effective densification and closure of larger defects. Table 3.3 shows the average defect analysis.

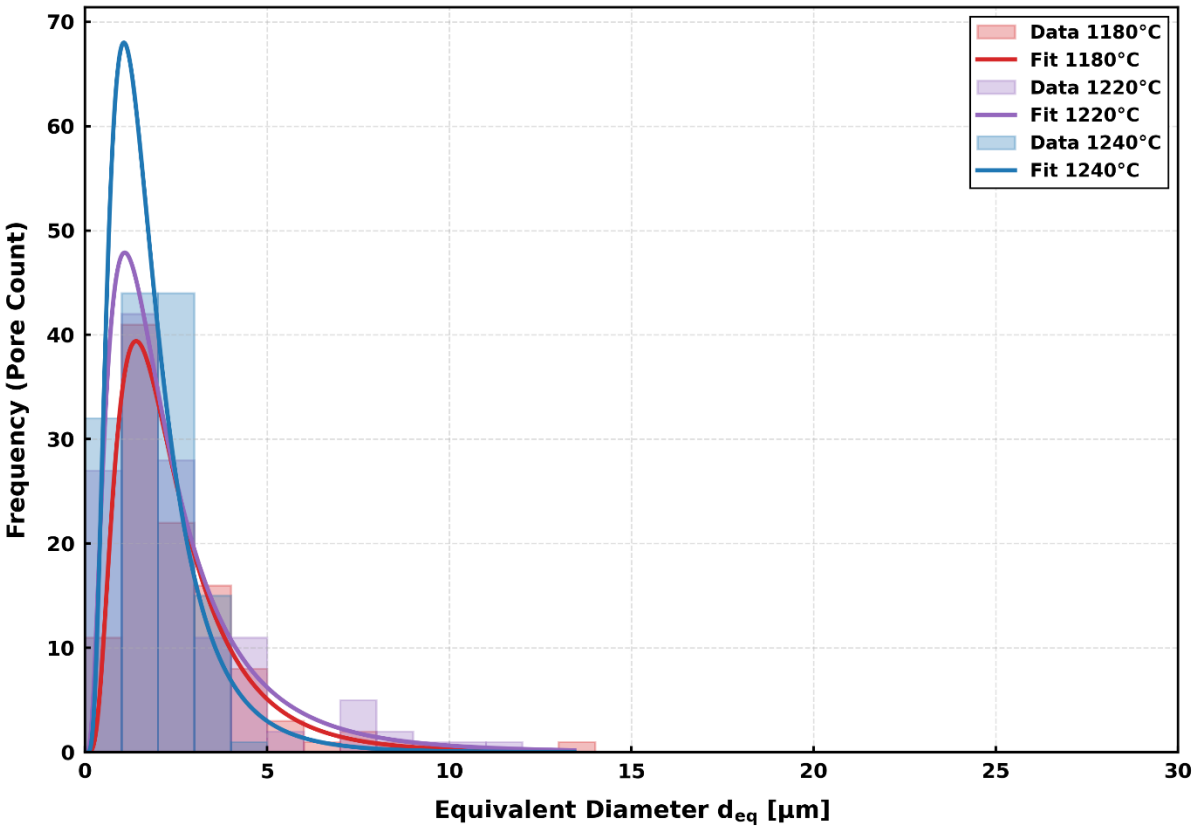

Figure 3.7: Frequency distribution of the equivalent pore diameter (d_{eq}) analysed on the XY cross-section. The samples were treated by HIP at 100 MPa and three different temperatures: 1180°C, 1220°C, and 1240°C.

Table 3.3: Diameter defect analysis along XY plane of samples HIP-treated at 100°C-20°C/min.

	Av. defects diameter [µm]	St. Dev [µm]
sample A (1180°C)	2.57	2.15
sample B (1220°C)	2.55	1.88
sample C (1240°C)	2.45	1.72

With reference to the box plots reported in Figure 3.8 and data Table 3.4, an inverse correlation can be observed between the processing temperature and the volumetric fraction of residual porosity. While the samples treated at 1180 °C and 1220 °C exhibit average porosity values slightly above 0.040-0.045%, a significant reduction is observed at 1240 °C, where the porosity decreases to below 0.030%, with median values close to 0.020%. Another relevant aspect is the reduction in statistical dispersion. Whereas the lower processing temperatures are associated with a wider distribution of porosity values, the box plot corresponding to 1240 °C appears

more compact, indicating a more uniform porosity distribution throughout the sample volume. Furthermore, a comparison between the two observation planes reveals the persistence of a certain degree of anisotropy: the XZ plane systematically shows slightly higher porosity levels and greater dispersion than the XY plane. This behaviour can be attributed to the intrinsic characteristics of the LPBF process, in which lack-of-fusion defects preferentially develop at the interface of melt pool that are mainly oriented along the printing direction.

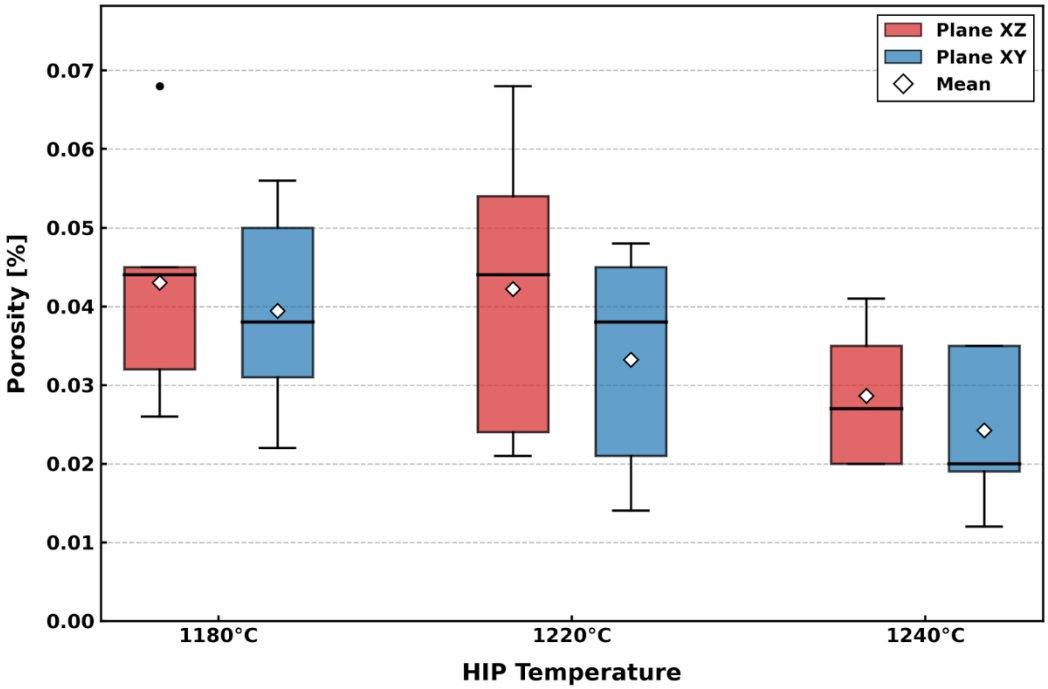

Figure 3.8: Box-plot statistical analysis of residual porosity (%) on XZ and XY planes for samples treated by HIP at 100Mpa and temperatures of 1180°C, 1220°C e 1240°C.

Table 3.4: residual porosity (%) on XZ and XY planes of HIP-treated samples at 100°C-20°C/min.

	XZ Av. porosity [%]	St. Dev [%]	XY Av.porosity [%]	St. Dev [%]
sample A (1180°C)	0.043	0.020	0.039	0.014
sample B (1220°C)	0.042	0.019	0.033	0.015
sample C (1240°C)	0.029	0.009	0.025	0.010

With respect to the shape of the defects, the graph in Fig. 3.9 and Table 3.5, the behaviour illustrated in the graph remains unchanged as the process temperature increases, indicating that the closure of the defects is isotropic along the three dimensions. The standard deviations also stay virtually unchanged, suggesting a homogeneous distribution of defect shapes throughout the material, regardless of the considered plane.

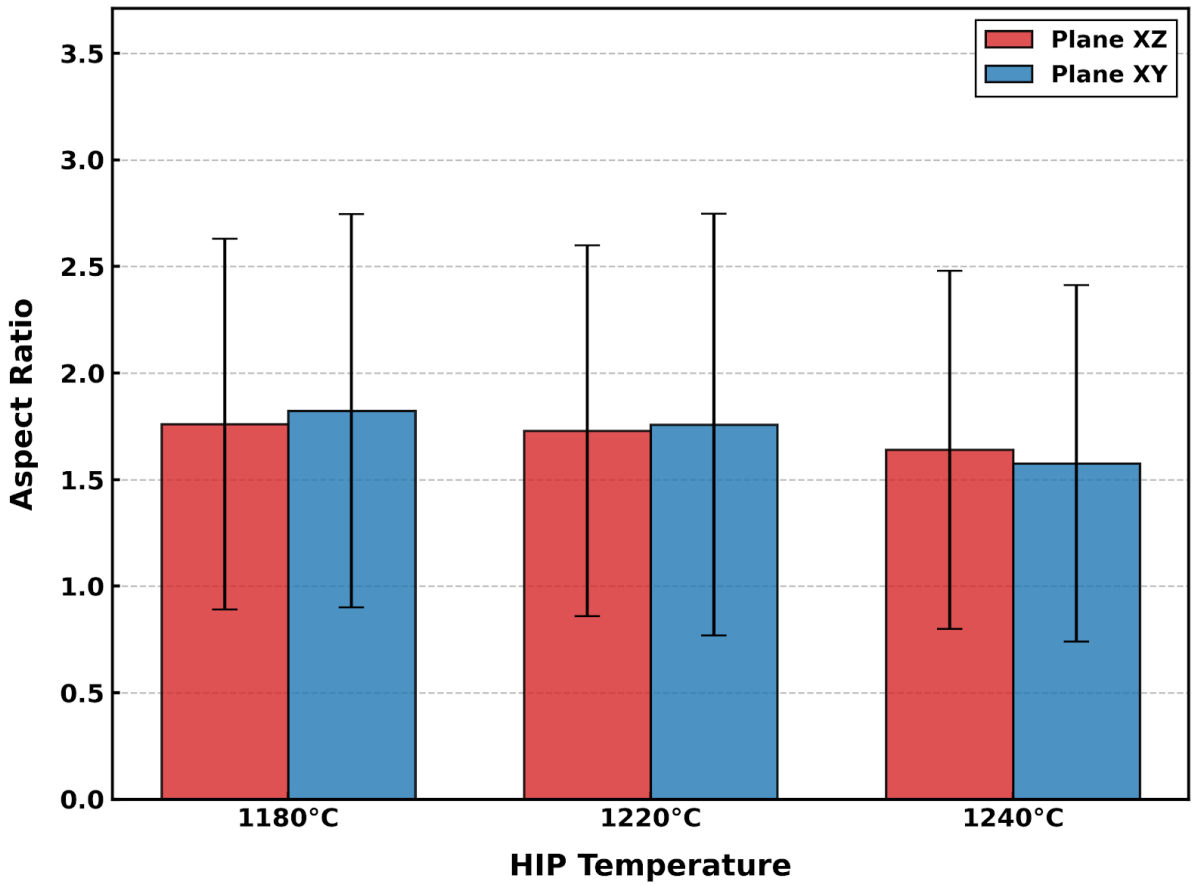

Figure 3.9: Average aspect ratio of pores, measured on XZ and XY planes for samples treated by HIP at 100Mpa and temperatures of 1180°C, 1220°C and 1240°C.

Table 3.5: Aspect ratio defect analysis along XZ and XY planes of HIP-treated samples at 100°C-20°C/min.

	XZ AR	St. Dev	XY AR	St. Dev
sample A (1180°C)	1.76	0.87	1.82	0.92
sample B (1220°C)	1.73	0.87	1.76	0.99
sample C (1240°C)	1.64	0.84	1.57	0.84

The analysis revealed a significant reduction in terms of porosity, reaching densification values of over 99.96%, which demonstrates the effective healing action of the process and the achievement of a considerable defect-free component. Subsequently, the surface was etched with Kalling solution No. 2 and the effects of recrystallisation following HIP treatment at different temperatures were observed under an optical microscope. Specifically, Figure 3.10 shows the evolution of the grain microstructure along the XZ where a partial recrystallisation

destroyed the typical substructure of the PBF-LB process, resulting in larger grains with an anisotropic structure along the cooling gradient during printing.

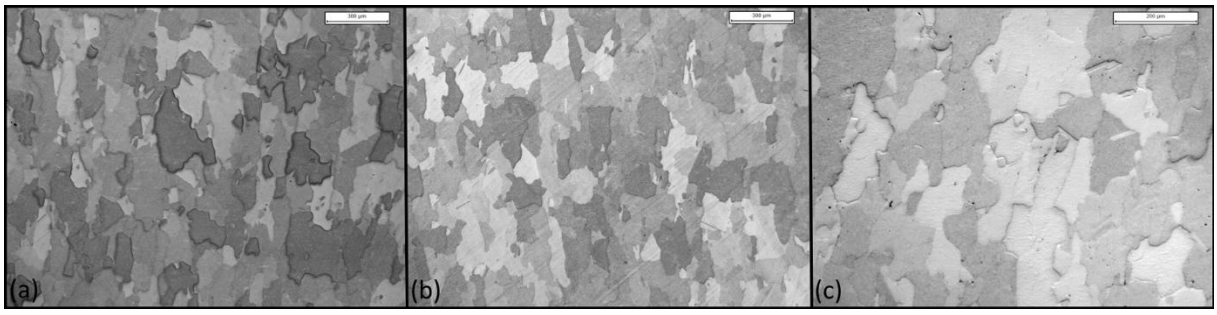

Figure 3.10: Optical microscopy images of etched specimens subjected to HIP treatments at 100MPa along XZ plane at: (a) 1180 °C, (b) 1220 °C and (c) 1240 °C.

The analysis was performed using the ASTM method intercept rule to evaluate the average grain size. This procedure was also applied using the vertical and horizontal intercepts to verify the extent of anisotropy. As shown in Figure 3.11(a) at the first two temperatures, the grain size in the vertical direction ~140 µm is significantly greater than the one in the horizontal direction ~90 µm. This confirms that at 1180°C and 1220°C, the columnar structure inherited from the LPBF process has not been eliminated. The error bars at 1180°C and 1220°C are very wide, suggesting the coexistence of very long columnar grains and smaller, ungrown grains. At 1240°C, the vertical grain size collapses from ~135 to ~90 µm, coming quite close to the horizontal size ~70 µm. The reduction in the average size at 1240°C may be subject not so much to the nucleation of small grains, but rather to the fragmentation and morphological reconfiguration of long columnar grains into more equiaxed grains. This behaviour is confirmed by the aspect ratio trend shown in Figure 3.11(b) At 1180°C - 1220°C the aspect ratio (AR) remains stable at around 1.6, whereas at 1240°C the AR decreases to ~1.25 with the consequent reduction of the error bar, which means that not only is the anisotropy reduced, but also that the grain distribution inside the material is more homogeneous. Since this is a supersolvus treatment, the aim is to solubilize the precipitates. It is likely that at 1180°C and 1220°C, despite being nominally in or near the supersolvus range, carbides or pinning phases may still remain at the grain boundaries (Zener pinning), preventing the migration of the grain interfaces necessary to break the columnar structure.

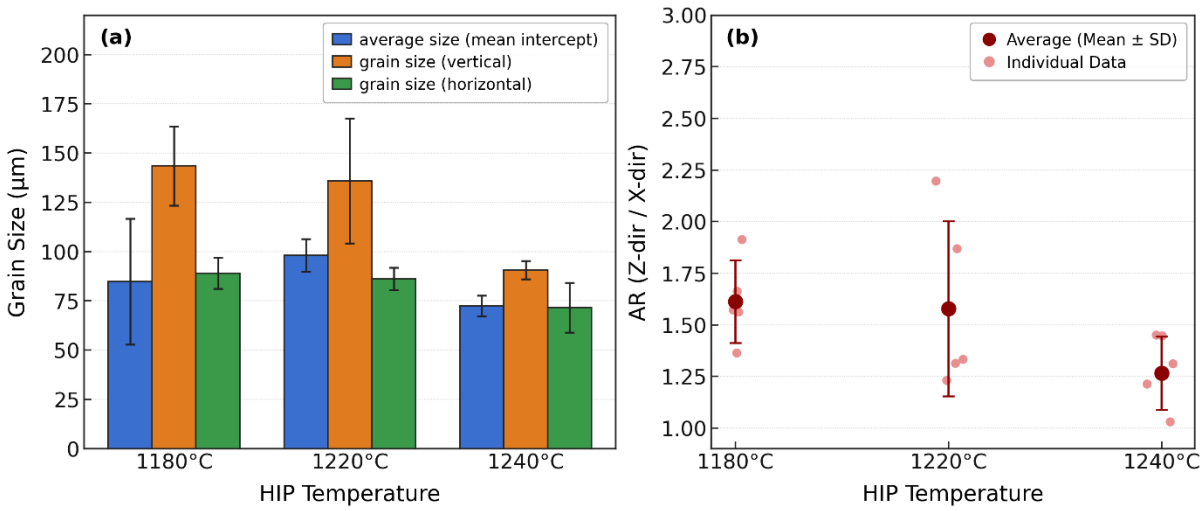

Figure 3.11: (a) Grain size evolution along XZ plane of the HIP-treated samples as a function of HIP temperature at 100MPa (b), Grain AR evolution along XZ of the HIP-treated samples as a function of HIP temperature at 100MPa.

The three-dimensional morphology of the grains was approximated through an equivalent ellipse due to their having inheritance of a partially anisotropic structure from differential cooling during printing along the growth direction. Therefore, on the XY plane, the grains have a more uniform and equiaxed morphology, as it can be seen in Figure 3.12.

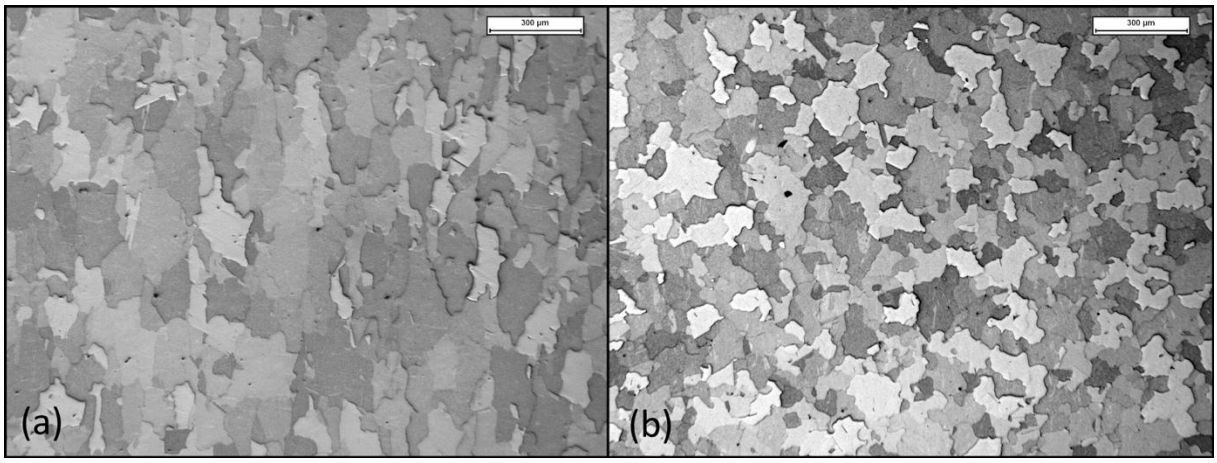

Figure 3.12: Grain microstructure of HIP-treated SAM (a) anisotropic grains along XZ-plane, (b) more equiaxial grains along XY-plane.

For this reason, the average grain size at different process temperatures was evaluated along this plane, but the aspect ratio was not. The obtained results show a clear upward trend similar to the previous in terms of average grain size, with an upward trend increasing the temperatures from 1180°C to 1220°C, but at 1240°C, as can be seen in Figure 3.13, the inversion of trend persist.

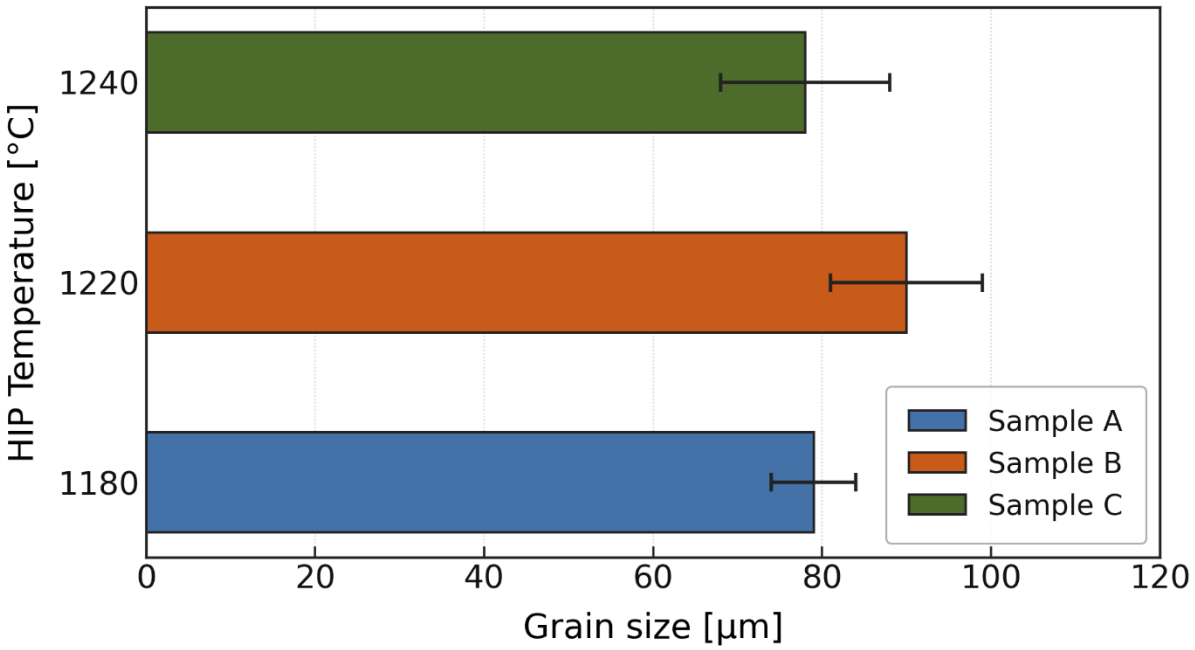

Figure 3.13: Grain size evolution along XY plane of the samples as a function of HIP temperature at 100MPa.

If the effects of HIP on grain are considered macroscopically, a significant change in the microstructure can be observed in terms of size and shape. Moving to higher magnifications, it is possible to appreciate a morphological characteristic of the grain boundary itself. Specifically, Figure 3.14 highlighted the simultaneous presence of both serrated and straight grain boundaries. Together with a coarse grain size, serration is a morphological feature that is significantly beneficial for high-temperature applications, offering he opportunity for what is known as grain boundary engineering.

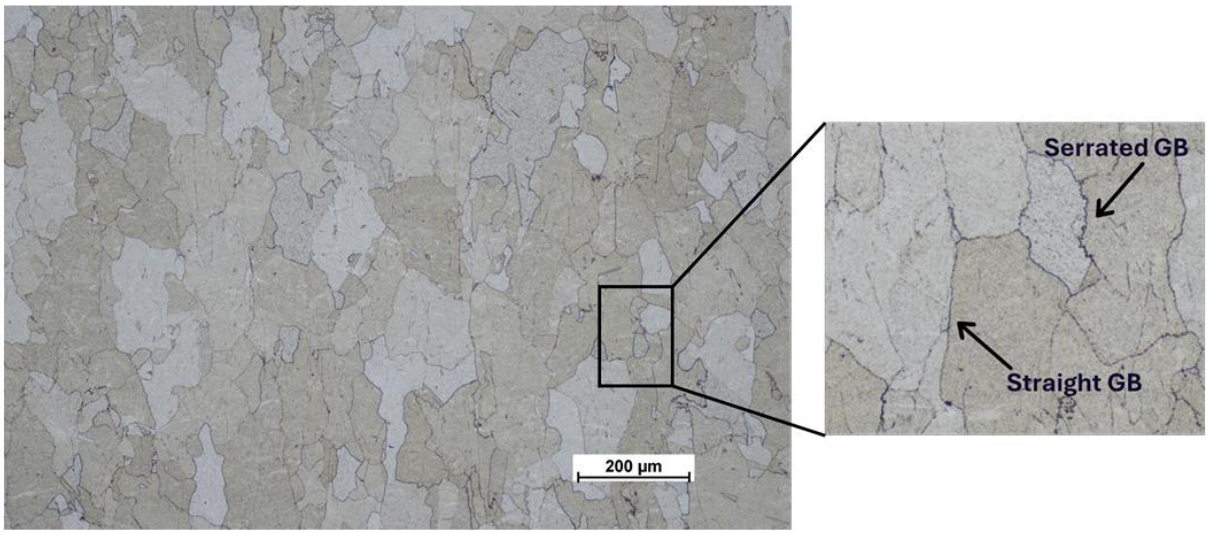

Figure 3.14: Light optical micrographs of the HIP-ed sample after Kalling No. 2, showing a low-magnification overview of the surface and a higher-magnification detail of the grain boundary morphology.[34]

The exact physical mechanism causing the serration effect is not well understood. From a practical perspective, serration is acknowledged to be possibly triggered by super solvus solution heat treatment. During the subsequent cooling stage, the precipitation of secondary phases and fine particles, including γ′, MC carbides, and $M_{23}C_6$ preferentially occurs along the grain boundaries. These precipitates exert a retarding force on the migrating boundaries, effectively inhibiting their motion at high temperatures. This mechanism, known as the Zener drag effect, leads to a reduction in grain boundary mobility and plays a key role in controlling the kinetics of recrystallization and grain growth. [35] Consequently, a detailed characterization of the grain boundaries at higher magnification by means of electron microscopy is required in order to identify the particles responsible for the observed serration and to elucidate the mechanisms governing this phenomenon. Specifically, Figure 3.15, presents a micrograph of a grain boundary exhibiting a noticeable degree of serration.

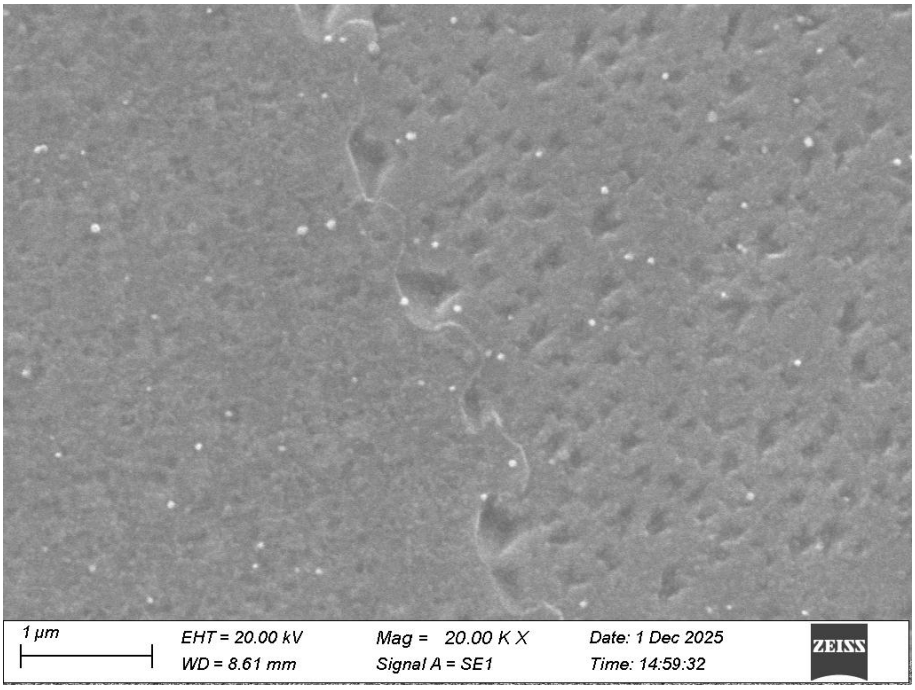

Figure 3.15: Grain boundary serrated of HIP-ed sample at 1180°C at 100MPa-20C°/min.

The presence of relatively coarse γ′ precipitates along the grain boundary is clearly observable; these particles locally alter the trajectory of the boundary, inducing a wavy morphology. As observed in the micrograph, the serrated structure derives from the migration of grain boundary segments between adjacent pinning particles. In particular, the grain located on the left tends to migrate toward the adjacent grain on the right; however, this movement is locally impeded by the presence of γ′ precipitates. This behaviour indicates that, although grain growth can still take place during slow cooling, grain boundary mobility is significantly restricted by the Zener pinning effect exerted in the γ′ phase. As a result, boundary segments in direct contact with the precipitates remain effectively anchored, while the surrounding regions undergo only limited displacement. The presence of carbides is random and not localised near the grain boundary; if present, their effect on the development of grain boundary serration can be considered irrelevant. In other grains, the presence of carbides influencing the grain boundary path has been observed, as shown in Fig. 3.16, but in comparison to the extent of serration caused by γ′, it is significantly lower.

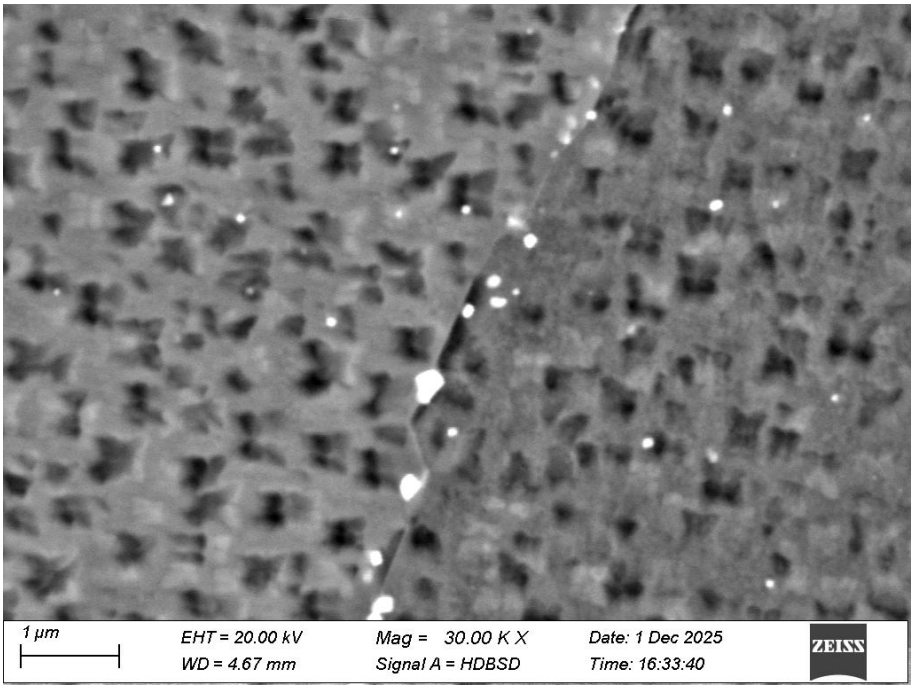

Figure 3.16: SEM micrograph of carbides along grain boundary of HIP-trated sample at 1120°C at 100MPa-20C°/min.

The description of the grain boundary path in geometric terms is very complex. As a first approximation, one might think of comparing the path of the boundary to a wave with a characteristic wavelength and amplitude. However, this interpretation differs greatly from the real complexity of the path, not only because of the wide variability in amplitude and wavelength and the absence of periodicity, but also because the baseline, on which the wave would develop, would not be linear at all. This concept is similar to the one which in surface science, differentiates roughness from waviness. Roughness describes fine-scale, high-frequency local irregularities, whereas waviness refers to larger-scale, low-frequency profile undulations. On the basis of this assumption, the idea was developed to correlate the characteristic parameters of surface science from ISO 4287 standard with the actual path of the grain boundary. A grain boundary roughness evaluation method has been established in order to quantify serration through the analysis of the boundary trace. Namely, this process combines electron microscopy, image analysis to manually trace the profile and extract coordinates (x,y) and a programmed code to calculate the mean line with a fourth-order polynomial curve. This curve is mathematically subtracted from the actual profile acquired in order to return the linearised profile at the graphic level, from which the parameters as average Roughness (R_a), maximum profile height (R_z) and tortuosity (τ) are calculated , as shown in Figures(3.17, 3.18, 3.19).

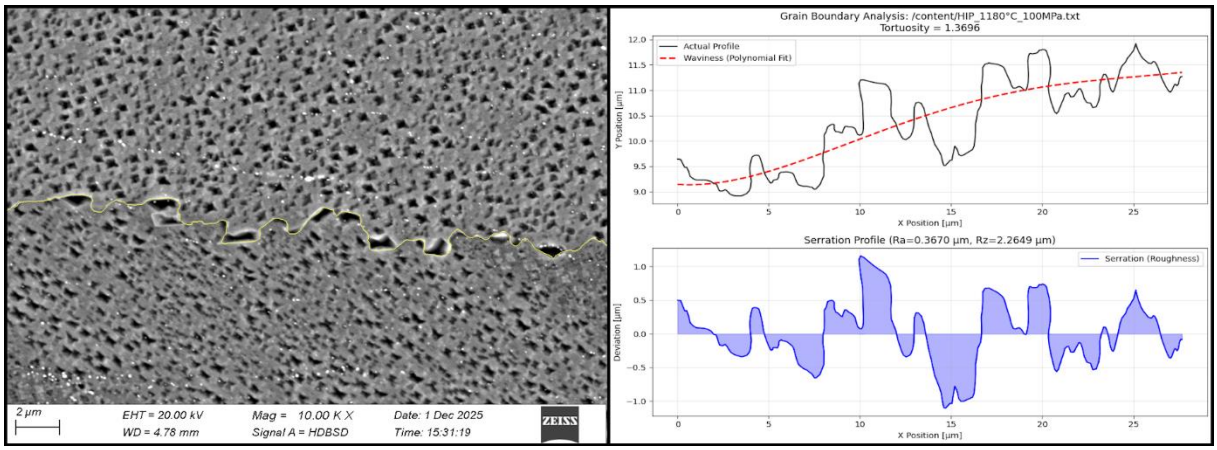

Figure 3.17: Grain boundary roughness evaluation method applied at one grain boundary of HIP-ed sample at 1180°C- 100MPa-20C°/min.

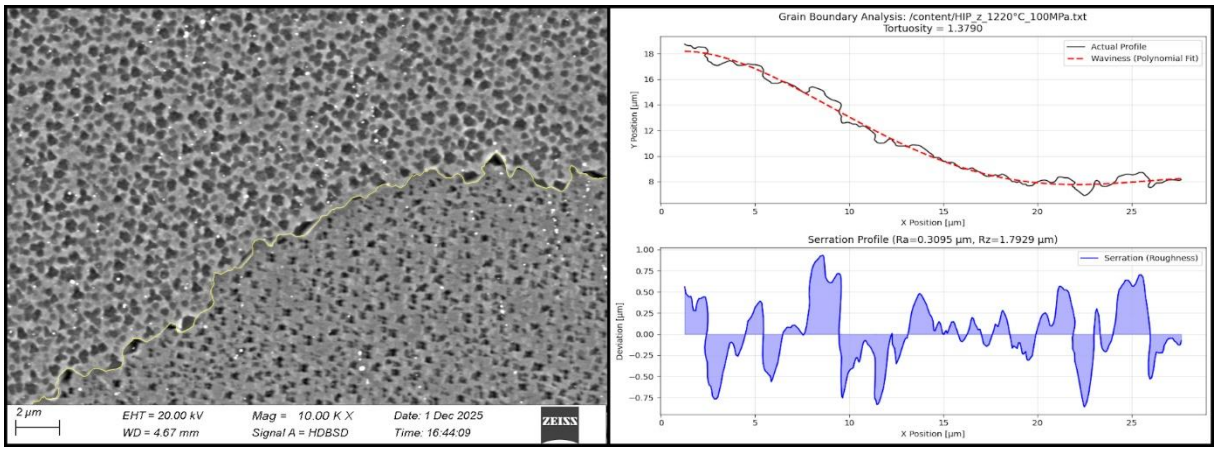

Figure 3.18: Grain boundary roughness evaluation method applied at one grain boundary of HIP-ed sample at 1220°C-100MPa-20C°/min.

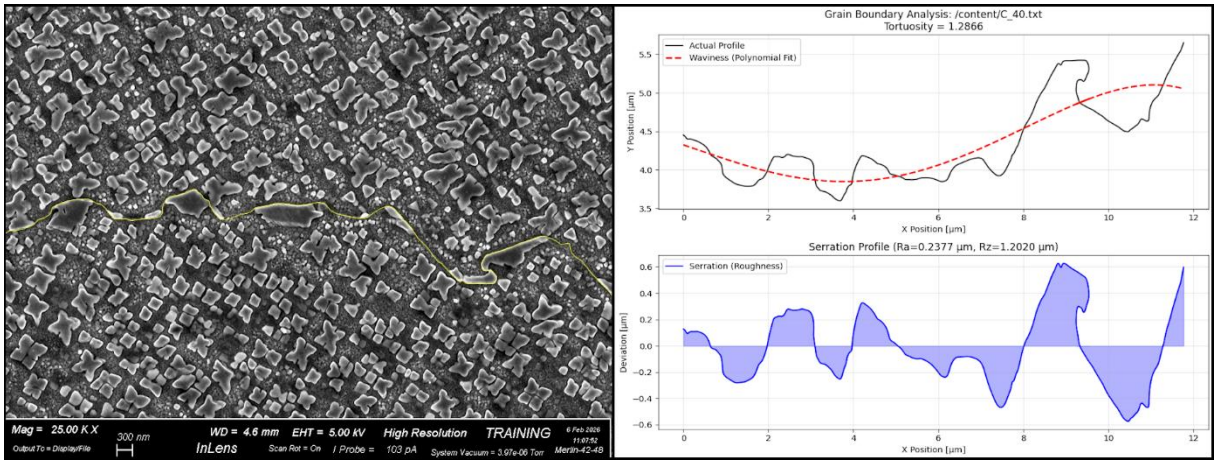

Figure 3.19: Grain boundary roughness evaluation method applied at one grain boundary of HIP-ed sample at 1240°C-100MPa-20C°/min.

This method was applied took into consideration five different grains for each treated sample. The data shown in Table 3.6 highlights that for the first two temperatures, the parameters remain virtually unchanged, while at 1240 °C the serration value collapse. Recalling the physical meaning of these parameters, (R_a)is calculated as the arithmetic mean of the absolute deviations from the mean line. This parameter provides an estimate of the average amplitude of the serration. Maximum Profile Height (R_z) is evaluated as the maximum deviation between the highest peak and the deepest valley of the roughness profile, indicative of the maximum extent of interlocking between adjacent grains, while Tortuosity (τ) is defined as the ratio between the actual path length along the grain boundary and the Euclidean distance between the endpoints of the analysed segment. This parameter gives an idea of the geometric complexity of the path.

Table 3.6: Grain boundary roughness evaluation method parameters of HIP-treated samples at 100°C-20°C/min.

	Av. R_a [µm]	St. Dev [µm]	Av. R_z [µm]	St.Dev [µm]	Av. τ [-]	St. Dev [-]
sample A (1180°C)	0.289	0.102	1.589	0.548	1.482	0.166
sample B (1220°C)	0.282	0.223	1.531	1.190	1.475	0.344
sample C (1240°C)	0.210	0.098	1.131	0.45	1.289	0.177

The qualitative assessment of the observed microstructures shows the generation of very tortuous paths in correspondence of large γ′ domains and irregular morphology. These paths are characterised by very pronounced peaks and valleys between adjacent grains. Conversely, in the presence of smaller or plate-like precipitates, the extent of grain boundary pinning is reduced. The experimental results obtained suggest that higher treatment temperature favour the coalescence of γ′ precipitates and the development of grain boundary with a continuous, film-like morphology, as opposed to large, discrete pinning particles. In regions exhibiting this highly elongated morphology, grain boundary serration virtually disappears. This microstructural evolution directly accounts for the observed reduction in boundary tortuosity and the diminished intensity of the Zener pinning phenomenon, as clearly highlighted by the morphological comparison of the two GBs as shown by the comparison of the two grain boundaries in Figure 3.20.

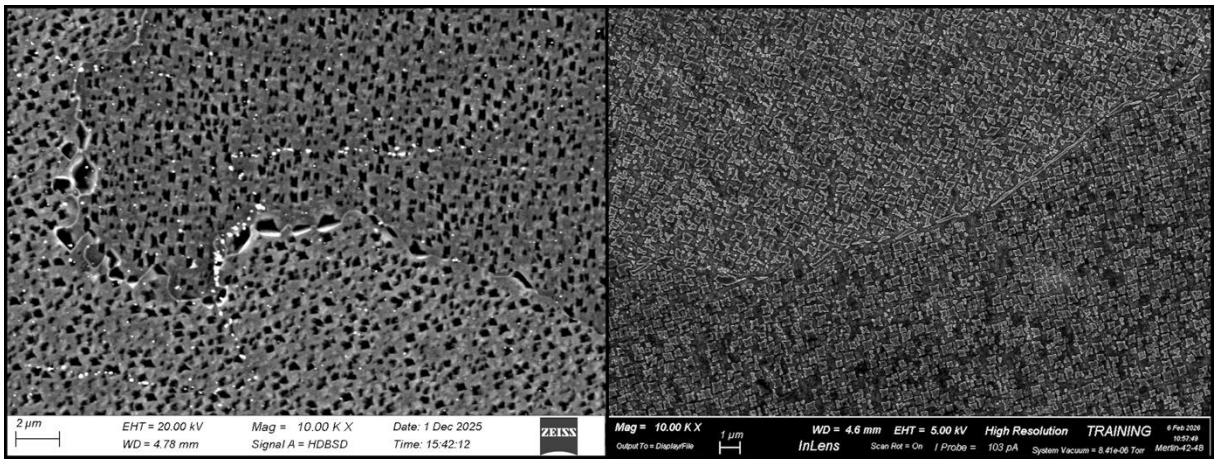

Figure 3.20: Focus on two grain boundaries: on the left there is a more serrated boundary of a sample HIP treated at 1220°C, on the right is highlighted a plate-like morphology of grain boundary of a sample HIP treated at 1240°C.

In addition to the analysis carried out in the vicinity of the grain boundaries, where the primary γ′ precipitates appear significantly coarser and characteristic dimensions in the range of 1-2 µm, the investigation was also applied to the grain interior through SEM and FE-SEM micrographs, as reported in Figure 3.21. All three samples of the experimental set showed the same γ′ morphological features. Namely, within the grains, it was possible to observe a massive population of secondary γ′ precipitates, which exhibited a markedly irregular and heterogeneous fan-like morphology, with typical sizes ranging between approximately 0.1-0.5 µm. This microstructural condition strongly deviates from the highly ordered and regular cuboidal distribution generally required for the optimization of high-temperature mechanical performance. Specifically, the last one is known to benefit from a uniform and well-aligned γ′ precipitate arrangement. Furthermore, the slow cooling step promoted the precipitation of a tertiary γ′ population, made of extremely fine particles with characteristic dimensions on the order of several tens of nanometres. These nanoscale precipitates are clearly distinguishable in the FESEM images, showing a multimodal γ′ size distribution throughout the microstructure.

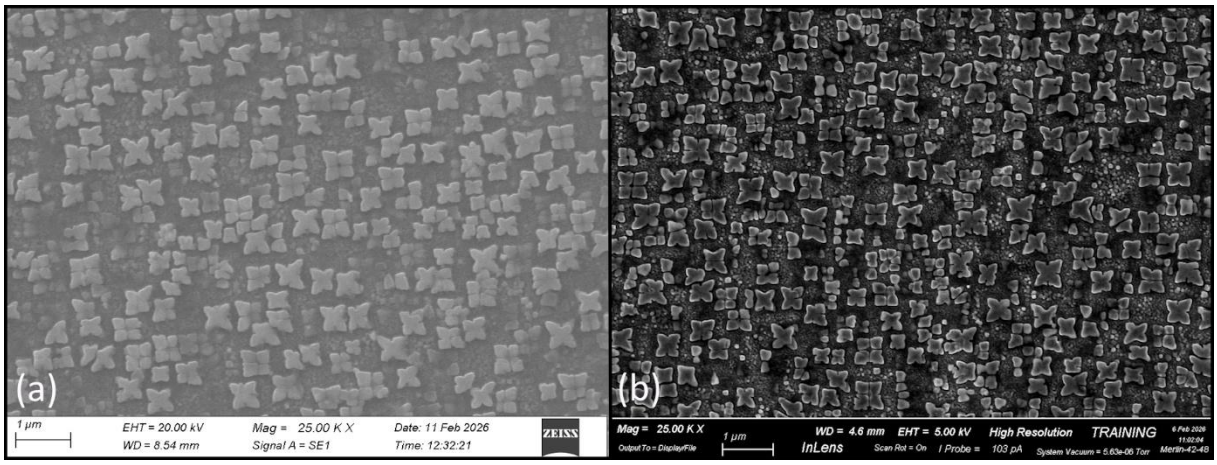

Figure 3.21: FESEM micrographs of HIP-treated SAM specimens processed at 100 MPa with a cooling rate of 20°C/min: (a) 1220°C treatment condition, (b) 1240°C treatment condition, illustrating the cuboidal γ′ precipitate morphology and their distribution within the γ matrix.

Figure 3.22 reports the results of the quantitative image analysis which analytically confirmed the multimodal γ′ precipitate size distribution. Due to the overall highly irregular morphology of the γ′ phase, the size distribution was statistically evaluated by considering the equivalent circular diameter of the individual precipitate areas, as determined using ImageJ. For the samples heat-treated at 1180 °C and 1220 °C, the resulting size distributions appear extremely broad and markedly asymmetric. It is possible to clearly observe a dominant primary peak centred at approximately 0.10 µm, accompanied by pronounced shoulders, or secondary peaks, extending towards larger equivalent diameters, up to about 0.40-0.50 µm. The lower relative intensity of these secondary peaks is entirely expected, since the number of such larger precipitates is significantly lower compared to the high density of extremely fine tertiary γ′ particles. Nevertheless, despite their lower number density, these coarser precipitates contribute predominantly to the overall γ′ volume fraction. The more intense peak observed in the distribution corresponding to the 1240 °C condition is mainly attributable to experimental factors. Specifically, conventional SEM was used to acquire the micrographs of samples A and B, while the images of sample C were obtained through FE-SEM, whose superior spatial resolution enabled the detection and accurate counting of a much larger population of fine tertiary γ′ precipitates, with a consequent influence on the resulting statistical distribution. Lastly, the total γ′ volume fraction remains approximately constant across all investigated heat treatment conditions, with values consistently close to 40%.

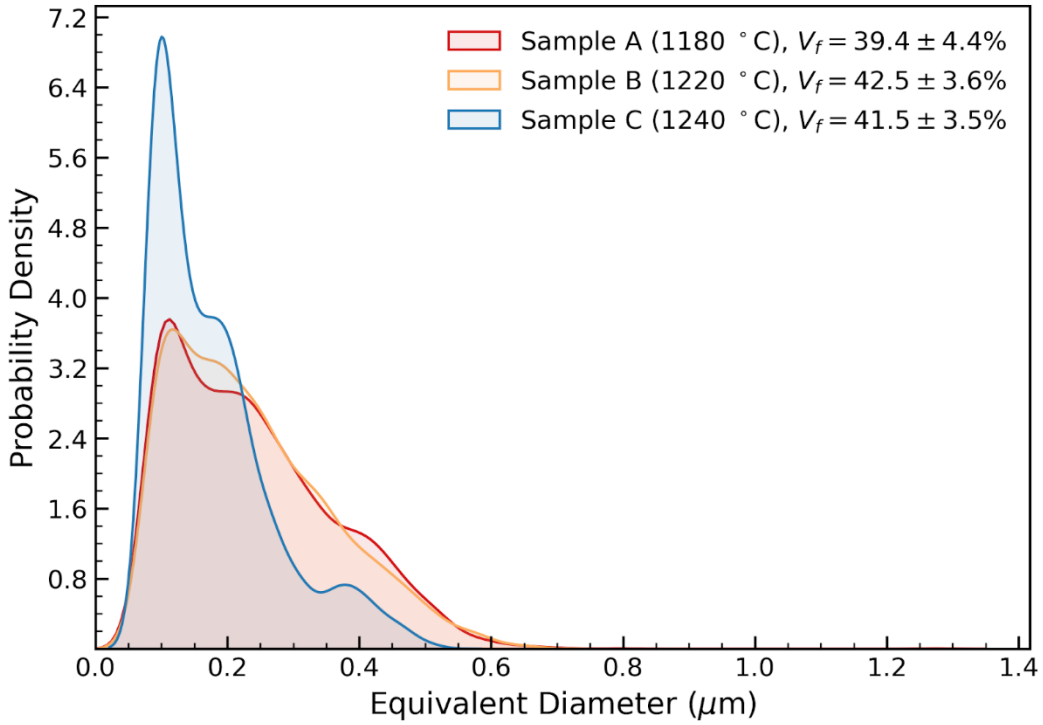

Figure 3.22: Probability density distribution of the equivalent diameters (µm) for HIP-ed samples at 100MPa-20C°/min and their volume fractions (V_f) are indicated.

Finally, Table 3.7 and Figure 3.23 present the average and standard deviation values of HBW hardness measured for the as-built and HIP-treated specimens. What emerges from these results is that the HIP-treated samples show a higher hardness than the as-built one. Although it might seem counterintuitive, the extremely fine-grained microstructure of the as-built sample leads to lower hardness values than the more coarse-grained microstructure, thanks to the

recrystallization of the HIP-treated samples. The explanation of this phenomenon, which deviates from the Hall-Petch relationship, is that the massive precipitation of the strengthening γ′ phase provides a greater contribution than grain size. Moreover, the low hardness values for the as-built condition are indicative of a good material ductility, which enhances the accommodation of thermal stresses during the printing process, with a consequent improvement of the material printability. As for the average hardness of the HIP-treated specimens, they all show values between 335 and 340 HBW, with a slightly higher for the sample treated at 1220°C. Since the samples have essentially the same total γ′ volume fraction, the more pronounced variability in their hardness values could derive from a partial recrystallization, with a consequent coexistence of regions with coarse and fine grains.

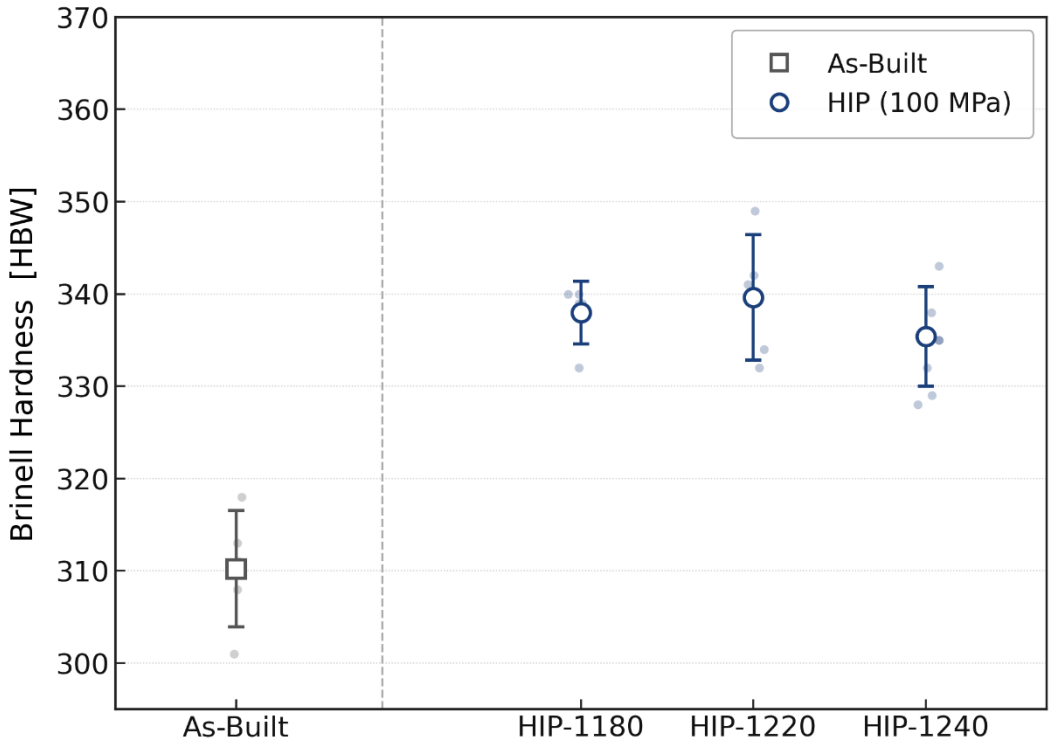

Figure 3.23: Brinell hardness (HBW) distribution across different sample conditions. The chart compares the baseline As-Built state with Hot Isostatic Pressing (HIP) treatment at 100 MPa-20°C/min.

Table 3.7: Average and standard deviation values of hardness (HBW) for different SAM samples HIP-ed at 100MPa-20°C/min.

	Av. Brinell H. [HBW]	St. Dev [HBW]
sample A (1180°C)	338.00	3.39
sample B (1220°C)	339.60	6.80
sample C (1240°C)	335.40	5.41

3.3.2. Samples HIP treated -150MPa-20°C/min

In order to evaluate the effectiveness of HIP in reducing defect content and refining the microstructure, the consolidation pressure was increased from 100 MPa to 150 MPa, while the remaining process parameters were kept unvaried. The applied experimental workflow was the same as in the previous set. As shown in Figure 3.24, residual porosity is still present in the core region along both the XZ building direction and the XY plane. Isolated coarse open pores were occasionally observed near the surface Figure 3.24 (c); however, since these defects are removed during subsequent machining, the porosity analysis was focused exclusively on the core regions.

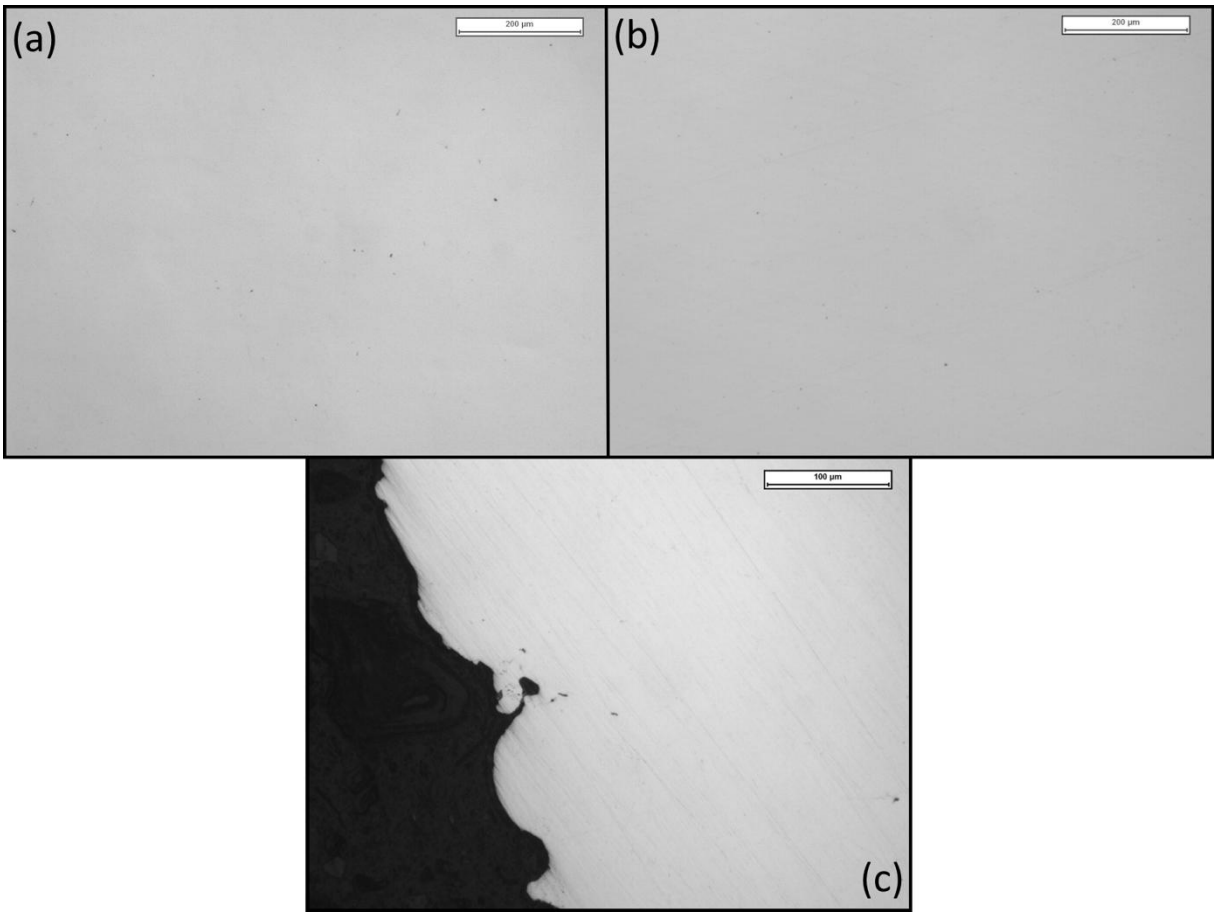

Figure 3.24: LOM images of the 1180°C at 150MPa of HIP-treated sample in as polish condition: (a) XZ cross-section, (b) XY cross-section, showing residual gas porosity localized within the core region and (c) open porosity at surface.

Figure 3.25 illustrates the frequency distribution of porosity sizes, expressed in terms of equivalent diameter classes, for the three investigated HIP temperatures along the XZ building direction. The analysis of the distributions clearly highlights the synergistic effect of elevated isostatic pressure (150 MPa) and temperature in promoting a substantial reduction in volumetric defects. In all three conditions, a log-normal trend is exhibited by the size patterns, with a dominant peak centred at approximately 1 µm. The increase in treatment temperature leads to a progressive decrease in the overall number density of pores, indicating an enhanced densification efficiency. This behaviour is fully consistent with the thermodynamic and kinetic mechanisms governing the HIP process. Specifically, higher temperatures promote increased atomic mobility and diffusion in the solid state, which facilitate plastic deformation and collapse of the pores, ultimately resulting in the effective "welding" of internal cavities. As summarized in Table 3.8, the average pore diameters remain approximately constant at around 2 µm for all three temperatures, which suggests that the main effect of temperature is associated with a reduction in pore population rather than a significant change in pore size.

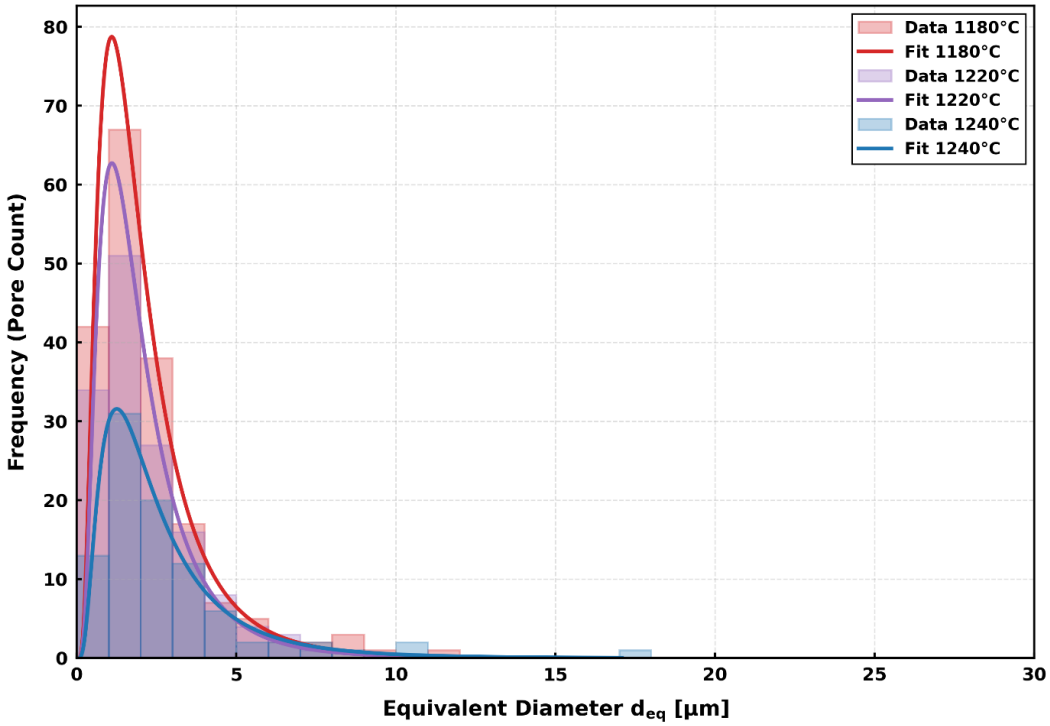

Figure 3.25: Frequency distribution of the equivalent pore diameter (d_{eq}) analysed on the XZ cross-section. The samples were treated by HIP at 150 MPa and three different temperatures: 1180°C, 1220°C, and 1240°C.

Table 3.8: Diameter defect analysis along XZ plane of samples HIP-treated at 150°C-20°C/min.

	Av. defects diameter [µm]	St. Dev [µm]
sample D (1180°C)	2.218	1.800
sample E (1220°C)	2.125	1.427
sample F (1240°C)	2.191	1.269

A similar behaviour is observed along the XY direction, as shown by the corresponding Figure 3.26 and summarized in Table 3.9. In this case, the porosity size distributions also follow a log-normal trend, showing comparable bandwidths at all investigated temperatures and a dominant peak centred between 1 and 2 µm. Interestingly, a slight inversion in the temperature-dependent trend is detected, with the sample treated at 1220 °C, which displays a higher pore number density at the peak compared to the specimen processed at 1240 °C. Nevertheless, the average equivalent pore diameters remain essentially constant at approximately 2 µm across all temperatures. Overall, these results, fully consistent with those obtained along the XZ building direction, indicate a high degree of homogeneity in the average defect size across both analysed planes, confirming the homogeneity of the HIP densification process.

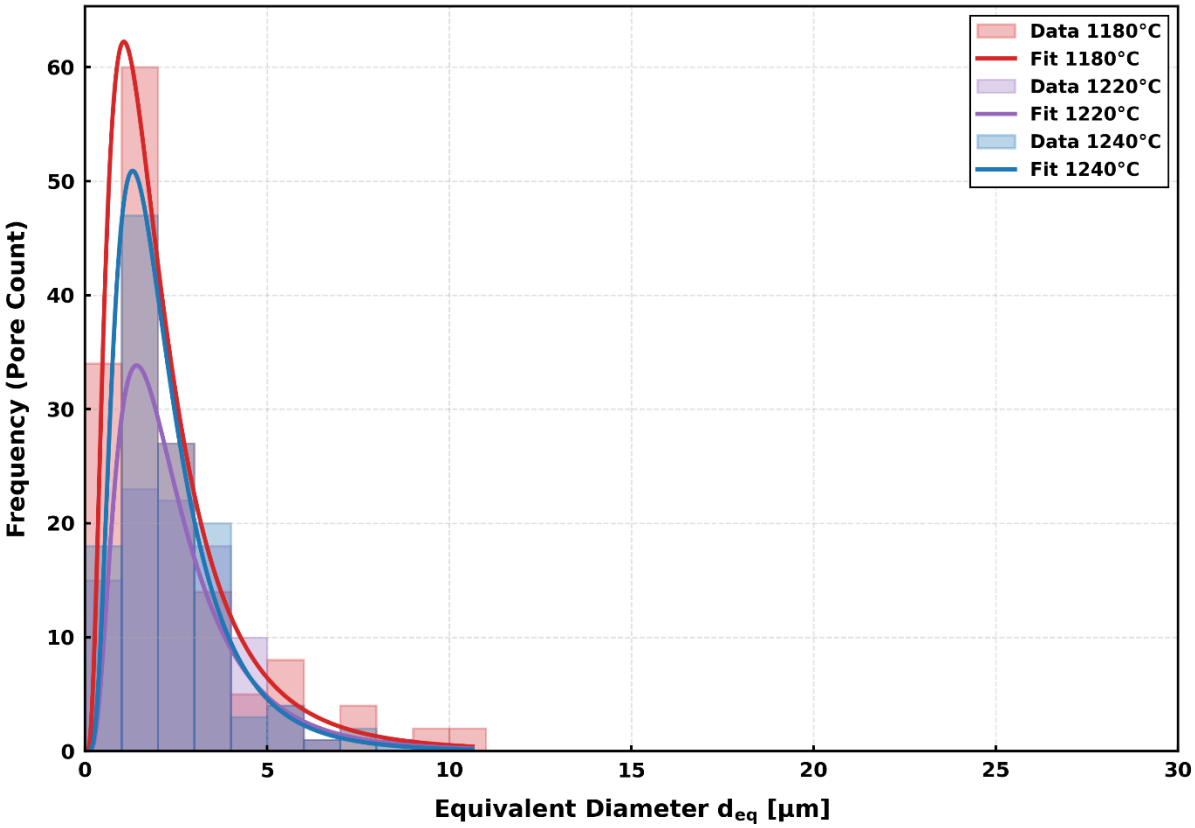

Figure 3.26: Frequency distribution of the equivalent pore diameter (d_{eq}) analysed on the XY cross-section. The samples were treated by HIP at 150 MPa and three different temperatures: 1180°C, 1220°C, and 1240°C.

Table 3.9: Diameter defect analysis along XY plane of samples HIP-treated at 150°C-20°C/min.

	Av. defects diameter [µm]	St. Dev [µm]
sample D (1180°C)	2.373	2.004
sample E (1220°C)	2.568	1.539
sample F (1240°C)	2.255	1.462

As shown in Figure 3.27, a further reduction in porosity is observed with the increase of temperature. Intensifying the applied pressure to 150 MPa results in a decrease in the overall porosity. In comparison with the condition at 100 MPa, at the intermediate temperature of 1220 °C the average porosity on the XZ plane decreases from 0.042% to 0.021% when a pressure of 150 MPa is applied. In addition to the improvement in terms of absolute densification, the higher pressure also leads to a considerable reduction in statistical variance, as evidenced by the narrower spread of the box plots. This indicates a more homogeneous microstructure. A levelling of the residual anisotropy between the two observation planes is promoted by the combined effect of elevated temperature and increased pressure. Consequently, the difference in porosity between the XZ and XY planes becomes negligible as confirmed in Table 3.10.

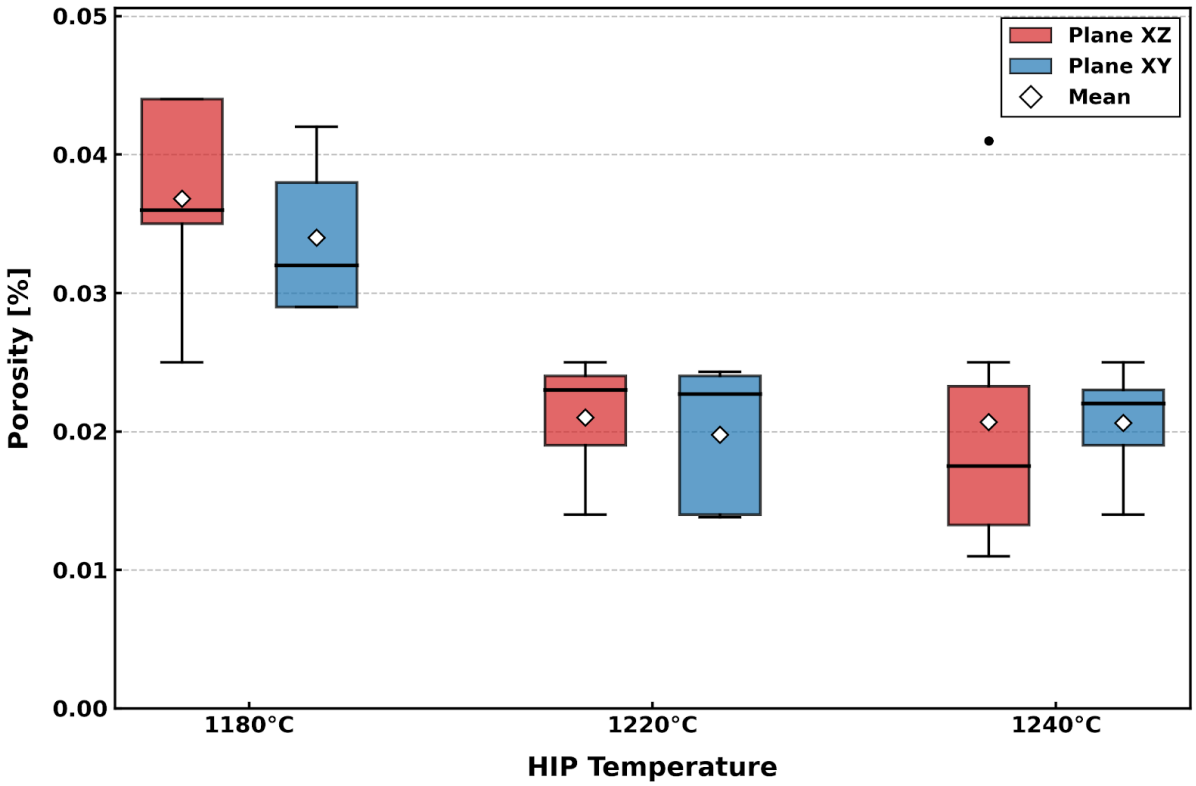

Figure 3.27: Box-plot statistical analysis of residual porosity (%) on XZ and XY planes for samples treated by HIP at 150Mpa and temperatures of 1180°C, 1220°C e 1240°C.

Table 3.10: Residual porosity (%) on XZ and XY planes of HIP-treated samples at 150°C-20°C/min.

	XZ Av. porosity [%]	St. Dev [%]	XY Av.porosity [%]	St. Dev [%]
sample D (1180°C)	0.037	0.0076	0.0034	0.0058
sample E (1220°C)	0.021	0.0045	0.020	0.0054
sample F (1240°C)	0.020	0.0112	0.020	0.0043

For a further confirmation of the homogeneity of pore morphology along both planes, the aspect ratio (AR) was evaluated Figure 3.28 and Table 3.11. The results show a stabilization of the average AR around 1.5, with a progressive reduction in standard deviation as the temperature increases, which indicates enhanced shape uniformity. The average AR suggests the predominance of not perfectly spherical defects with an AR slightly above 1. While HIP effectively reduces the equivalent pore diameter and total porosity, elongated defects mainly undergo progressive closure of the opposing surfaces, resulting in limited changes in pore elongation and hence a nearly constant AR.

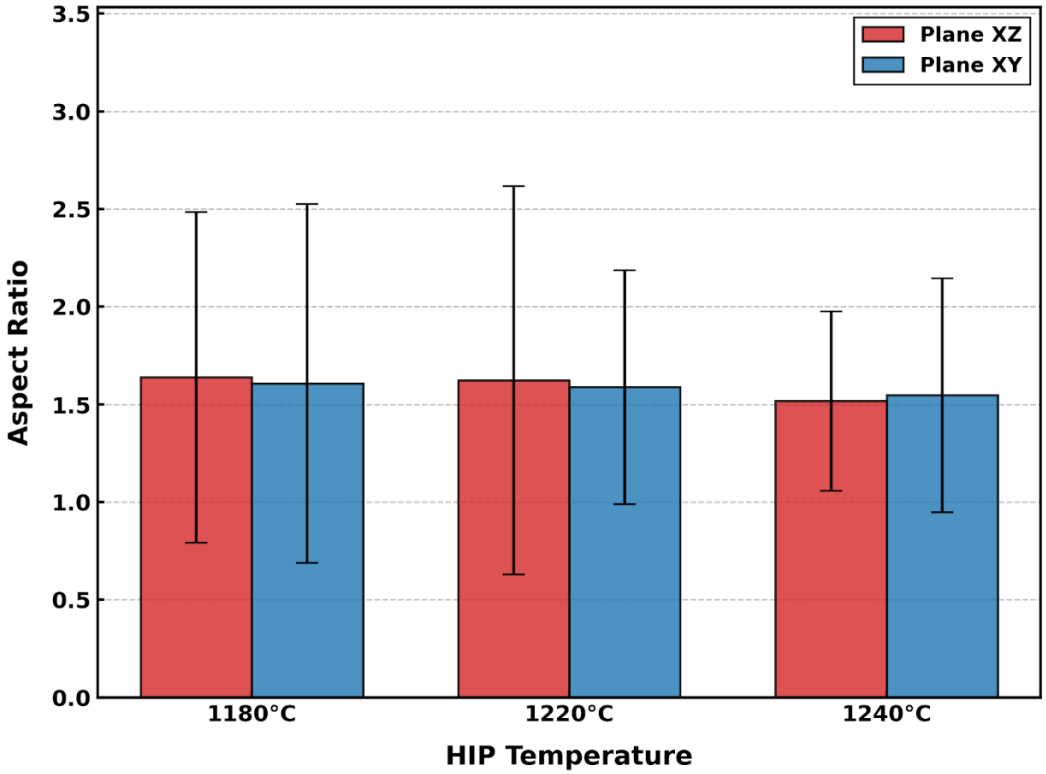

Figure 3.28: Average aspect ratio of pores, measured on XZ and XY planes for samples treated by HIP at 150Mpa and temperatures of 1180°C, 1220°C e 1240°C.

Table 3.11: Aspect ratio defect analysis along XZ and XY planes of HIP-treated samples at 100°C-20°C/min.

	XZ AR	St. Dev	XY AR	St. Dev
sample D (1180°C)	1.64	0.84	1.61	0.919
sample E (1220°C)	1.62	0.994	1.59	0.599
sample F (1240°C)	1.52	0.459	1.55	0.599

The study was further applied to investigate the effect of increasing pressure on the resulting grain microstructure. Figure 3.29 shows three representative micrographs of the specimens processed at three different temperatures and observed along the XZ plane. From a qualitative standpoint, a partial recrystallization can be clearly identified, as evidenced by the progressive dissolution of the characteristic as-built microstructural features, such as the cellular-dendritic substructure and the columnar grain morphology typical of the PBF-LB process. However, despite the increase in the applied pressure, a residual degree of microstructural anisotropy can still be observed along the direction of the thermal gradient imposed during solidification. This behaviour suggests the incompleteness of the recrystallization process and the strong influence of the prior solidification microstructure. Newly formed grains tend to nucleate with crystallographic orientations similar to those of the original grains, indicating a pronounced orientation memory effect. This phenomenon is primarily associated with the heterogeneous distribution of stored energy, locally maximized along melt pool boundaries where high dislocation densities accumulate during the rapid solidification process. Consequently, recrystallization preferentially initiates along these regions, leading to a directionally biased nucleation and growth process, commonly referred to as oriented recrystallization.

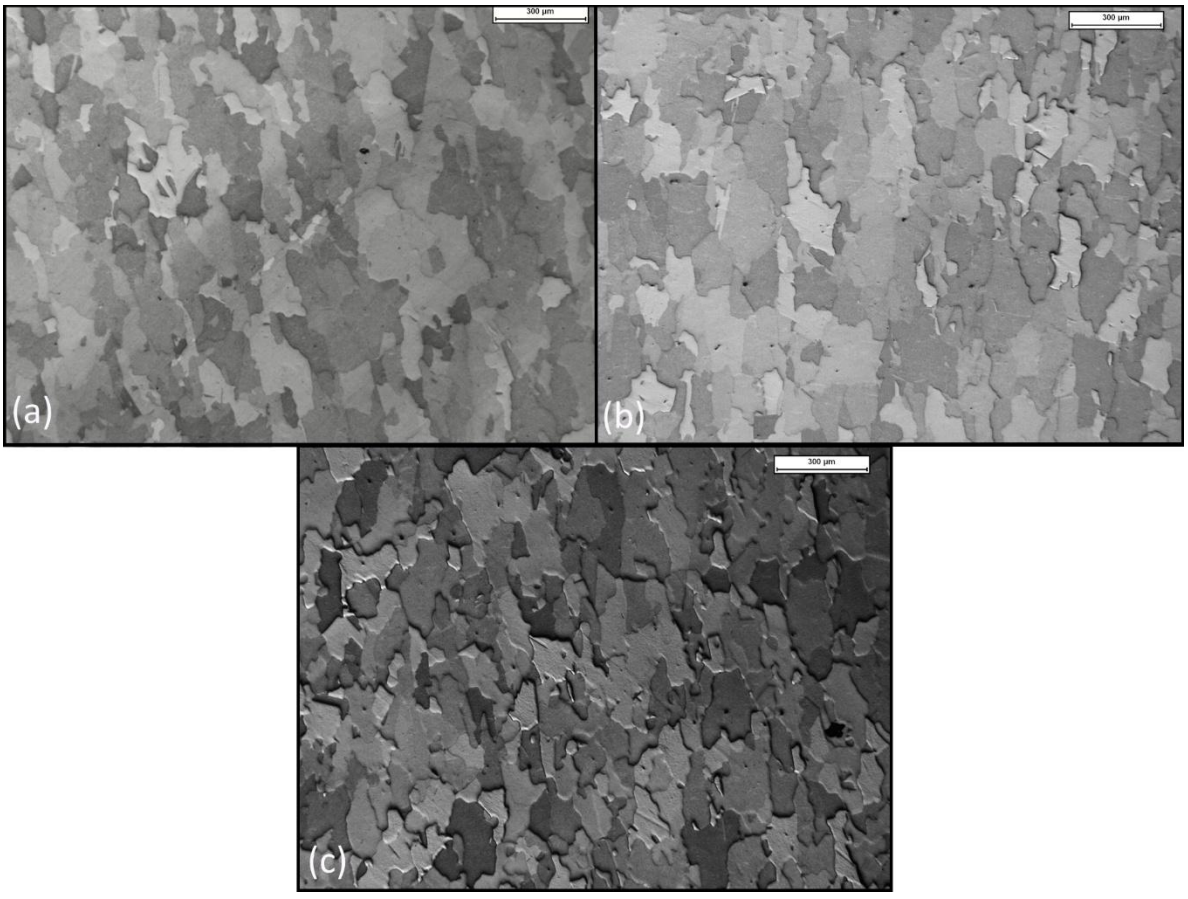

Figure 3.29: Optical microscopy images of etched SAM specimens subjected to HIP treatments at 150MPa along XZ plane at: (a) 1180 °C, (b) 1220 °C and (c) 1240 °C.

The data reported in Figure 3.30 (a) illustrate the evolution of grain size measured using the linear intercept method along the different reference directions. The results clearly highlight the presence of larger grains along the preferential growth direction, with values ranging between 100 and 125 µm, while the average grain size remains nearly constant at approximately 80 µm across the analysed processing temperatures. This behaviour suggests that, despite the thermal variations, there is no significant alteration of the overall grain refinement, while a directional dependence of grain growth is still retained. In Figure 3.30 (b), a progressive decrease in the aspect ratio (AR) is observed with increasing temperature, followed by a stabilization of the mean value around 1.5. This trend is accompanied by a reduction in data dispersion, indicating a narrower grain morphology distribution. Such behaviour is consistent with an enhanced degree of recrystallization at higher temperatures, leading to a more homogeneous and equiaxed grain structure. The combined decrease in AR and variability therefore suggests a gradual mitigation of microstructural anisotropy and an overall increase in grain uniformity.

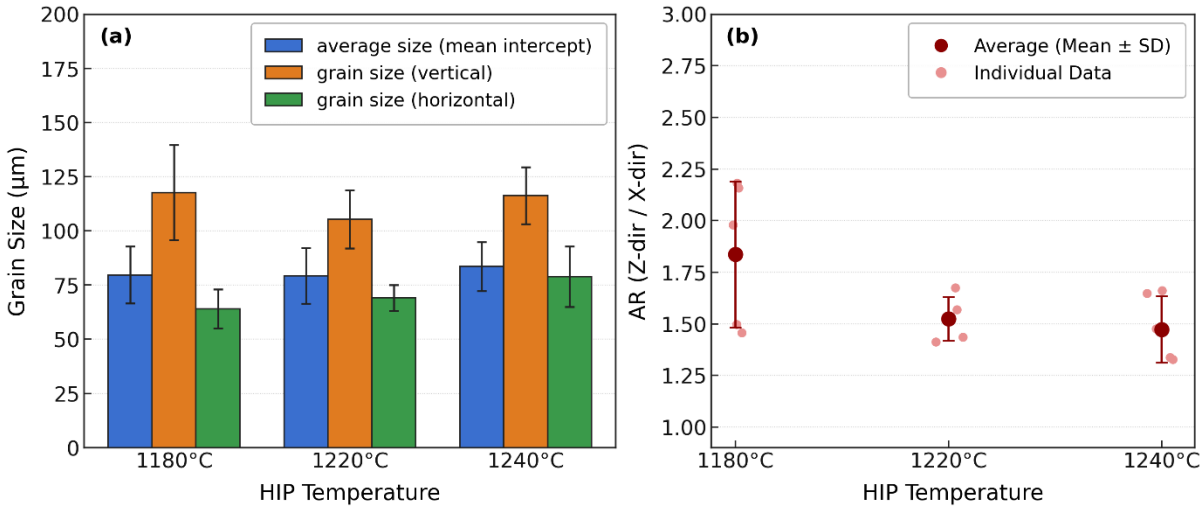

Figure 3.30:(a) Grain size evolution along XZ plane of the HIP-treated samples as a function of HIP temperature at 150MPa (b) Grain AR evolution along XZ of the HIP-treated samples as a function of HIP temperature at 150MPa.

The same methodological approach previously adopted for the 100 MPa experimental set was used for the grain size evaluation on the XY plane. Also in this case, to describe the three-dimensional grain morphology, each grain was geometrically approximated by an equivalent ellipse. When observed on the XY plane, however, the grains exhibit a more regular and nearly equiaxed morphology compared to the longitudinal sections, as shown in Figure 3.31.

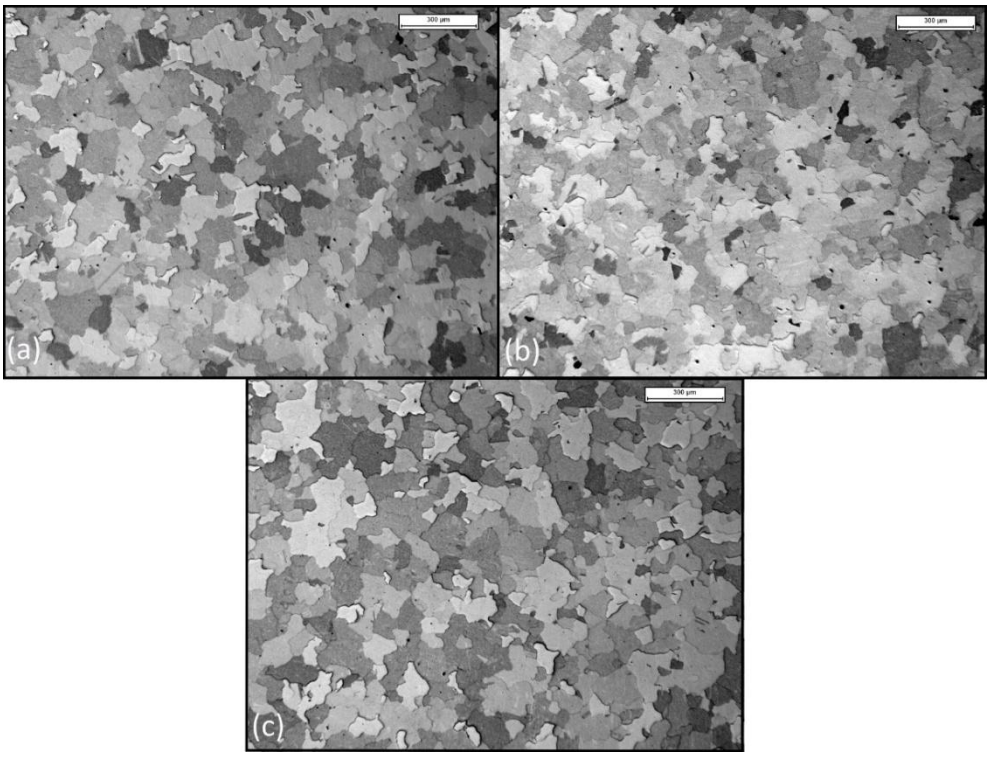

Figure 3.31: Optical microscopy images of etched SAM specimens subjected to HIP treatments at 150MPa along XY plane at: (a) 1180 °C, (b) 1220 °C and (c) 1240 °C.

For this reason, the average grain size was evaluated on this plane at the different processing temperatures, whereas the aspect ratio was not considered due to the nearly equiaxed in-plane morphology. The results in Figure 3.32, shows a clear increasing trend in the average grain size as the temperature rises from 1180 °C to 1220 °C, reaching values above 80 μm, in agreement with the behavior previously observed. However, at 1240 °C, this trend is reversed, similarly to what was observed for the 100 MPa condition. This inversion can be attributed to the activation of a more pronounced recrystallization process.

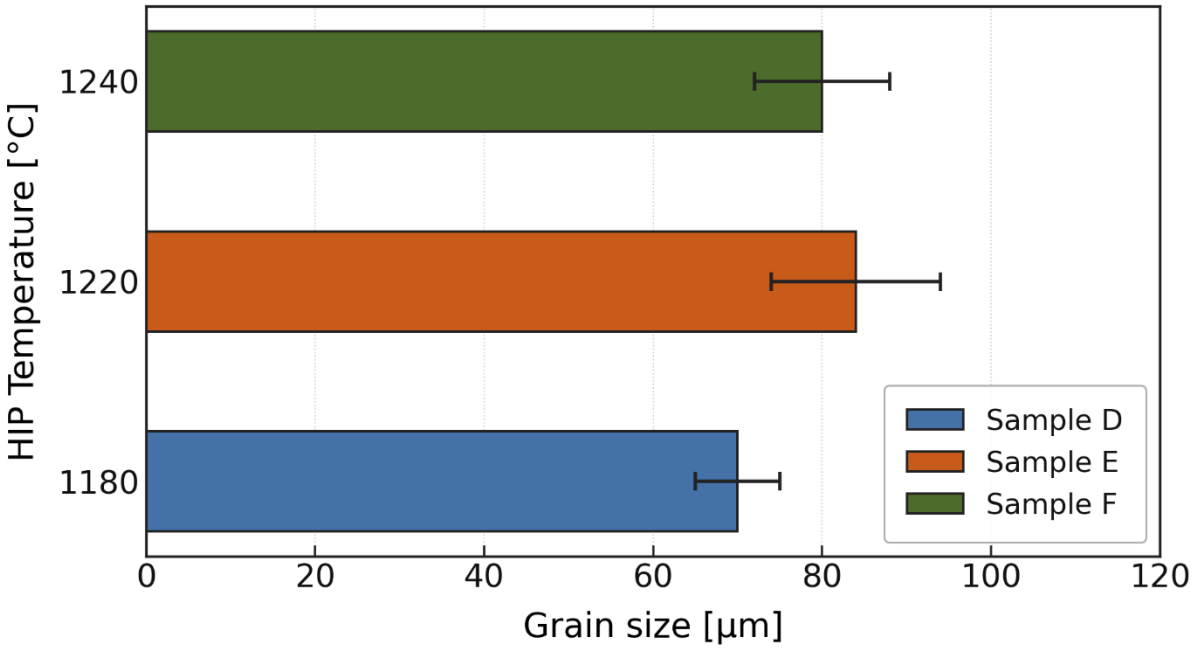

Figure 3.32: Grain size evolution along XY plane of the samples as a function of HIP temperature at 150MPa.

When the superalloy is cooled from supersolvus temperatures, γ′ nucleation is thermodynamically favoured at crystalline defects, such as triple junctions and grain boundaries. The method used to evaluate the effect of the presence of these larger precipitates at the boundaries and their associated distortion has been systematically revisited to each sample at its respective heat-treatment, as shown in Figure (3.33, 3.34, 3.35).

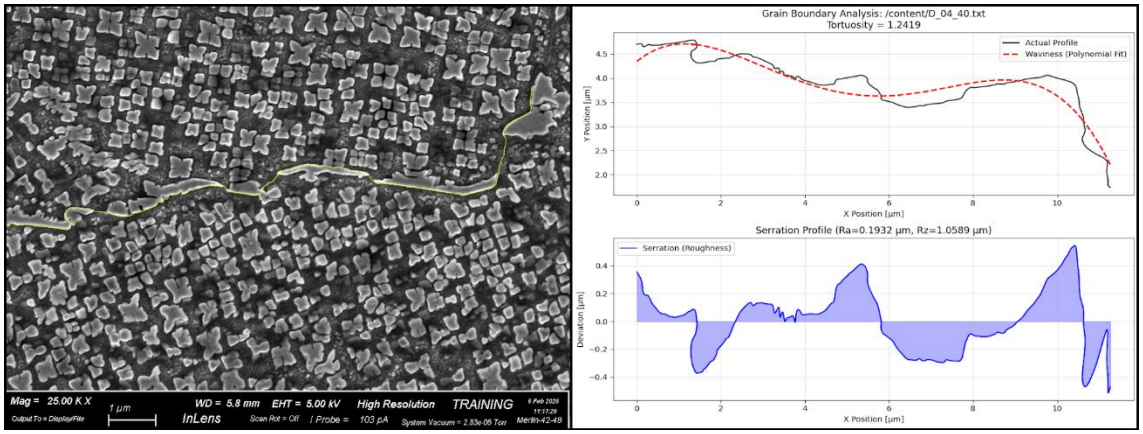

Figure 3.33: Grain boundary roughness evaluation method applied at one grain boundary of HIP-ed sample at 1180°C-150MPa-20C°/min.

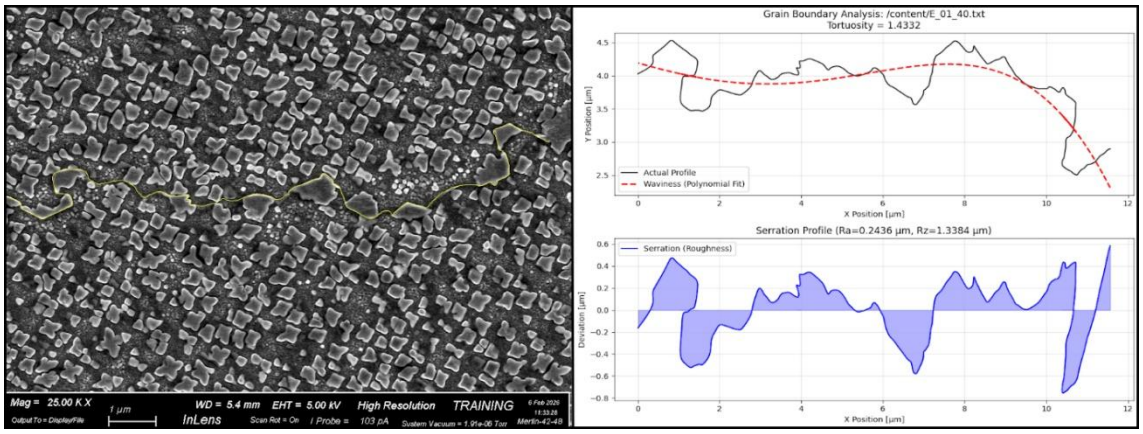

Figure 3.34: Grain boundary roughness evaluation method applied at one grain boundary of HIP-ed sample at 1220°C-150MPa-20C°/min.

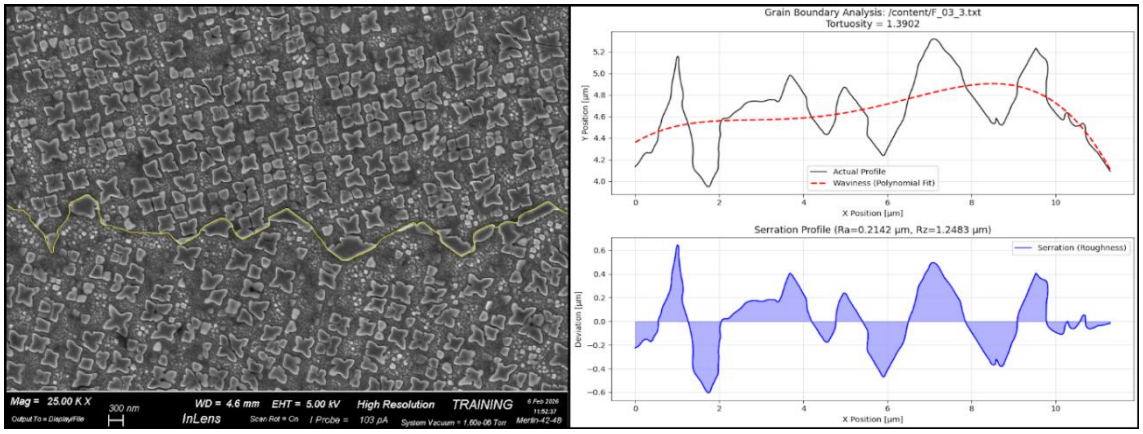

Figure 3.35: Grain boundary roughness evaluation method applied at one grain boundary of HIP-ed sample at 1240°C-150MPa-20C°/min.

The corresponding results can be read in Table 3.12, while Figure 3.36 illustrates a comparison between the present dataset and the experimental results previously obtained at a pressure of 100 MPa. Specifically, the box plots indicate a substantial overlap of all measured parameters with those of the previous experimental study, as well as a noticeable reduction in data scatter and a more compact distribution. Similarly to the previous case, it is possible to identify a slight decreasing trend of the characteristic serration parameters with the increase of the solution treatment temperature. This behaviour suggests that pressure does not significantly affect the precipitation kinetics and the associated grain boundary pinning, whereas temperature plays a dominant role with a consistent influence on all three parameters. At 1180 °C and 1220 °C, the distributions can be described as broad and centred at relatively high values, revealing pronounced grain boundary tortuosity and strong serration. The extended whiskers reflect the large data dispersion, characteristic of a localized Zener pinning mechanism, in which the interaction between discrete precipitates and migrating grain boundaries leads to geometrically irregular and statistically variable paths. Conversely, at 1240 °C, a marked decrease is revealed in both the average values and the statistical variance. This specific observation supports the hypothesis that, at higher temperatures, diffusion mechanisms could promote the coalescence of γ′ and evolve toward a straighter configuration.

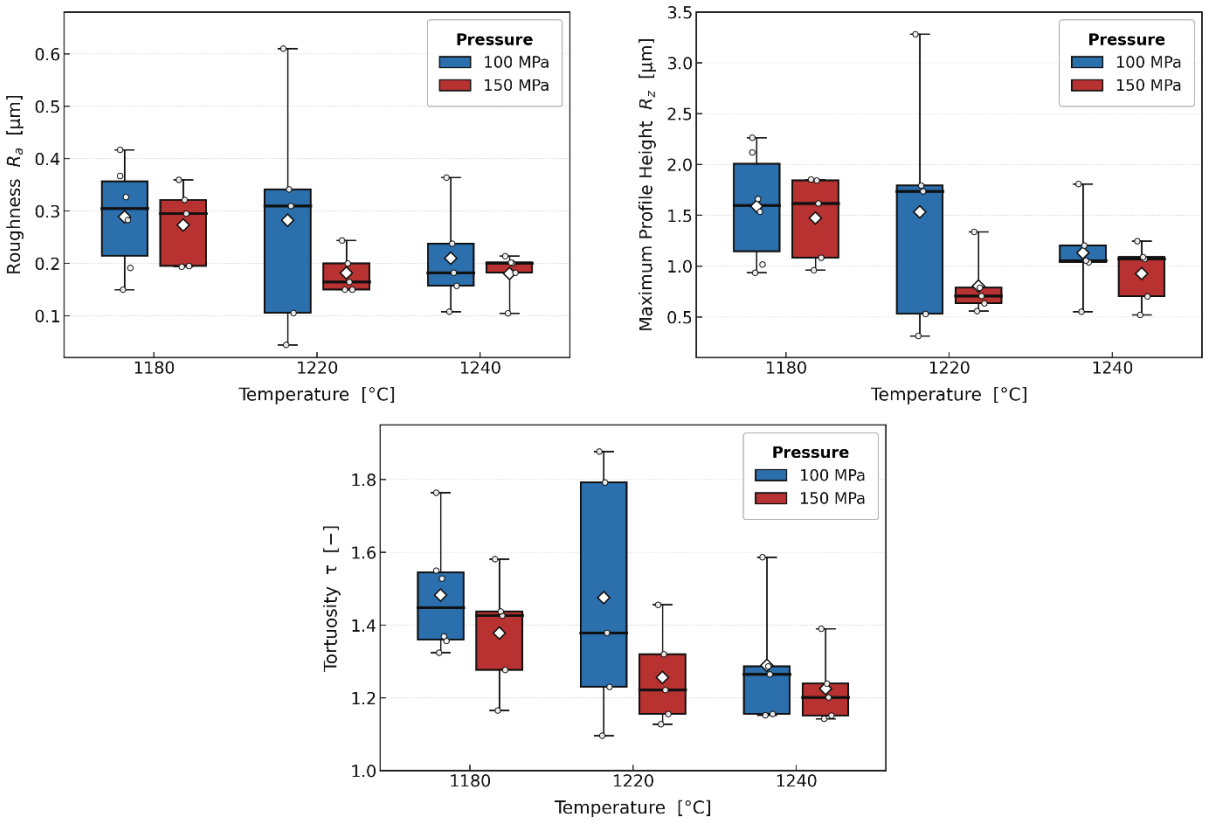

Figure 3.36: The image shows the box plots illustrating the trends of the three analysed parameters average Roughness (R_a), maximum profile height (R_z) and tortuosity (τ)as a function of the solution treatment temperature and the pressure applied during the HIP process (100 MPa vs 150 MPa).

Table 3.12: Grain boundary roughness evaluation method parameters of HIP-treated samples at 100°C-20°C/min.

	Av. R_a [µm]	St. Dev	Av. R_z [µm]	St. Dev	Av. τ [-]	St. Dev
sample D (1180°C)	0.289	0.102	1.589	0.548	1.482	0.166
sample E (1220°C)	0.282	0.223	1.531	1.190	1.475	0.344
sample F (1240°C)	0.210	0.098	1.131	0.45	1.289	0.177

Figure 3.37,shows an intragranular γ′ morphology substantially consistent across all samples of the experimental set. Specifically, well-defined cuboidal and regularly arranged precipitates, i.e. secondary γ′, are occasionally observed, separated by narrow γ channel features that are typically considered optimal for maximising the thermomechanical performance of Ni-based superalloys. However, such an ideal microstructural configuration is only sporadically detected. In most cases, what characterises the strengthening phase is a less regular morphology showing

fan-like, triangular, rounded, and generally irregular shapes. Therefore, during the cooling phase, non-uniform precipitation and growth conditions are observed, indicating a deviation from the ideal cuboidal arrangement. In contrast, tertiary γ′ precipitates are distributed withinthe γ matrix, decorating the regions between secondary γ′ particles in the form of very fine dispersions.

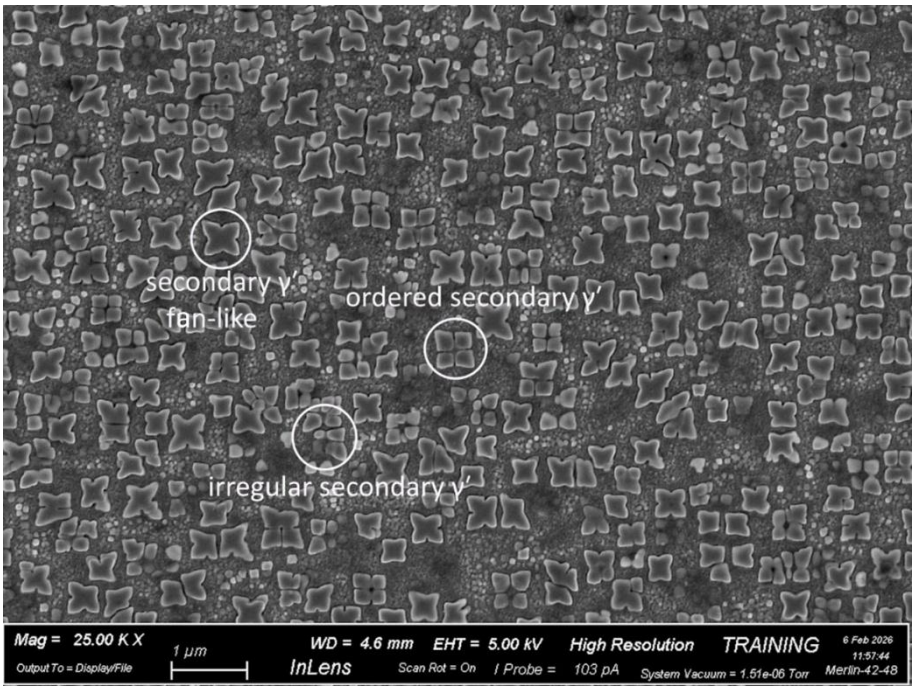

Figure 3.37: FESEM micrograph illustrating the γ′ precipitate microstructure of the SAM alloy after HIP treatment at 1220°C, 150 MPa, and a cooling rate of 20°C/min.

In this case, image analysis was performed on FESEM micrographs, enabling the quantification of most of the tertiary γ′ precipitates, although not all of them due to their extremely fine size. The use of an extremely aggressive thresholding procedure would have resulted in the artificial merging of adjacent fine precipitates, leading to an overestimation of particle size by assigning a single equivalent diameter to clusters of multiple tertiary γ′ particles. In order to avoid this artifact, a controlled segmentation approach was adopted. Given the predominantly irregular morphology of the precipitates, the image analysis was carried out by extracting the equivalent circle diameter of the identified particle areas as the representative size parameter. The resulting relative size distributions reveal essentially the same precipitate population across all three samples. Through this analysis it was possible to resolve ultrafine tertiary γ′ particles down to approximately 0.035 µm under all investigated conditions. In the Figure 3.38, the size distribution curves clearly indicate a multimodal behaviour. A pronounced peak is observed in the ultrafine size range 0.05-0.10 µm, which can be attributed to the extensive re-precipitation of tertiary γ′, or possibly to very fine secondary γ′. At larger equivalent diameters, two additional but less intense peaks are evident at approximately 0.2 µm and 0.4 µm. These populations contribute predominantly to the overall γ′ volume fraction. The total γ′ volume fraction (V_f) ranges between 39% and 44%, which is in excellent agreement with the values previously measured for the 100 MPa condition.

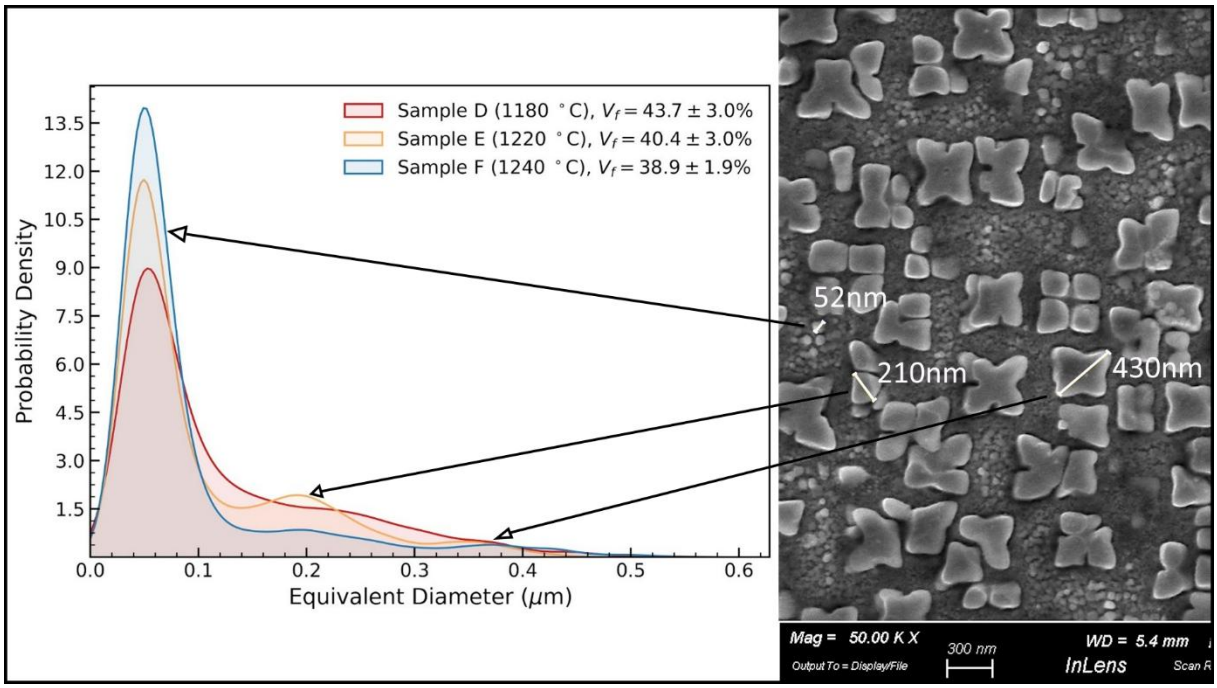

Figure 1.38: Probability density distribution of the equivalent diameters (μm) for HIP-ed samples at 150MPa-20C°/min and their volume fractions (V_f) are indicated.

Apparently, the application of increased pressure did not significantly affect the growth kinetics of the γ′ precipitates. This conclusion is further supported by the hardness measurements, which closely replicate the values obtained under the lower-pressure condition, as shown in Figure 3.39 and Table 3.13. The superposition of the datasets is not limited to the average hardness values; the corresponding standard deviations also show a nearly identical trend. This consistent mechanical response is coherent with the negligible differences observed in both the total γ′ volume fraction and the equivalent diameter distributions between the two experimental sets.

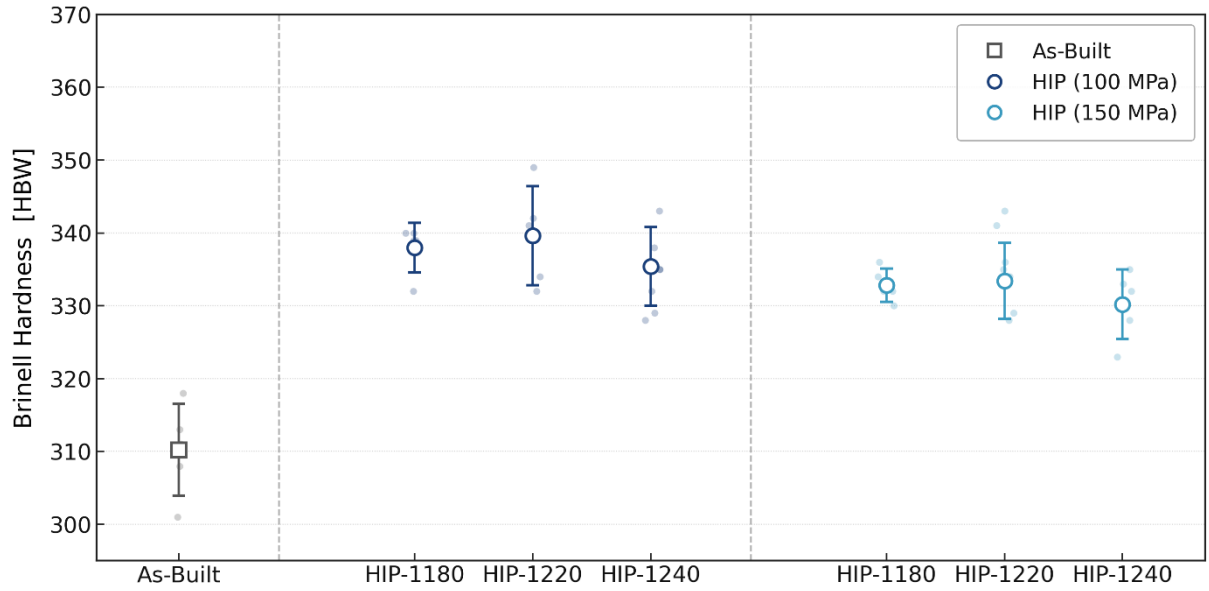

Figure 3.39: Brinell hardness (HBW) distribution across different sample conditions. The chart compares the baseline As-Built state with Hot Isostatic Pressing (HIP) treatment at 100 and 150 MPa-20C°/min.

Table 3.13: Average and standard deviation values of hardness (HBW) for different SAM samples HIP-treated at 150MPa-20°C/min.

	Av. Brinell [HBW]	St. Dev [HBW]
sample D (1180°C)	332.80	2.28
sample E (1220°C)	333.40	5.22
sample F (1240°C)	330.20	4.76

3.3.3. HIP-treated samples at 100 MPa vs 150 MPa -20 °C/min

A comparative analysis of the two experimental sets reveals a clear influence of temperature and pressure on the pore size distribution. Specifically, both parameters contribute to a leftward shift of the log-normal distribution curve toward lower equivalent diameter values, accompanied by a downward shift in terms of pore count. With reference to overall porosity, it is possible to observe a reduction in residual porosity of approximately 0.01–0.02%. Despite the negligibility of this variation in absolute terms, it becomes significant when considered in the context of the ambitious target of achieving a defect-free material: transitioning from 99.96% to 99.98% density represents a meaningful advancement toward this goal. Furthermore, the decrease in mean porosity is accompanied by a measurable reduction in variance, evidenced by the narrowing of the box plots in Figure 3.40, which indicates an improvement in the spatial homogeneity of defects within the material.

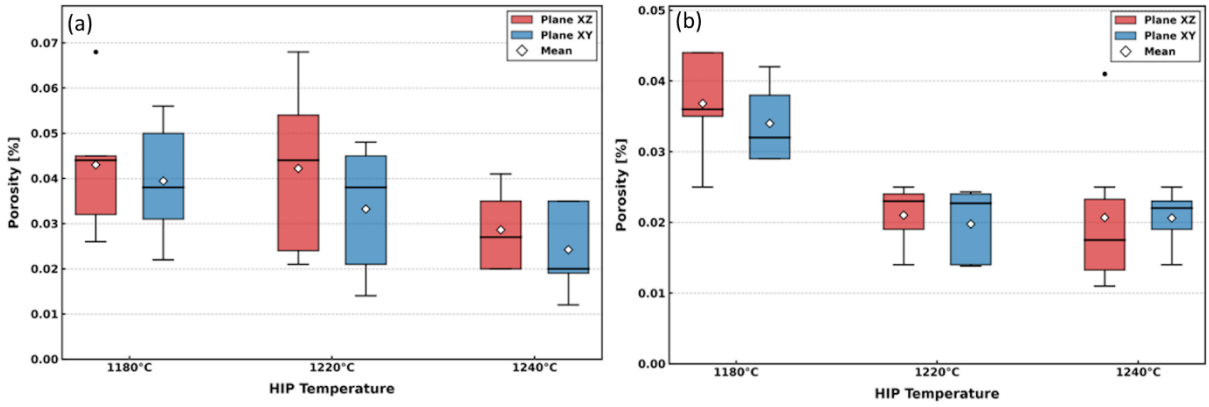

Figure 3.40: Box plot distribution of porosity fraction measured on the XZ and XY planes as a function of HIP temperature: (a) first experimental set at 100 MPa, (b) second experimental set at 150 MPa.

With regard to the remaining microstructural features, the increase in pressure does not produce a significant effect the grain size or morphology, nor on γ′ precipitation in terms of volume fraction or morphological characteristics. The same conclusion holds at the grain boundary level, where precipitate morphology and its contribution to boundary tortuosity are fully comparable to those observed at the reference pressure of 100 MPa. This is corroborated by the parameters extracted through the grain boundary evaluation method, confirming that precipitation kinetics are governed primarily by temperature rather than pressure. Figure 3.41 illustrates representative images of two grain boundaries processed at the same temperature but under different applied pressures, presented for comparative purposes. The uniformity of the microstructural characteristics was further confirmed by means of hardness values and standard deviations that are in close accordance with the two conditions.

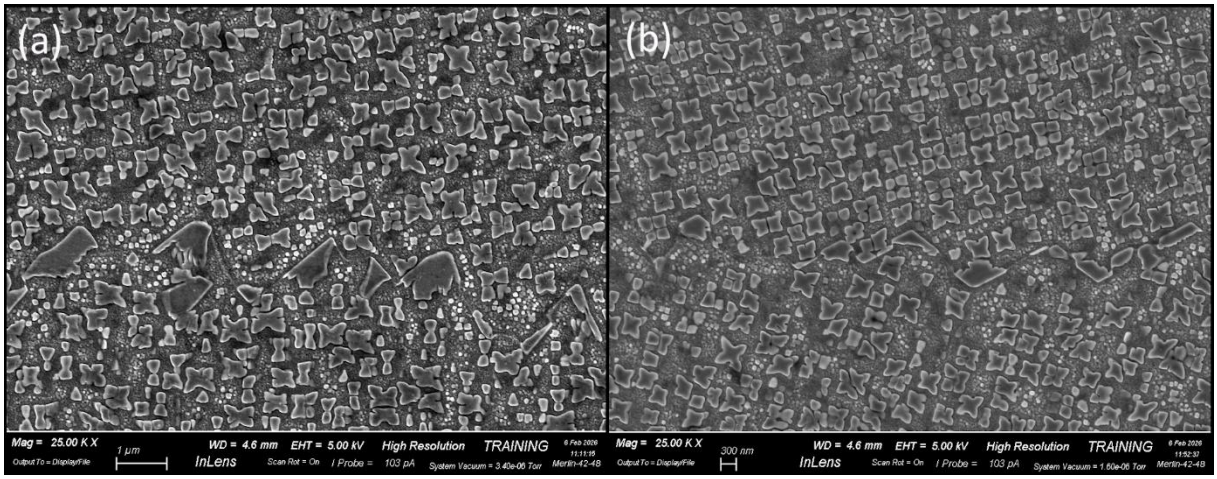

Figure 3.41: FESEM micrographs showing a comparative analysis of grain boundary morphology: (a) 1240°C-100MPa-20°C/min, (b) 1240C°-150MPa-20°C/min.

After assessing the benefits associated with increased processing pressure, it must be noted that, from an industrial standpoint, this approach does not constitute a viable pathway. A pressure increase of this magnitude would introduce a disproportionate rise in operational costs relative to the marginal improvements achieved in residual porosity. As a consequence to these considerations, it was decided to proceed with the HIP-Quench treatment using the same temperature set, at a pressure of 100 MPa and a cooling rate of 120 °C/min.

3.3.4. Samples HIP-Quench treated 100MPa – 120 °C/min

Figure 3.42 shows defect analysis images from the 1220°C HIP-Q sample surface, where spherical gas pores of small diameter are visually identifiable along both the XZ and XY planes.

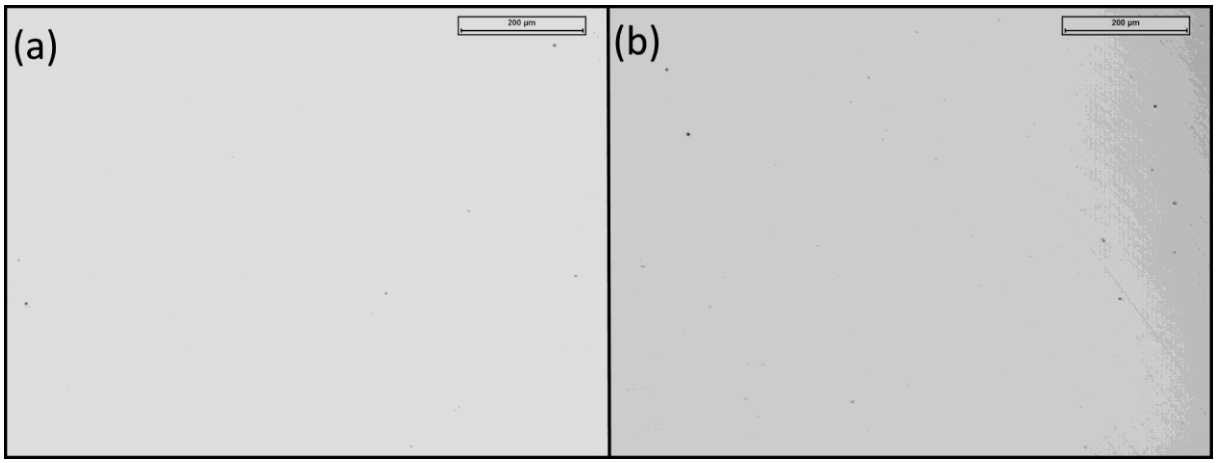

Figure 3.42: LOM images of the 1220°C HIP-Q sample in as polish condition: (a) XZ cross-section, (b) XY cross-section, showing residual gas porosity localized within the core region.

Figure 3.43. Frequency distributions of the equivalent pore diameter along the XZ and XY cross-sections exhibit a log-normal trend, in agreement with the behaviour reported for the previous experimental sets. In the XZ plane, a progressive leftward shift of the distribution curves is observed with increasing HIP temperature, indicating a systematic reduction in mean pore size. Along the XY plane, the primary effect is a decrease in the peak intensity, reflecting a lower overall pore count. In both cases, the distribution peak remains stable within the 1-2 µm size class, and the mean equivalent diameter across both planes is consistently close to 2 µm. Notably, all detected pores fall below 9 µm in equivalent diameter, with no evidence of anomalous or large-scale defects. The average defect diameters are summarized in Table 3.14. Furthermore, the close agreement between the XZ and XY distributions suggests a substantially isotropic pore morphology, with no preferential orientation introduced by the HIP-Quench thermal cycle.

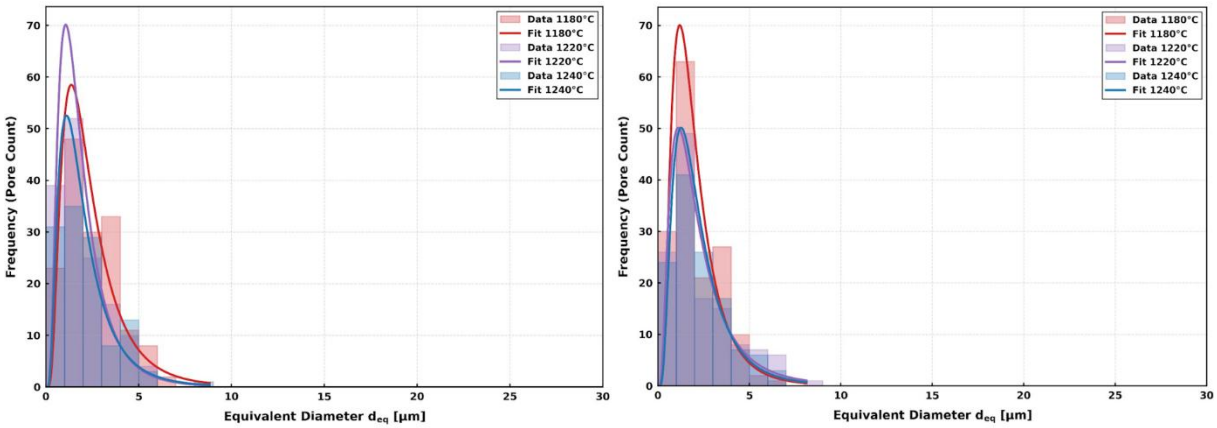

Figure 3.43 Frequency distribution of the equivalent pore diameter (d_{eq}) analysed on the XZ (a) and XY (b) cross-section. The samples were treated by HIP-Quench at 100 MPa and three different temperatures: 1180°C, 1220°C and 1240°C.

Table 3.14: Diameter defect analysis along XZ and XY plane of samples HIP-Q at 100°C-120°C/min.

	XZ Av.defects diameter [μm]	St. Dev [μm]	XY Av. defects diameter [μm]	St. Dev [μm]
sample G (1180°C)	2.44	1.38	2.37	1.68
sample H (1220°C)	1.98	1.25	2.30	1.44
sample I (1240°C)	2.12	1.43	2.07	1.24

An increase in the cooling rate does not lead to significant variations in the residual porosity. As observed in the previous conditions, the plot shown in Figure 3.44 illustrates a slight decrease in porosity with increasing temperature, accompanied by a progressive reduction in statistical variance. Overall, the residual porosity stabilises within a very narrow range between approximately 0.03% and 0.02%. Regarding pore morphology, all three samples exhibit an essentially constant aspect ratio along both analyzed planes, with an average value of approximately 1.4. Furthermore, the close agreement between the XZ and XY distributions indicates a substantially isotropic pore morphology within the material. The results obtained are fully in agreement with those observed under slower cooling conditions, as shown in Table 3.15. This behaviour can be explained by the fact that densification during HIP primarily occurs during the high-temperature holding stage, when the combined action of temperature and pressure promotes pore closure through plastic deformation and solid-state diffusion. Consequently, by the time the cooling stage begins, most of the internal porosity has already healed. For this reason, the cooling is not considerable as a controlling parameter for the densification process.

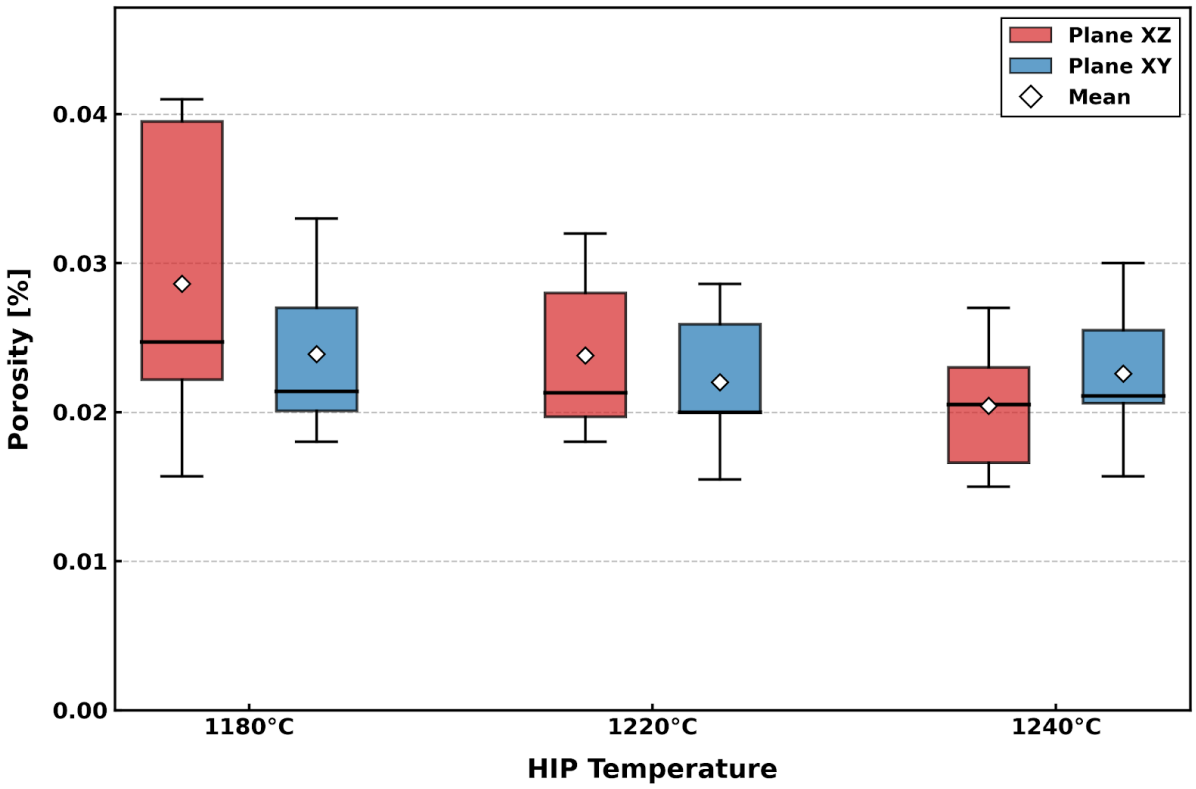

Figure 3.44: Box-plot statistical analysis of residual porosity (%) on XZ and XY planes for samples treated by HIP-Quench at 100MPa and temperatures of 1180°C, 1220°C and 1240°C.

Table 3.15: Residual porosity (%) on XZ and XY planes of HIP-treated samples at 150°C-20°C/min.

	XZ Av. porosity [%]	St. Dev [%]	XY Av.porosity [%]	St. Dev [%]
sample G (1180°C)	0.029	0.011	0.024	0.006
sample H (1220°C)	0.024	0.006	0.022	0.005
sample I (1240°C)	0.020	0.005	0.023	0.005

As in previous cases, Figure 3.45 reveals a clear microstructural anisotropy that is preserved across all investigated temperatures.

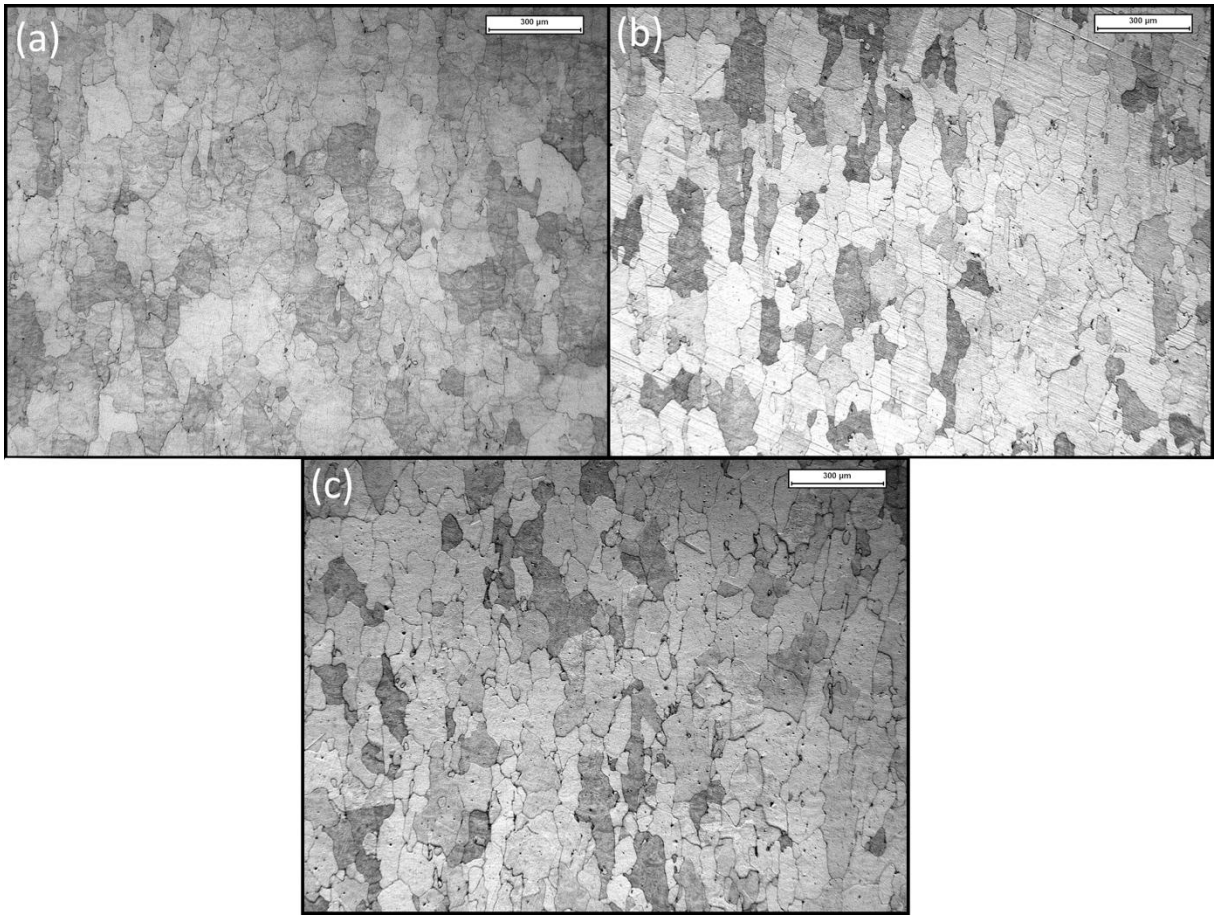

Figure 3.45: Optical microscopy images of etched specimens subjected to HIP treatments at 100MPa along the XZ plane at: (a) 1180 °C, (b) 1220 °C and (c) 1240 °C.

The grain size measured along the vertical direction is consistently and significantly larger than that measured along the horizontal direction. As the HIP temperature increases from 1180°C to 1220°C, it is possible to observe a grain coarsening phenomenon, with the overall mean grain size increasing from ~76.7 µm to ~81.1 µm. At 1240°C, the mean grain size drops sharply to ~62.7 µm as shown in Figure 3.46(a), suggesting the onset of static recrystallization driven by the dissolution of secondary phases that at lower temperatures exerted a pinning effect on grain boundaries. Finally, the analysis of the aspect ratio is shown in Figure 3.46(b); it can be noted that despite the pronounced grain refinement at 1240°C, the mean aspect ratio settles at approximately 1.57. Supported by the broad scatter of individual measurements, this value confirms that the columnar grain morphology has not been fully eliminated by the thermal treatment, and that a degree of residual anisotropy is retained within the material.

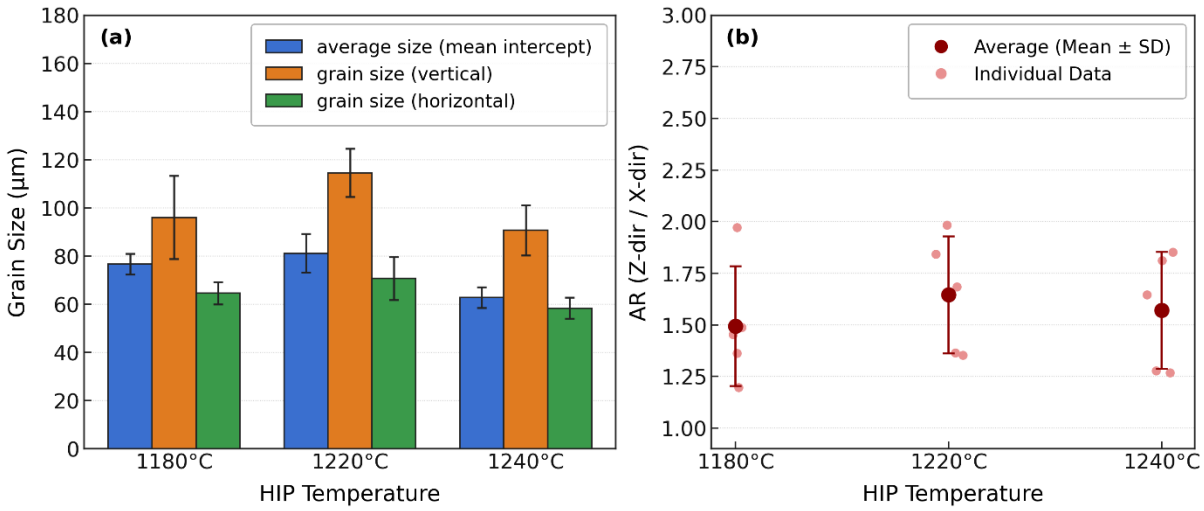

Figure 3.46: (a) Grain size evolution along XZ plane of the HIP-Quenched samples as a function of HIP temperature at 100MPa (b), Grain AR evolution along XZ of the HIP-treated samples as a function of HIP temperature at 100MPa.

The analysis of the microstructure in Figure 3.47 shows how, along the XY cross-section, the average grain size evolves with the HIP temperature. At 1180°C and 1220°C, the mean grain sizes are nearly identical, measuring 78.4 µm and 78.5 µm, respectively and indicating that no appreciable grain growth or refinement occurs within this thermal window. As the temperature increases to 1240°C, a clear microstructural change is observed: the average grain size drops to 62.2 µm, suggesting the onset of a different grain evolution mechanism at this condition. Figure 3.48 presents a comparative overview of the grain microstructure obtained at 1220°C and 1240°C, respectively. This result suggests that, also in the case of recrystallization kinetics, temperature represents the dominant controlling parameter.

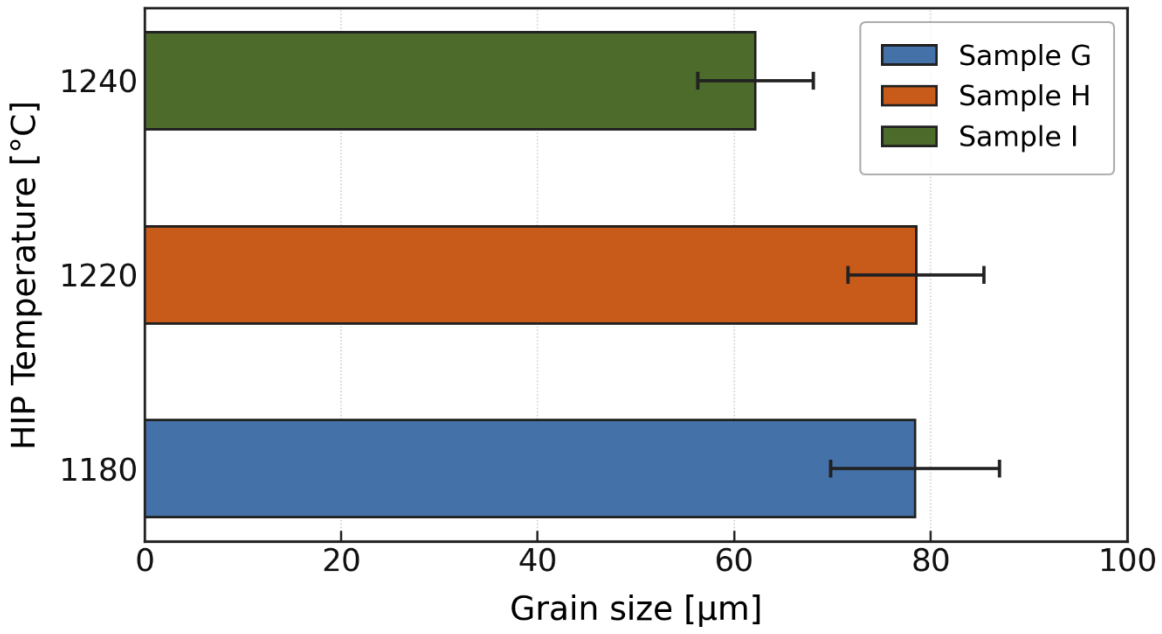

Figure 3.47: Grain size evolution along the XY plane of the samples as a function of HIP-Q temperature at 100MPa.

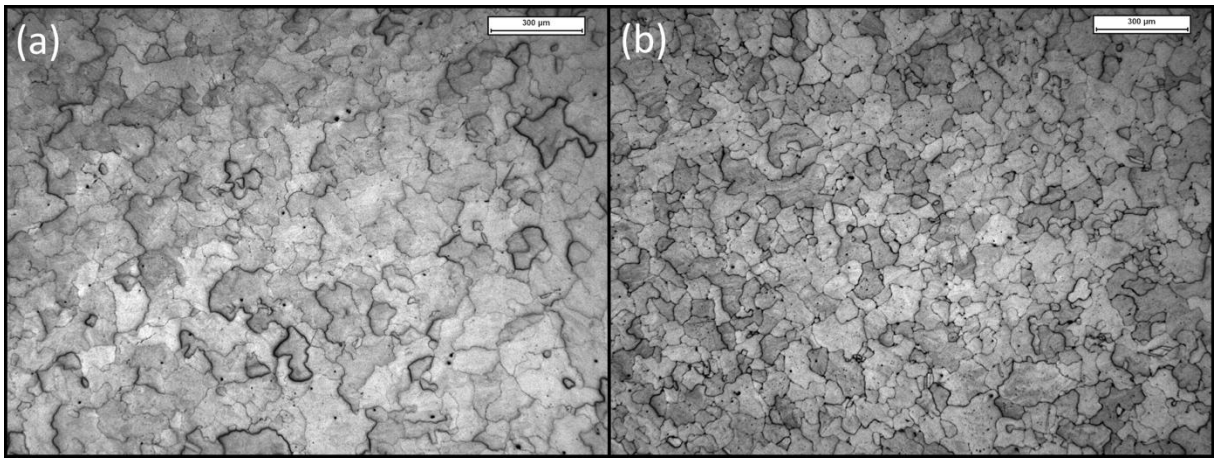

Figure 3.48: Grain structure along XY plane of HIP-Quenched samples:(a)1220°C-100MPa-20C°/min, (b)1240°C-100MPa-20C°/min

With reference to the precipitation kinetics of the γ′ phase along boundaries, its effect on GB serration level was again investigated through the GB roughness evaluation method. Figures (3.49, 3.50, and 3.51) show some examples of graphical output from the semi-automatic method.

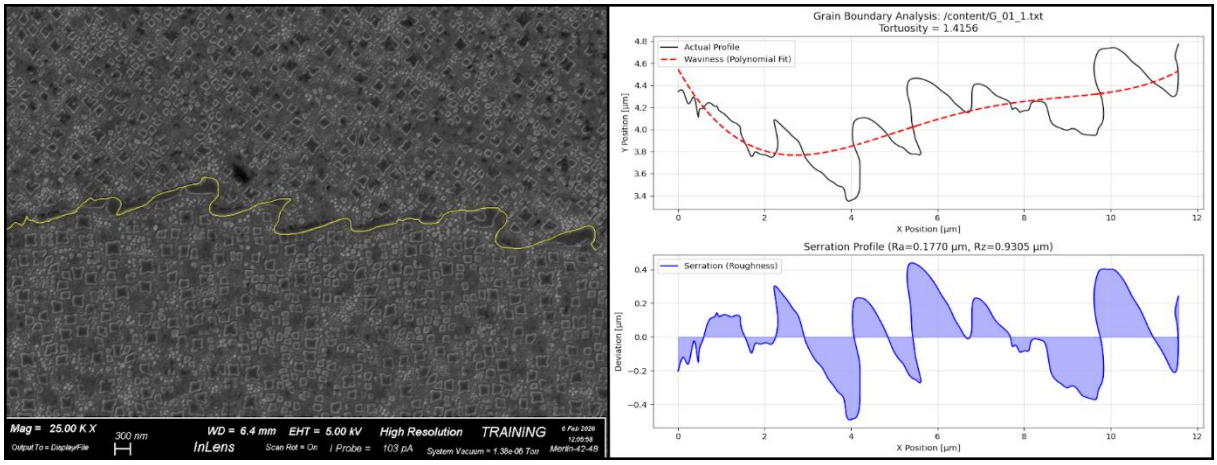

Figure 3.49: Grain boundary roughness evaluation method applied at one grain boundary of HIP-Quenched sample at 1180°C- 100MPa-120C°/min.

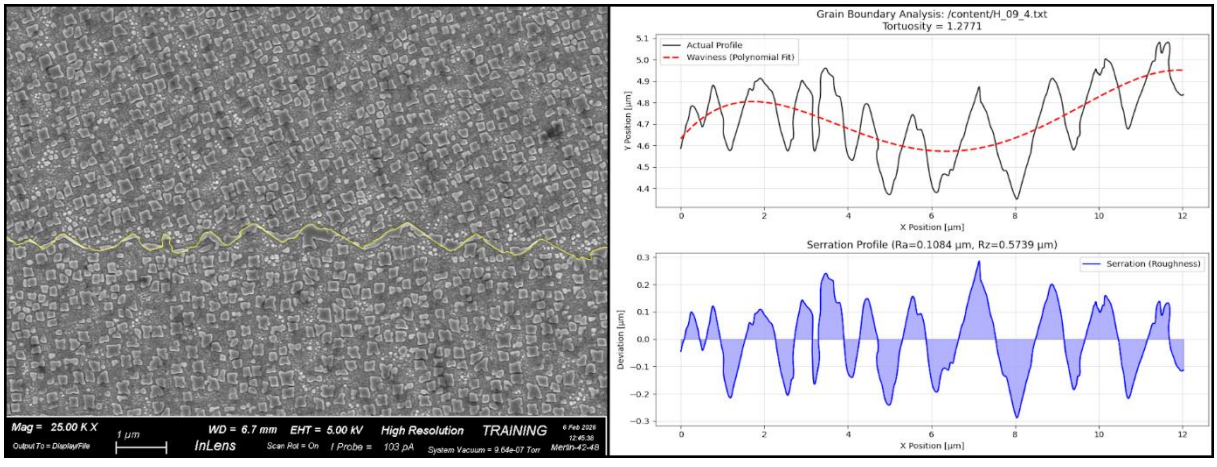

Figure 3.50: Grain boundary roughness evaluation method applied at one grain boundary of HIP-Quenched sample at 1220°C- 100MPa-120C°/min.

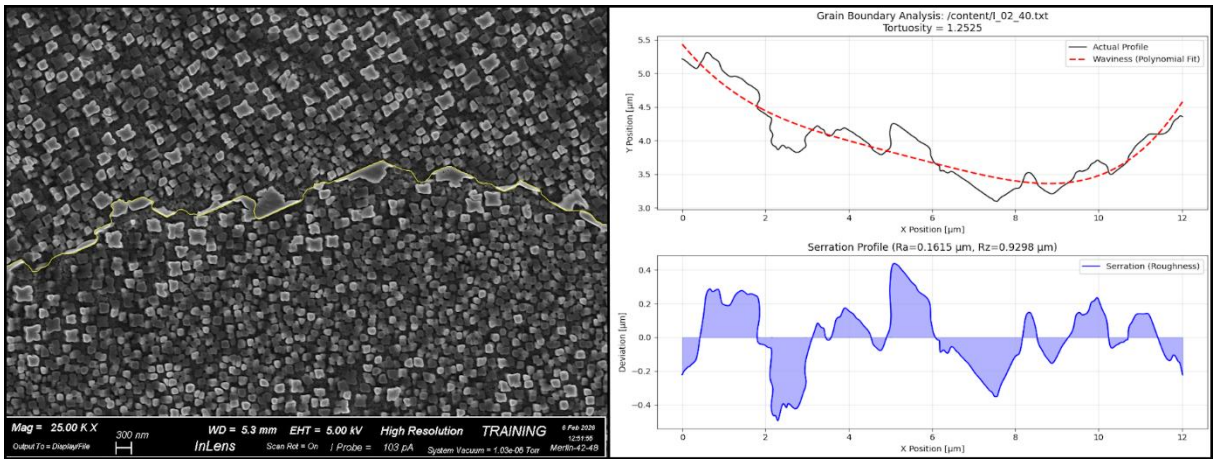

Figure 3.51: Grain boundary roughness evaluation method applied at one grain boundary of HIP-Quenched sample at 1240°C- 100MPa-120C°/min.

Figure 3.52 shows a comparison of samples processed at 100 MPa across cooling rates of 20°C/min and 120°C/min, highlighting the progressive reduction in grain boundary geometric complexity with increasing cooling rate. The mean roughness R_a decreased by an average of 30-38% across all investigated temperature conditions, while the maximum profile height R_z, a critical parameter for mechanical interlocking, dropped from a mean value of ~1.55 µm at 20°C/min to ~0.95 µm at 120°C/min. Similarly, tortuosity τ exhibited a consistent decline across all conditions, indicating that grain boundaries tend to straighten and become more planar as the cooling rate increases. A notable narrowing of the box plot distributions is also observed compared to those obtained at slower cooling rates, reflecting a more homogeneous grain boundary morphology throughout the material. These findings are consistent with the kinetic theory of grain boundary serration formation in Ni-based superalloys. Increasing the cooling rate promotes a higher γ′ nucleation density while simultaneously reducing precipitate size. At low cooling rates, precipitates have sufficient time to grow by diffusion, exerting a local pinning force on the migrating grain boundary and forcing it to curve around the particles, thus generating the characteristic serrated morphology. At higher cooling rates, the time available for diffusion is significantly reduced, with the results of finer boundary precipitates that are unable to exert sufficient force to deflect the grain boundary, which consequently retains a more planar configuration. Table 3.16 reports the output data of the grain boundary roughness evaluation.

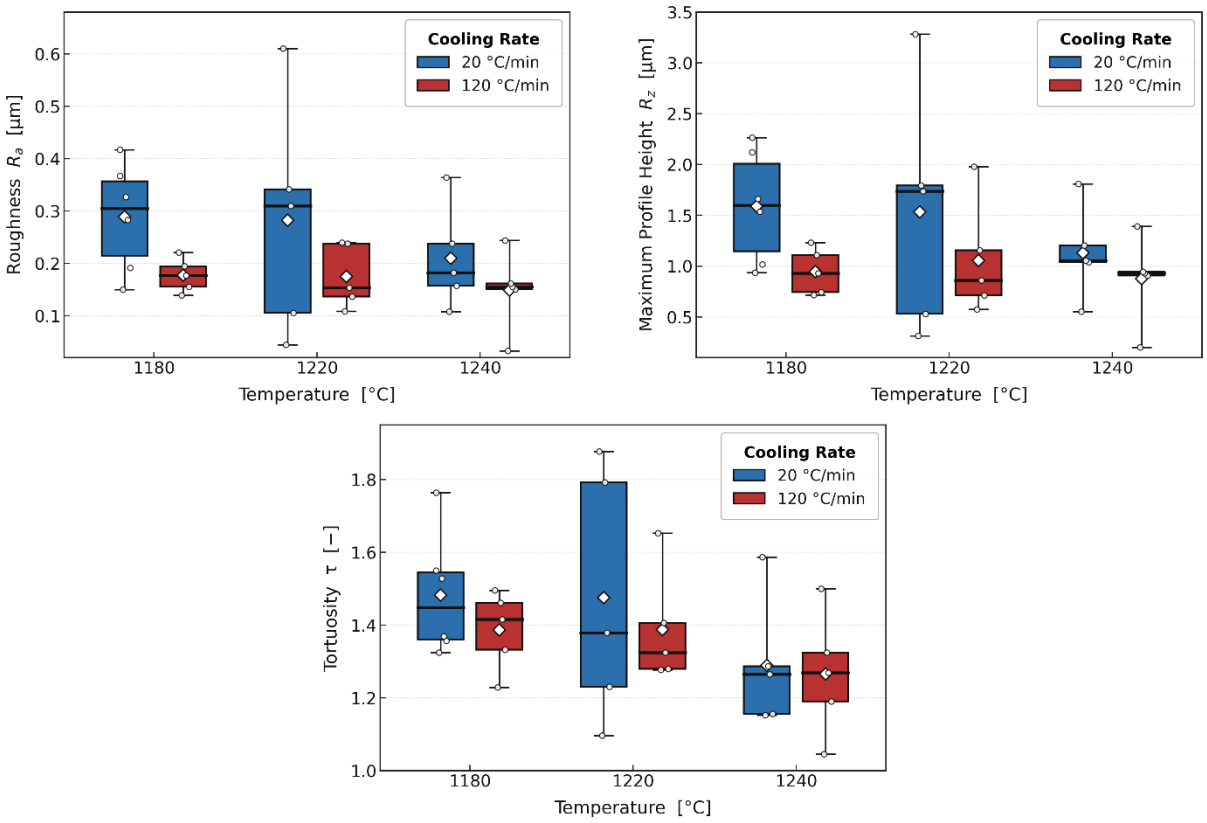

Figure 3.52: The image shows the box plots illustrating the trends of the three analyzed parameters average Roughness (R_a), maximum profile height (R_z) and Tortuosity (τ) as a function of the HIP solution temperature and cooling treatment (20°C/min vs 120 C°/min.

Table 3.16: Grain boundary roughness evaluation method parameters of HIP-Quenched samples at 100°C-120°C/min.

	Av. R_a [µm]	St. Dev [µm]	Av. R_z [µm]	St.Dev [µm]	Av. τ [-]	St. Dev [-]
sample G (1180°C)	0.177	0.032	0.94	0.22	1.346	0.13
sample H (1220°C)	0.175	0.060	1.05	0.55	1.30	0.06
sample I (1240°C)	0.148	0.075	0.87	0.42	1.23	0.10

However, this behavior is not universally observed. In many cases the data distributions show a considerable degree of overlap, leading to situations where some grain boundaries show a smoother profile while, in the same sample, a significant degree of serration was still present in localized regions, as shown in Figure 3.53.

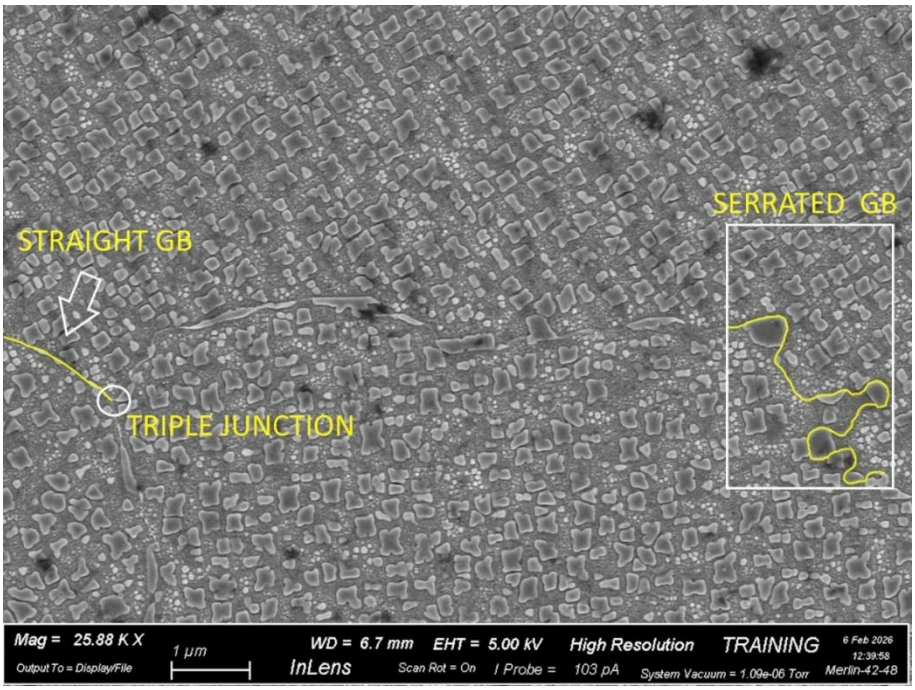

Figure 3.53: Grain boundaries showing the coexistence of smooth and serrated profiles within the same sample HIP-Quenched (1180 MPa-100MPA-120°C/min).

The data obtained from the grain boundary roughness evaluation method suggest that increasing the solution treatment temperature leads to a progressive reduction in the degree of boundary serration. To further rationalise this behaviour, grain boundary serration was treated as a thermally activated process and described within an Arrhenius law. Under this assumption, the serration amplitude quantified here through $\frac{1}{(R_a)\,(R_z)\,(\tau)}$ is expected to scale exponentially with the inverse of temperature, according to:

$$\frac{1}{(R_a)\,(R_z)\,(\tau)} \propto exp(-1/T) \tag{3.1}$$

Taking the logarithm of both sides of the above expression, all experimental data were plotted as shown in Figure 3.54. It should be noted that the data representation does not follow the conventional approach of first computing the arithmetic mean of the raw values and then applying the logarithm. Instead, the logarithm of each individual data point was calculated first, followed by the arithmetic mean of the resulting log-transformed values. This approach reduces the influence of outliers and more clearly reveals the underlying kinetic trend in the data.

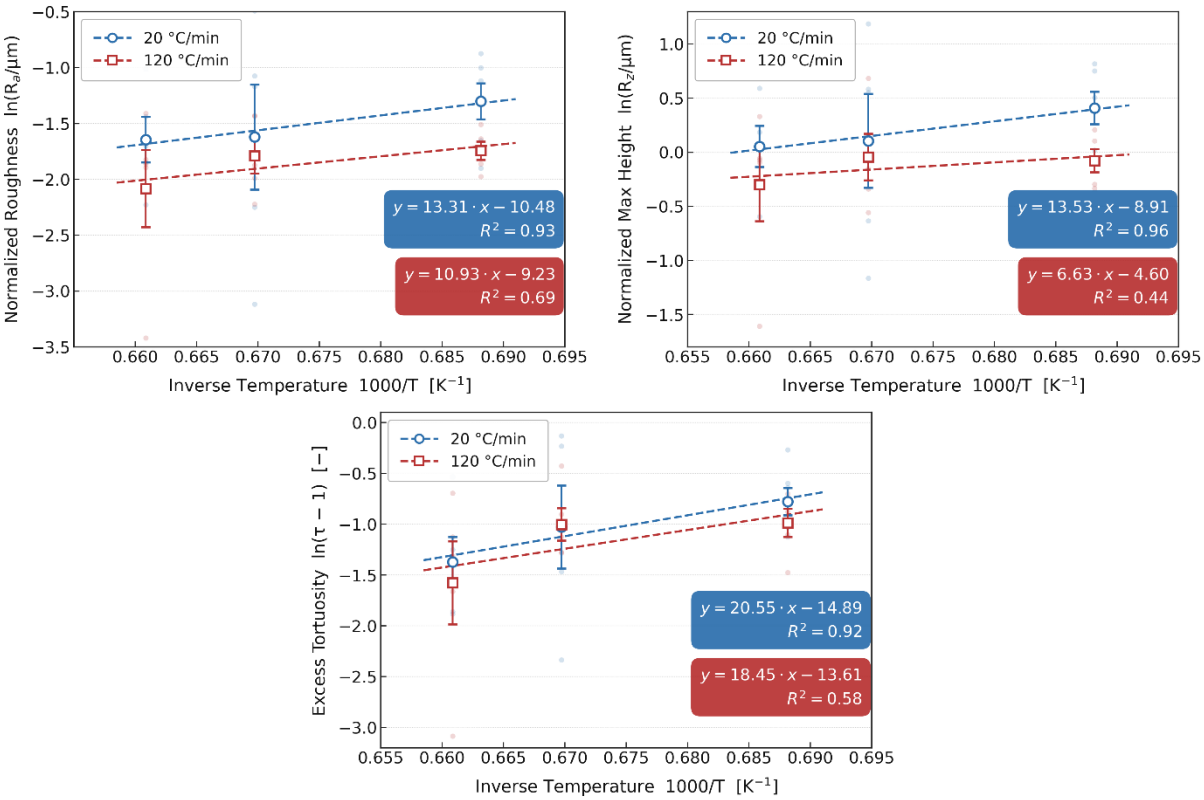

Figure 3.54: Arrhenius correlation of the grain boundary roughness evaluation method data comparison between HIP-ed vs HIP-Quenched samples.

The difference in the coefficient of determination (R^2) between the two cooling regimes clarifies the mechanism of grain boundary serration.

- 20 °C/min → R^2 (0.93, 0.96, 0.92)
- 120 °C/min → R^2 (0.69, 0.44, 0.58)

At 20°C/min, the strong linear correlation points to a diffusion-controlled regime, in which serration amplitude is predominantly governed by the thermodynamic driving force following Arrhenius kinetics. At 120°C/min, the drop in R^2 reflects a shift toward a kinetically-limited regime, where the rapid thermal excursion constrains atomic diffusion before the microstructure can evolve toward its thermodynamic equilibrium configuration. In Figure 3.54, tortuosity is expressed as τ-1 rather than τ, since a perfectly planar grain boundary carries a value of τ = 1 by definition. The quantity τ-1 therefore isolates the actual contribution of serration, representing the excess boundary path length generated by the tooth-like geometric features introduced during cooling.

The precipitation kinetics of γ′ inside the grain is clearly shown in Figure 3.55. Specifically, it shifted toward a strong nucleation rather than diffusion and growth of the γ′ phase compared with slow-cooling conditions. The presence of secondary γ′ is identified by finer precipitates displaying an intermediate morphology between rounded and cuboidal shapes, with the presence of fan-like structures, but more ordered and uniformly dispersed. The tertiary γ′ is also extremely fine and, in many cases, it is not possible to detect it even at high magnifications.

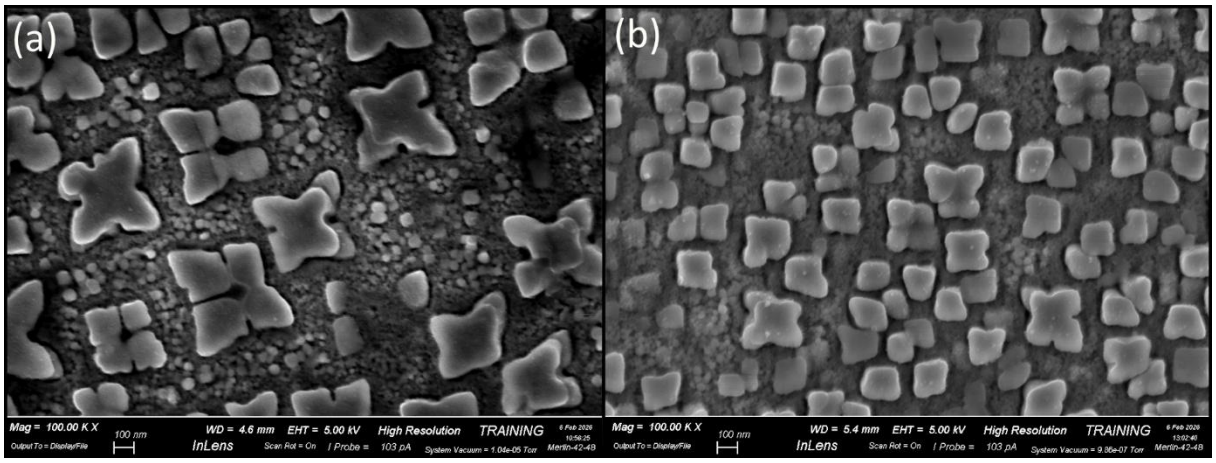

Figure 3.55: comparison micrographs of HIP-treated SAM specimens at different cooling rate: (a) 1240°C-20C°/min, (b) 1240°C -120°C/min.

Since the majority of precipitates exhibit a morphology close to cubic geometry, image analysis was carried out by extracting the equivalent side length as the primary output parameter. A closer examination of the precipitate size distribution in Figure 3.56 reveals a multimodal population, with a dominant peak at an equivalent side length of approximately 40 nm, followed by additional peaks of decreasing intensity in the 100-300 nm range. Compared to the population obtained at slower cooling rates, the larger precipitates are shifted toward smaller equivalent diameters, with the 20°C/min condition yielding distributions extending to equivalent side lengths exceeding 400 nm. Regarding the γ′ phase fraction, it remains centred around 40% on average, consistent with what was observed under slow cooling conditions. This indicates that, although the increased cooling rate favours nucleation at the expense of diffusion-driven growth, the system is both kinetically and thermodynamically driven toward the same equilibrium volume fraction of γ′ phase.

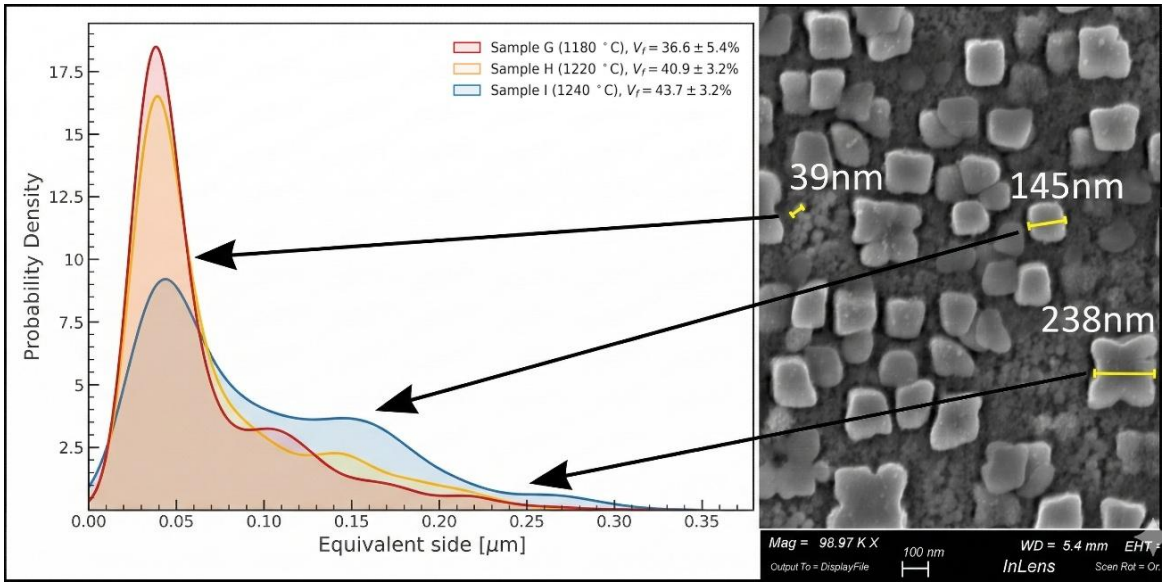

Figure 3.56: Probability density distribution of the equivalent diameters (μm) for HIP-Quenched samples at 100MPa and their volume fractions (V_f) are indicated.

The formation of a finer microstructure resulting from the rapid cooling imposed by the HIP-Quench cycle has a direct and measurable impact on hardness. In the HIP-Quench condition, the high cooling rate promotes extensive γ′ nucleation. This microstructure presents a significantly higher obstacle density to dislocation motion, translating into superior hardness values, as clearly shown in Figure 3.57 and Table 3.17 for the HIP-Q 100 MPa samples. The strengthening contribution arises from both Orowan bypass and precipitate shearing mechanisms, both of which are more effective when precipitates are small and densely distributed. Conversely, under slow cooling conditions, the reduced nucleation rate and extended diffusion time favour precipitate coarsening, increasing the inter-precipitate spacing and reducing the effectiveness of the strengthening mechanism, ultimately resulting in lower hardness values.

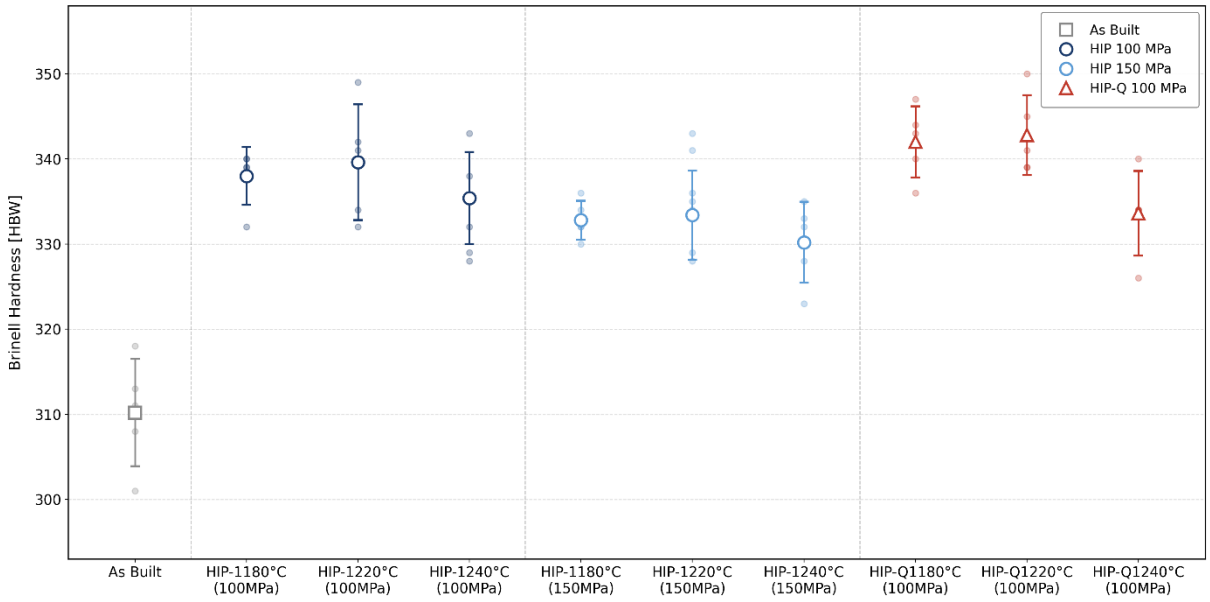

Figure 3.57: Brinell hardness (HBW) distribution across different sample conditions. The chart compares the baseline As-Built state with various Hot Isostatic Pressing (HIP) treatments grouped by pressure (100 MPa, 150 MPa) and a quenched condition (HIP-Q at 120°C/min).

Table 3.17: Average and standard deviation values of hardness (HBW) for different SAM samples HIP-Quenched at 100MPa-120°C/min.

	Av. Brinell H. [HBW]	St. Dev [HBW]
sample G (1180°C)	339.20	4.38
sample H (1220°C)	337.00	5.70
sample I (1240°C)	326.80	4.60

3.4. Formation mechanism of SGBs

Through the analysis of the grain boundary trajectory, several mechanisms responsible for the formation of SGBs can be identified. During slow cooling, primary γ′ preferentially nucleates at grain boundaries, which provide a lower energy barrier for heterogeneous nucleation due to their higher local free energy and enhanced atomic mobility. This promotes the formation of coarser precipitates along such regions. Subsequent growth is governed by the solute diffusion kinetics, which operate through two concurrent pathways: a slower bulk diffusion from the supersaturated matrix and a faster one along the incoherent grain boundary interface. Since the solute flux toward the incoherent grain boundary interface exceeds that toward the coherent matrix regions, the growth rate of γ′ precipitates is significantly enhanced in the direction normal to the grain boundary plane. This asymmetry in solute transport drives the preferential development of γ′ perpendicular to the boundary, ultimately forcing the grain boundary to curve around the growing precipitates and generating the characteristic serrated morphology.[36]
A defining characteristic of this growth mechanism is that γ′ precipitates, developing perpendicularly to the grain boundary, are consistently located on the concave side of the serrated grain boundary, with a size equal to or greater than the serration amplitude, as shown in Figure 3.58.

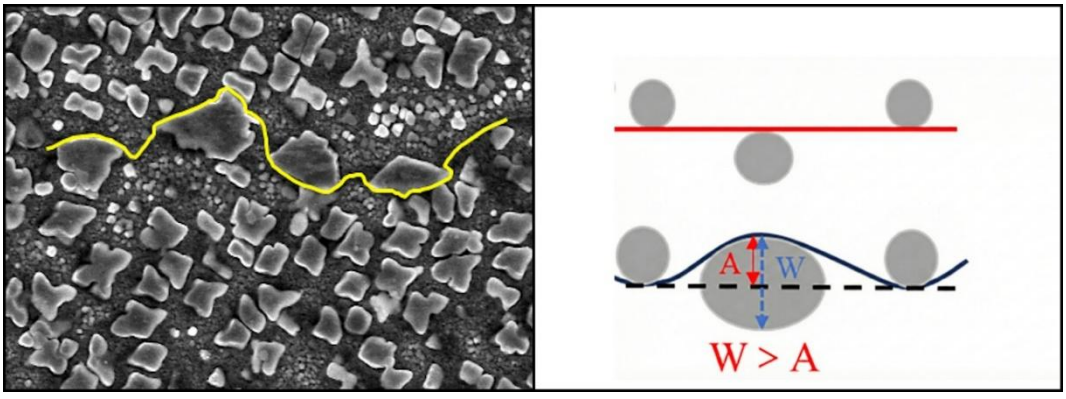

Figure 3.58: FESEM micrograph of a serrated grain boundary (highlighted in yellow) with primary γ′ precipitates located on its concave side, and corresponding schematic defining serration amplitude (A) and wavelength (W).[37]

In several cases, as illustrated in Figure 3.59, the serration amplitude exceeds the size of the γ′ precipitates located at the grain boundary, indicating that precipitate growth alone cannot fully account for the development of the serrated morphology. This observation points to the involvement of additional mechanisms. Koul and Gessinger proposed a complementary model based on the migration of γ′ precipitates along the grain boundary plane, driven by the elastic strain energy imbalance arising from the difference between the coherent γ′/γ matrix interface and the incoherent γ′/grain boundary interface. This thermodynamic driving force induces a localised dragging effect on the surrounding boundary, causing progressive deviations from a planar configuration. A distinctive feature of this mechanism is that γ′ precipitates are typically found at the apex of the concave boundary segments, with dimensions significantly smaller than the overall serration amplitude.[38]

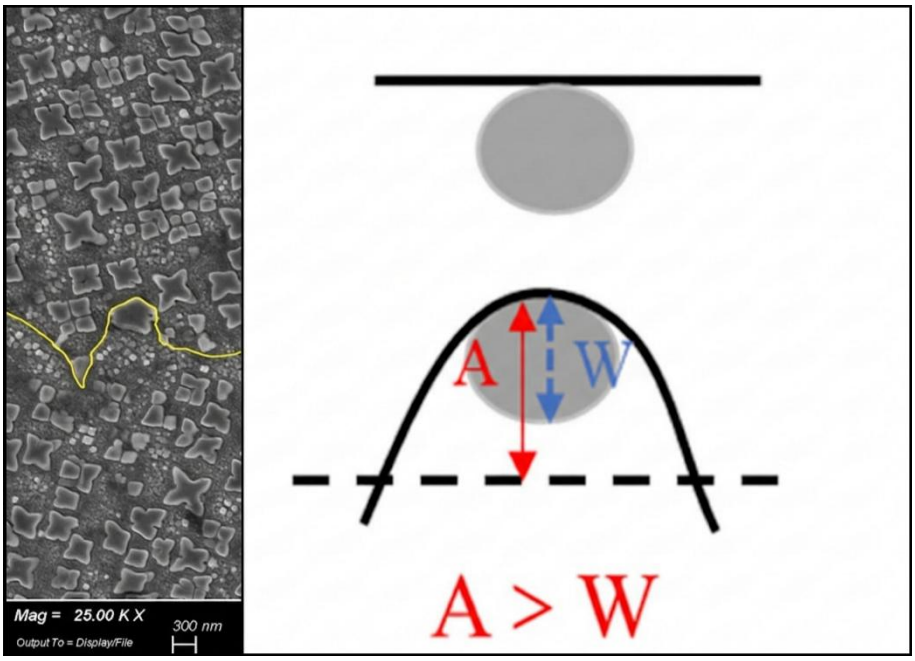

Figure 3.59: FESEM micrograph and schematic illustration of the migration mechanism, where the serration amplitude (A) exceeds the precipitate size (W).[37]

Alternatively, when they nucleate in large numbers and in close proximity, these precipitates may coalesce into a plate-like configuration, equally promoting a more planar grain boundary morphology, as shown in Figure 3.60. The stress field plays a crucial role in this coarsening process: the lattice misfit between γ′ and the γ matrix generates an anisotropic elastic strain field at the interface, which drives preferential precipitate growth along specific crystallographic directions to minimise the total strain energy. As the precipitates grow, their surrounding diffusion fields begin to overlap, causing a transition from independent to coalescent growth, ultimately leading to the formation of larger, elongated morphologies.[37]

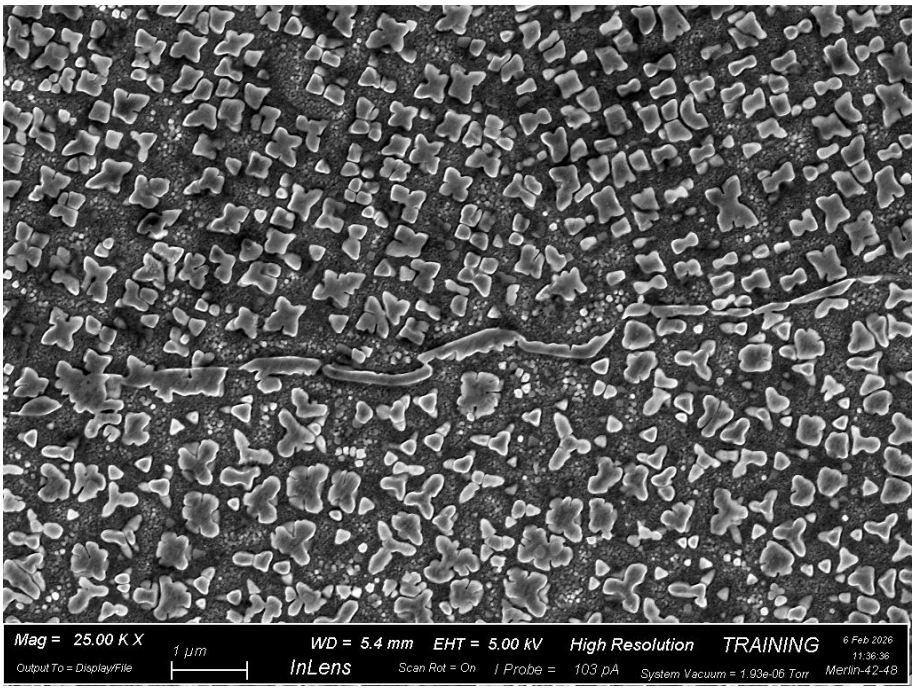

Figure 3.60: Grain boundary with high coalescence of γ′ along one direction.

In some cases, as shown in Figure 3.61, no primary γ′ precipitates are observed on the concave side of the serrated grain boundaries. This behaviour can be attributed to the Zener drag exerted by coarse γ′ precipitates, which locally pins the boundary and prevents its migration, while the surrounding unpinned boundary segments remain free to move and ultimately give rise to the characteristic serrated morphology.

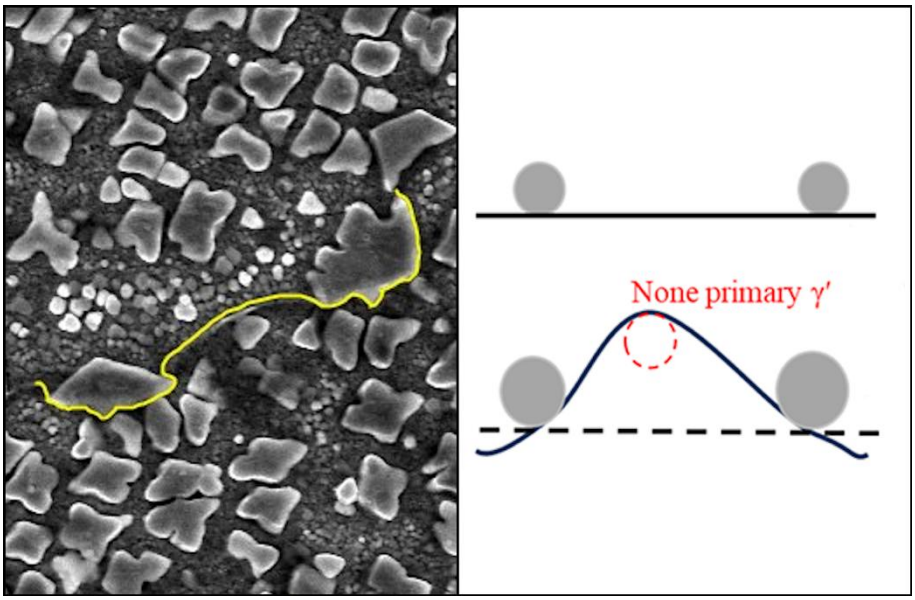

Figure 3.61: FESEM micrograph and schematic illustration of the migration mechanism, where γ′ precipitates locally arrest boundary migration while the surrounding unpinned segments remain free to move.[37]

At high cooling rates, γ′ exhibits a higher nucleation rate but limited growth, resulting in a predominantly fine cubic or granular morphology. Despite their small individual size, multiple γ′ precipitates distributed along the grain boundary can collectively pin the boundary through a synergistic mechanism, since a single particle alone would be insufficient to effectively impede boundary migration. Figure 3.62 shows his cooperative pinning effect nonetheless contributes to the development of a serrated grain boundary morphology.

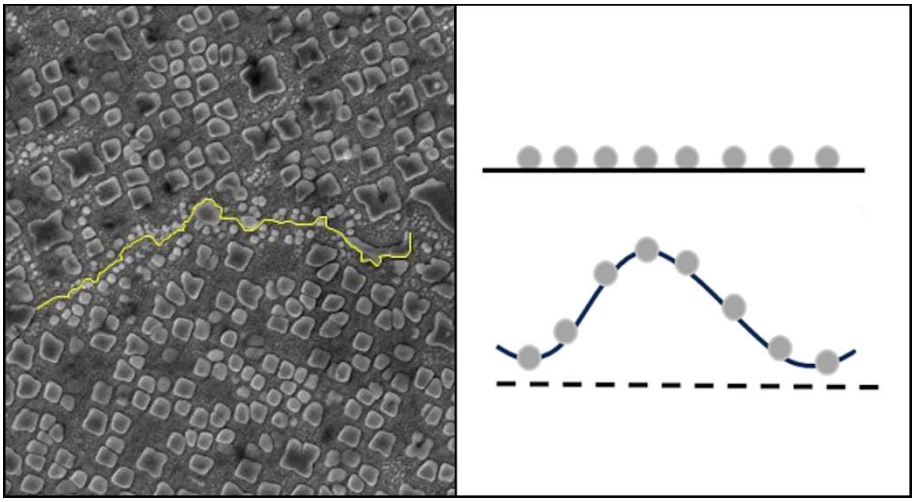

Figure 3.62: FESEM micrograph and schematic illustration of the migration mechanism, where fine γ′ precipitates are distributed along the grain boundary that collectively arrest boundary migration.[37]

3.5. Completion of the heat treatment

Aging represents the final heat treatment step aimed at achieving a refined and well-controlled morphology and distribution of γ′ precipitates, as well as at enhancing the overall microstructural homogeneity. Specifically, this thermal treatment is designed to regulate the precipitation kinetics and the subsequent growth of the γ′ phase, allowing the precipitates to progressively evolve toward a stable cuboidal morphology and a uniform spatial distribution within the matrix. These microstructural features are essential for the maximisation of the strengthening contribution of the γ′ phase, as they effectively hinder dislocation motion, while simultaneously ensuring improved thermal stability of the alloy under prolonged high-temperature service conditions. The strategy adopted for this treatment is illustrated in Figure 3.63. The strategy adopted for this treatment involves the evaluation of two different approaches applied to the HIP-Q sample at 1220°C. This procedure represents the best compromise in terms of microstructure and cost. The first approach consists of subjecting the HIP-Quenched sample to two lower aging temperatures, namely 600 °C and 800 °C, with the aim of promoting the precipitation of γ′, in particular the tertiary one. This method aims to populate the inter-channel regions between the secondary γ′ precipitates, thereby increasing the resistance to dislocation motion and enhancing the overall strengthening effect. The second approach, instead, aims to promote the precipitation and the homogenisation of γ′ and the carbides, through the application of two higher aging temperatures, namely 975 °C and 1000 °C.

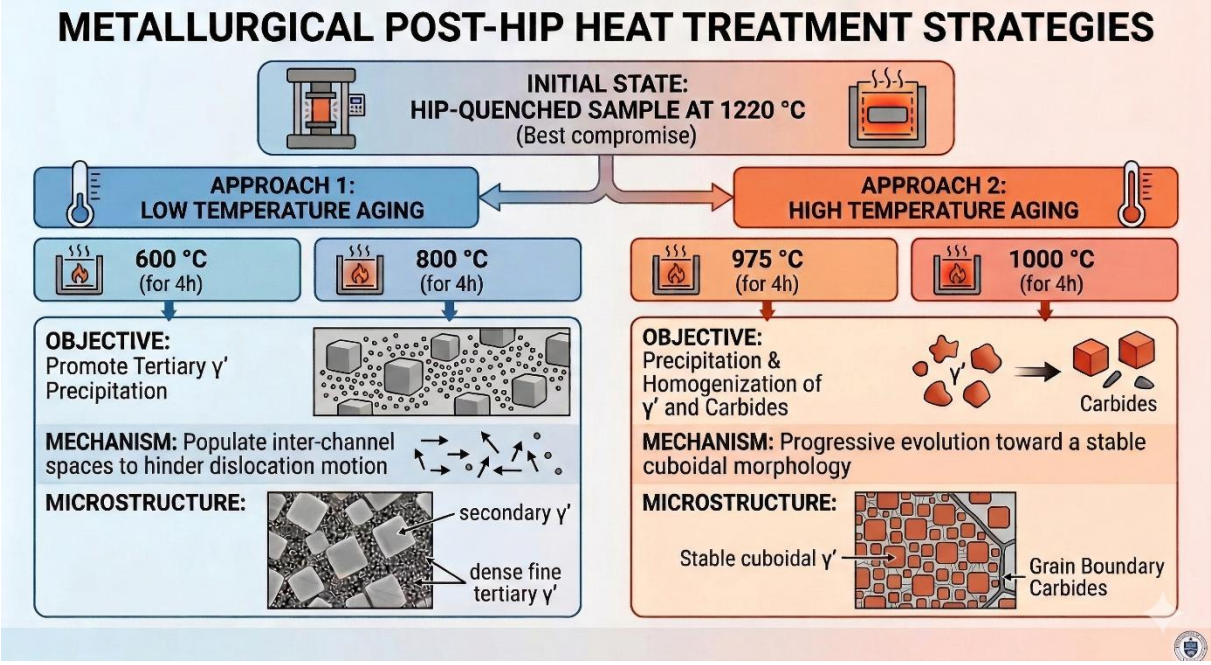

Figure 3.63: Aging workflow of the 1220°C HIP-Q sample.

During the first two ageing treatments, at 600°C and 800°C respectively, it is clear from Figure 3.64 that in both cases an orderly, cubic morphological evolution was not achieved. The fan-like structure persists in both cases. At first glance, areas with different gradients can be seen, in which secondary γ′ appears in the form of precipitates of varying sizes.

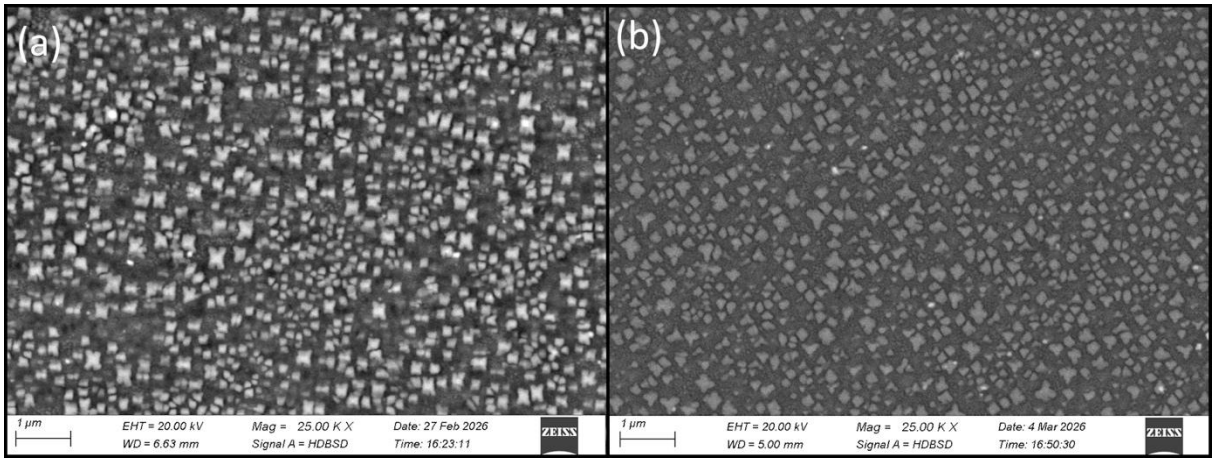

Figure 3.64: γ′ microstructure after aging:(a) after 4h aging at 600°C, (b) after 4h aging at 800°C.

The dimensional population analysis was carried out considering only secondary γ′ precipitates, as the acquired SEM images were resolution-limited to the detection of extremely fine tertiary γ′ particles. The probability density curves shown in Figure 3.65 are narrow and localised at equivalent side length values of approximately 140 nm, progressively broadening and shifting toward higher values exceeding 250 nm. The higher ageing temperature led to a

slight increase in the average equivalent side due to a greater contribution of diffusive phenomena, going from 147 to 154 µm.

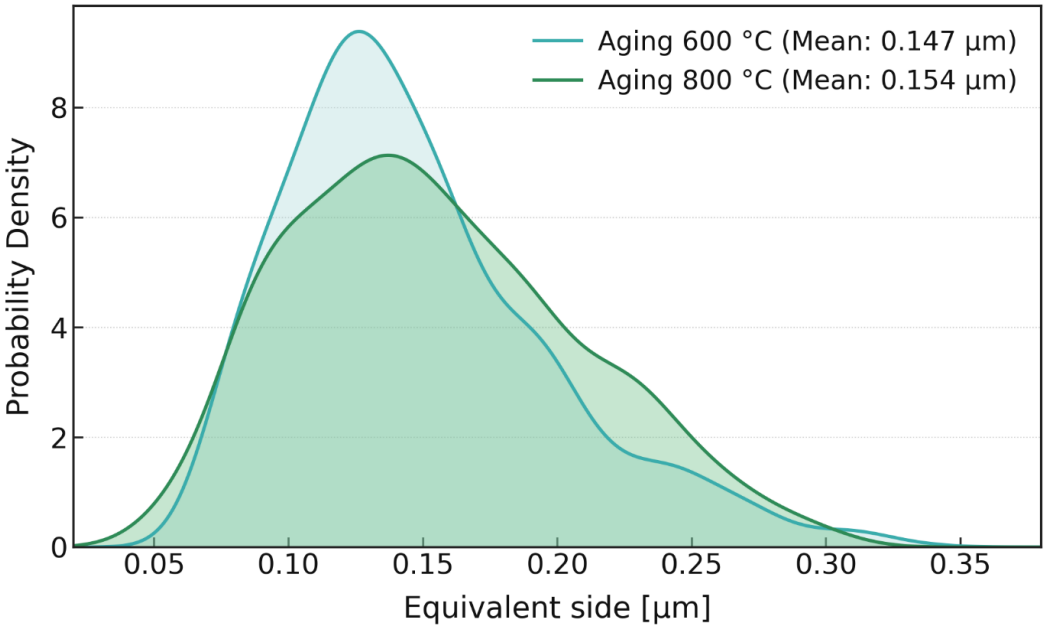

Figure 3.65: Plot of relative frequencies of precipitate size, expressed in terms of equivalent side, for the samples subjected to aging heat treatments at 600 °C and 800 °C.

In terms of γ′ volume fraction, a decrease from 34.2% to 29.7% is observed with increasing ageing temperature. However, this result should be interpreted with caution, as it does not account for the full precipitate population. At higher magnification, as shown in Figure 3.66 (b), it becomes evident that ageing at 800°C promotes significantly more extensive precipitation of fine tertiary γ′, which falls below the resolution limit of the analysis and is therefore, is not captured in the volume fraction measurements.

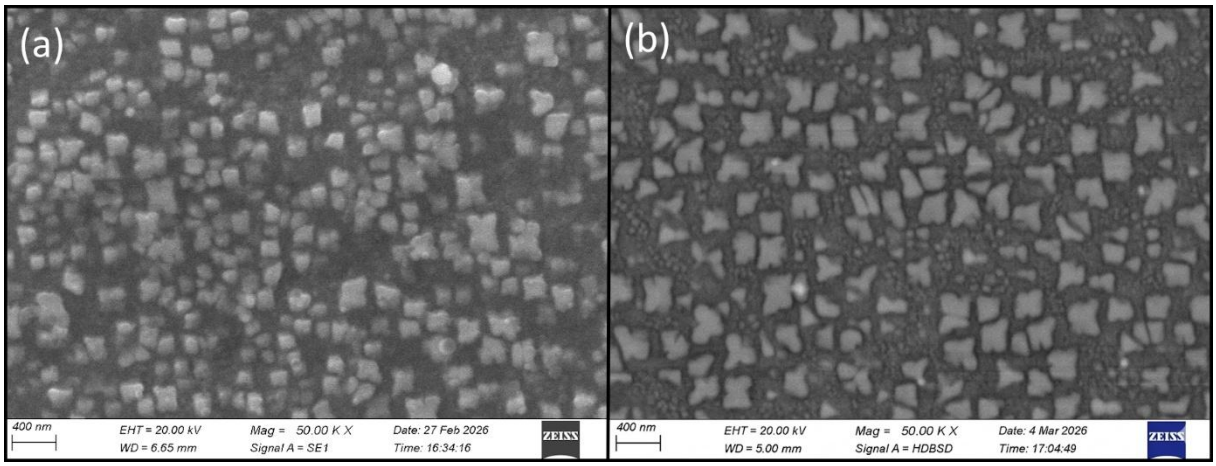

Figure 3.66: γ′ microstructure after aging:(a) after 4h aging at 600°C, (b) after 4h aging at 800°C.

At ageing temperatures of 975°C and 1000°C, a pronounced coarsening of the secondary γ′ precipitates is observed, accompanied by the disappearance of the fan-like morphology and the evolution toward a well-ordered, predominantly cubic structure, as shown in Figure 3.67. Furthermore, no tertiary γ′ is detectable within the γ channels, indicating that diffusion-driven

Ostwald ripening promoted the coalescence of finer precipitates, favouring the growth of secondary γ′ at the expense of the finely precipitated population.

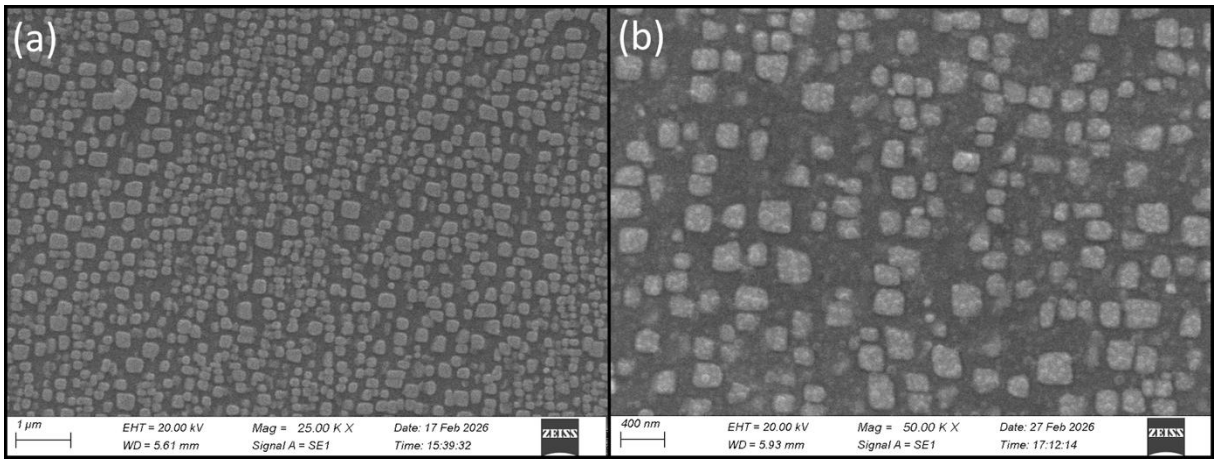

Figure 3.67: γ′ microstructure after aging:(a) after 4h aging at 975°C, (b) after 4h aging at 1000°C.

Also in this case, the precipitate size population analysis was carried out considering only secondary γ′ precipitates, due to the instrumental resolution limitation of the acquired images. The probability density curves, shown in Figure 3.68, are narrow, but localised at equivalent side length values larger than those observed at lower ageing temperatures, with the primary peak shifting to approximately 200 nm at 1000°C. The larger secondary γ′ precipitate size, obtained at elevated ageing temperatures, is further confirmed by the mean equivalent side lengths of 161 nm and 174 nm recorded at 975°C and 1000°C, respectively. These values are consistent with the progressive coarsening driven by enhanced diffusivity at higher temperatures.

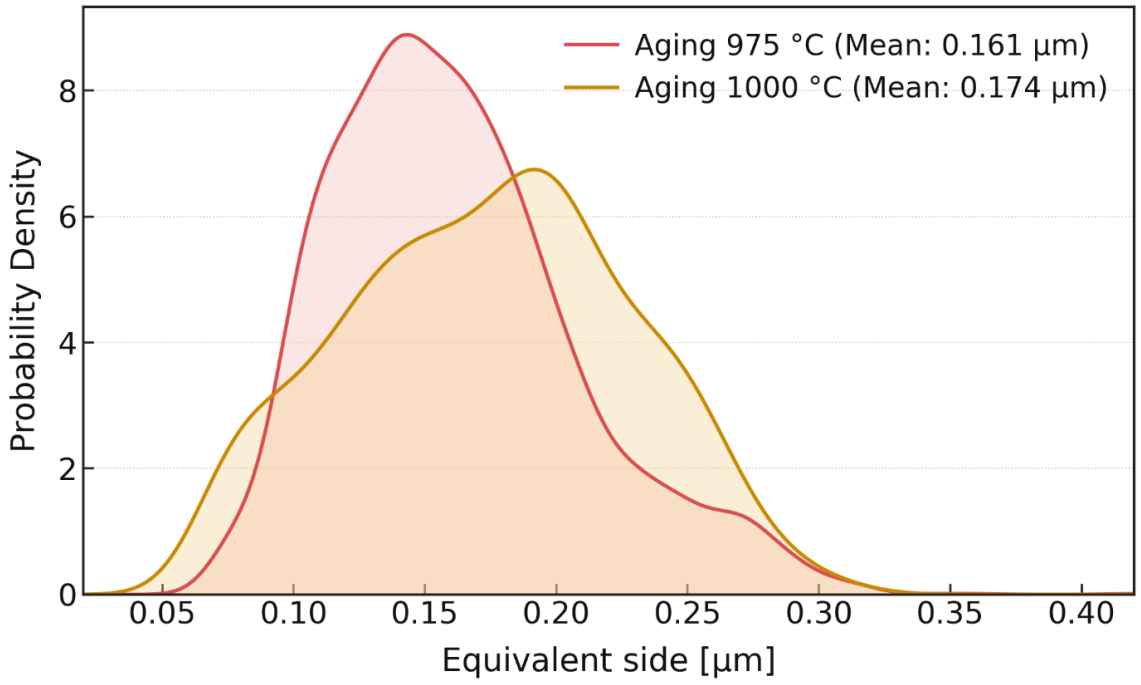

Figure 3.68: Plot of relative frequencies of precipitate size, expressed in terms of equivalent side, for the samples subjected to aging heat treatments at 975 °C and 1000 °C.

The microstructural changes described above are also reflected at the grain boundaries. Figure 3.69 shows representative grain boundary regions after ageing at 800°C and 1000°C, respectively. At 1000°C, the rapid diffusion of γ′-forming elements toward these high-energy sites promotes the growth of larger and more regularly shaped boundary precipitates. This localized solute drainage depletes the adjacent matrix of γ′-forming elements, leading to the dissolution of particles in the immediate vicinity of the grain boundary and giving rise to the characteristic solute-depleted region known in the literature as the Precipitate-Free Zone (PFZ). These zones act as preferential pathways for dislocation motion, lowering the stress required to initiate plastic deformation and thereby adversely affecting the yield strength of the material. [39]

At 800°C, atomic mobility is comparatively lower, and the primary γ′ precipitates at the boundary retain a more irregular morphology. However, the supersaturated state of the surrounding matrix simultaneously favours the nucleation of very fine tertiary γ′ precipitates in the region immediately adjacent to the grain boundary.

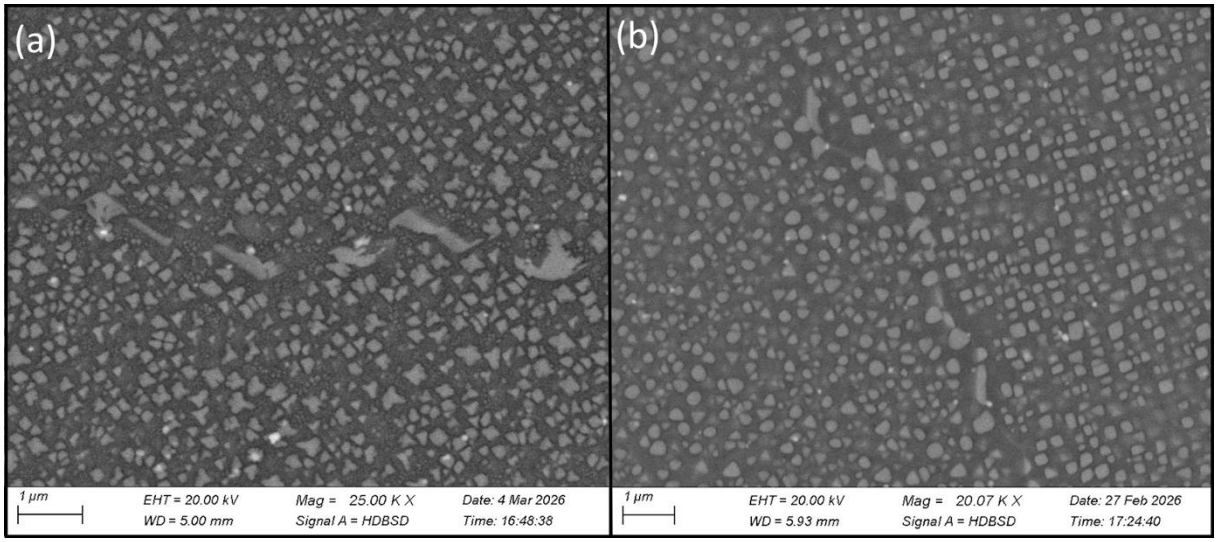

Figure 3.69: SEM micrographs showing grain boundary morphology after aging at two different temperatures: (a) 800 °C and (b) 1000 °C.

Figure 3.70 shows the results of the Brinell hardness measurements carried out on the four samples subjected to ageing treatments at different temperatures. The microstructural analysis presented in the preceding sections provides the interpretation of distinct mechanical responses observed across the investigated conditions.

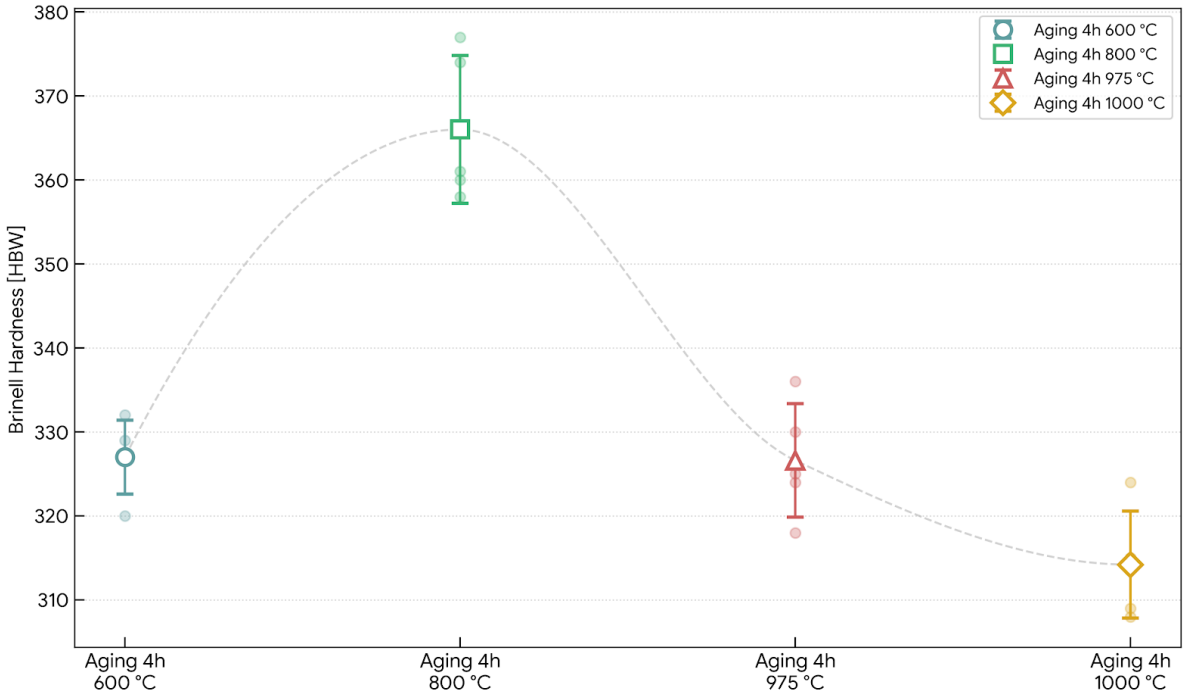

Figure 3.70: Brinell hardness values measured on samples subjected to aging treatments at different temperatures.

Table 3.18*:* Average and standard deviation values of hardness (HBW) for different aging treatments.

	Av. Brinell H. [HBW]	St. Dev [HBW]
Aging 600C°	327.00	4.42
Aging 800C°	366.00	8.80
Aging 975C°	326.60	6.77
Aging 1000C°	314.20	6.38

- At 600°C, under sub-ageing conditions, a secondary γ′ volume fraction of approximately 31.2% and a hardness of 327 HBW are recorded. These values indicate that at this temperature the precipitation kinetics are insufficiently rapid to develop a fully effective strengthening precipitation distribution within the applied soaking time.

- By raising the ageing temperature to 800°C, the maximum hardness peak of 366 HBW is reached. At this condition, the secondary γ′ volume fraction determined by image analysis drops to 26.7%, a result that may appear counterintuitive but in fact constitutes indirect evidence of extensive tertiary γ′ precipitation within the γ matrix channels. At 800°C, a significant fraction of the γ′-forming elements, including Al, Ti, and Nb, is redistributed from the secondary precipitates to nucleate a high density of ultrafine, nanometric tertiary precipitates. This tertiary population falls below the instrumental

resolution limit and therefore, is not captured by image analysis. Yet it is primarily responsible for the hardness peak. Its presence drastically reduces the mean free path available for dislocation glide, maximising the resistance to plastic deformation through the classical strengthening mechanisms of precipitate shearing and Orowan bowing.

- At 975°C and 1000°C, a pronounced microstructural evolution is observed. The probability density curves broaden considerably and shift toward progressively larger equivalent side length values, a behaviour symptomatic of Ostwald ripening, whereby the high thermal energy drives the dissolution of finer precipitates, including tertiary γ′. These finer precipitates disappear entirely in favour of the thermodynamically driven growth of coarser particles. The measured volume fraction data clearly corroborate this mechanism: at 975°C, a sharp increase in the visible γ′ fraction to 37.8% is recorded. It is attributable to the complete dissolution and coalescence of the fine tertiary precipitates into the growing secondary population, thereby maximising the measurable area fraction. However, the concurrent increase in secondary γ′ size and inter-particle spacing progressively reduces the effectiveness of dislocation blocking, driving the material into an over-aged condition and accounting for the hardness drop to 326 HBW. For the same reason, the rise in the process temperature to 1000°C results in an increase in the γ′ phase and γ channels, leading to a decrease in volume percentage and hardness, respectively, 32% and 314HBW.

4. Conclusion

This thesis has demonstrated the effectiveness of an innovative integrated thermal process (HIP-Quenching) applied to a SAM nickel-based superalloy produced by LPBF. This approach represents a viable alternative to conventional multi-step heat treatments, reducing both processing time and costs by combining defect healing and solution treatment into a single stage. The main conclusions from the experimental investigation are summarised below:

- **Densification and Recrystallisation:** HIP showed high effectiveness in closing printing-induced defects. The equivalent pore diameter distribution curves follow a log-normal trend. Successively, the increase in both process temperature and pressure shifts these equivalent diameter curves toward smaller dimensional values while simultaneously reducing the total pore count. Densification levels exceeding 99.96% were consistently achieved. A pressure of 100 MPa was found to be fully sufficient; its increase to 150 MPa led to a reduction in residual porosity of only 0.01-0.02%, which does not justify the associated growth in operating costs. Temperature emerged as the primary control variable: not only did treatments at 1240°C refine the pore size distribution, but they also provided the thermal energy necessary to trigger extensive static recrystallisation, fragmenting the columnar grain structure inherited from the directional solidification conditions of the additive process, mitigating microstructural anisotropy, and reducing aspect ratio values.

- **Effect of Cooling Rate:** The HIP-Quench process confirmed that the cooling rate has no appreciable influence on either final density or grain size, since both porosity closure and recrystallisation are completed during the supersolvus holding stage. The cooling rate instead governs the nucleation and growth kinetics of the γ' phase. Slow cooling at 20°C/min allows precipitates to grow to larger sizes, producing a multimodal size distribution with equivalent diameters exceeding 450 nm. Rapid cooling at 120°C/min promotes significantly finer precipitation, with maximum equivalent diameters below 300 nm. This finer and more homogeneously dispersed γ' microstructure translates into higher hardness values, reaching mean values of up to 342 HBW. In both cooling regimes, the γ' morphology remains irregular, with the characteristic fan-like structures retained.

- **Grain Boundary Roughness Evaluation Method:** By investigating the variation in R_a, R_z, and τ as a function of processing parameters, the relationship between the degree of grain boundary serration and the solution treatment temperature and cooling rate was clarified. The study revealed that grain boundary morphology and γ' precipitation is governed by the thermodynamic-kinetic balance established during cooling. A first comparison between the two experimental sets processed at 100 MPa and 150 MPa under slow cooling conditions led to fully superimposable results, confirming that pressure is not a determining factor in the serration process. A mild decreasing trend in the serration characterisation parameters was observed with increasing solution treatment temperature. Regarding the effect of cooling rate, slow cooling at 20°C/min establishes a diffusion-controlled regime that allows γ' precipitates to grow and forces grain boundaries into a strongly serrated morphology. Conversely, rapid cooling at 120°C/min confines the system to a kinetically limited regime, in which the serration mechanism is effectively suppressed. Future work should focus on further automating

the Grain Boundary Roughness Evaluation Method, enabling the simultaneous analysis of a larger number of grain boundaries and improving the statistical robustness of the characterisation.

- **Ageing:** The HIP-Q sample processed at 1220°C was subjected to four distinct ageing temperatures. At 800°C, the maximum hardness of ~366 HBW was recorded, driven by the extensive precipitation of nanometric tertiary γ′ within the matrix channels, which maximises the obstacle density to dislocation motion. Exposure to higher temperatures (975°C and 1000°C) triggers Ostwald ripening, whereby precipitate coalescence leads to uncontrolled coarsening of the secondary γ′ population, wider γ matrix channels, and the appearance of Precipitate-Free Zones (PFZ) near the grain boundaries. This over-aged condition results in a marked deterioration of mechanical performance, with mean hardness values dropping to ~326 HBW and ~314 HBW, respectively. It should be noted that the secondary γ′ morphology obtained after ageing at 800°C remains considerably irregular. Future work aimed at assessing the margins for further improvement should therefore focus on exploring the temperature window between 800°C and 900°C and on investigating the effect of different soaking times, with the objective of promoting a more regular cuboidal γ′ morphology with narrower and more uniform matrix channels, to maximise thermomechanical performance.

Acknowledgements

Prima di arrivare a questo punto non avevo mai pensato alle parole da scrivere, forse perché finché non si arriva a tagliare il traguardo non lo si realizza veramente. Guardandomi indietro, è stato un viaggio lungo e stimolante, ricco di sfide e momenti altalenanti. Di una cosa sono sicuro, senza la mia famiglia questo viaggio non sarebbe stato possibile, in particolare mia madre, mio padre e alla mia Stella. Un ringraziamento speciale va a chi non c'è più, che mi ha insegnato che se vuoi puoi e mi guarda da qualche barca da lassù. Un ringraziamento sincero va alla mia famiglia allargata di amici che sono stati il compagno di viaggio perfetto ed indispensabile, sempre presente nei momenti del bisogno e non. Infine, ringrazio la curiosità, quella che per fortuna non mi ha abbandonato nel percorso e mi auguro non mi abbandoni nella vita. Quella che ti motiva a cercare spiegazioni anche dietro argomenti che gli automatismi della nostra mente pensano di aver già consolidato e permette di andare oltre evolvendo continuamente. Senza la quale forse, il mondo sarebbe alimentato da poco.

Bibliography

[1] *Manufacturing Technology for Aerospace Structural Materials*. Elsevier, 2006. doi: 10.1016/B978-1-85617-495-4.X5000-8.

[2] K. Minet, A. Saharan, A. Loesser, e N. Raitanen, «Superalloys, powders, process monitoring in additive manufacturing», in *Additive Manufacturing for the Aerospace Industry*, Elsevier, 2019, pp. 163–185. doi: 10.1016/B978-0-12-814062-8.00009-1.

[3] R. C. Reed, *The Superalloys: Fundamentals and Applications*. Cambridge University Press, 2008.

[4] A. C. LIMITED, «Clearly Understand the Role of Nickel in All 3 Types of Superalloys», aeether.com. Consultato: 4 dicembre 2025. [Online]. Disponibile su: https://www.aeether.com/AEETHER/media/media-4/media.html

[5] S. Qiu e Z. Jiao, «Ni-Base Superalloys: Alloying and Microstructural Control», in *Advanced Multicomponent Alloys*, Z. Jiao e T. Yang, A c. di, in Materials Horizons: From Nature to Nanomaterials. , Singapore: Springer Nature Singapore, 2022, pp. 133–154. doi: 10.1007/978-981-19-4743-8_6.

[6] Z. Li *et al.*, «Quantifying Solid Solution Strengthening in Nickel-Based Superalloys via High-Throughput Experiment and Machine Learning», *Comput. Model. Eng. Sci.*, vol. 135, fasc. 2, pp. 1521–1538, 2022, doi: 10.32604/cmes.2022.021639.

[7] R. Eriş, M. V. Akdeniz, e A. O. Mekhrabov, «Atomic size effect of alloying elements on the formation, evolution and strengthening of γ′-Ni3Al precipitates in Ni-based superalloys», *Intermetallics*, vol. 109, pp. 37–47, giu. 2019, doi: 10.1016/j.intermet.2019.02.017.

[8] G. Brunetti *et al.*, «Determination of γ-γ' lattice misfit in a single-crystal nickel-based superalloy using convergent beam electron diffraction aided by finite element calculations», *Micron Oxf. Engl. 1993*, vol. 43, pp. 396–406, ott. 2011, doi: 10.1016/j.micron.2011.10.009.

[9] K. Hou *et al.*, «Temperature-dependent yield strength and deformation mechanism of a casting Ni-based superalloy containing low volume-fraction γ′ phase», *J. Alloys Compd.*, vol. 905, p. 164187, giu. 2022, doi: 10.1016/j.jallcom.2022.164187.

[10] K. Hou *et al.*, «Temperature-dependent yield strength and deformation mechanism of a casting Ni-based superalloy containing low volume-fraction γ′ phase», *J. Alloys Compd.*, vol. 905, p. 164187, giu. 2022, doi: 10.1016/j.jallcom.2022.164187.

[11] S. Anand, A c. di, «Current trends in engineering practice: lectures under the AICTE-INAE Distinguished Visiting Professorship Scheme. Vol. 3», New Delhi: Narosa Publ. House, 2014.

[12] P. M. Mignanelli *et al.*, «Gamma-gamma prime-gamma double prime dual-superlattice superalloys», *Scr. Mater.*, vol. 136, pp. 136–140, lug. 2017, doi: 10.1016/j.scriptamat.2017.04.029.

[13] Y. Chen, H. Yu, Y. Chen, H. Di, e W. Xu, «The strengthening effects and mechanisms of alloying elements on interfaces for multiphase Ni-based superalloys: A first-principles study», *J. Mater. Res. Technol.*, vol. 23, pp. 4802–4813, mar. 2023, doi: 10.1016/j.jmrt.2023.02.119.

[14] W. Xia, X. Zhao, L. Yue, e Z. Zhang, «A review of composition evolution in Ni-based single crystal superalloys», *J. Mater. Sci. Technol.*, vol. 44, pp. 76–95, mag. 2020, doi: 10.1016/j.jmst.2020.01.026.

[15] M. Jullien, R. L. Black, J. C. Stinville, M. Legros, e D. Texier, «Grain size effect on strain localization, slip-grain boundary interaction and damage in the Alloy 718 Ni-based

superalloy at 650 °C», *Mater. Sci. Eng. A*, vol. 912, p. 146927, ott. 2024, doi: 10.1016/j.msea.2024.146927.
[16] M. Mudang, E. Hamzah, H. R. Bakhsheshi-Rad, e F. Berto, «Effect of Heat Treatment on Microstructure and Creep Behavior of Fe-40Ni-24Cr Alloy», *Appl. Sci.*, vol. 11, fasc. 17, ago. 2021, doi: 10.3390/app11177951.
[17] H. U. Hong, I. S. Kim, B. G. Choi, M. Y. Kim, e C. Y. Jo, «The effect of grain boundary serration on creep resistance in a wrought nickel-based superalloy», *Mater. Sci. Eng. A*, vol. 517, fasc. 1, pp. 125–131, ago. 2009, doi: 10.1016/j.msea.2009.03.071.
[18] Y. T. Tang, A. J. Wilkinson, e R. C. Reed, «Grain Boundary Serration in Nickel-Based Superalloy Inconel 600: Generation and Effects on Mechanical Behavior», *Metall. Mater. Trans. A*, vol. 49, fasc. 9, pp. 4324–4342, set. 2018, doi: 10.1007/s11661-018-4671-7.
[19] Q. Tian *et al.*, «Formation mechanism of serrated grain boundary caused by different morphologies of γ′ precipitates in GH4742 superalloy», *J. Mater. Res. Technol.*, vol. 35, pp. 4352–4367, mar. 2025, doi: 10.1016/j.jmrt.2025.02.107.
[20] Y. Zhang *et al.*, «The Characterization of Curved Grain Boundary in Nickel-Based Superalloy Formed During Heat Treatment», *Metals*, vol. 16, fasc. 1, gen. 2026, doi: 10.3390/met16010068.
[21] R. Reed, «Physcial Metallurgy and Microstructure of Superalloys».
[22] H. Wang *et al.*, «Modification of M23C6 carbides by Ti addition in Ni-based polycrystalline superalloy», *Scr. Mater.*, vol. 263, p. 116686, lug. 2025, doi: 10.1016/j.scriptamat.2025.116686.
[23] X. Li, M. Ou, M. Wang, L. Zhang, Y. Ma, e K. Liu, «Effect of boron addition on the microstructure and mechanical properties of K4750 nickel-based superalloy», *J. Mater. Sci. Technol.*, vol. 60, pp. 177–185, gen. 2021, doi: 10.1016/j.jmst.2020.02.079.
[24] B. Du *et al.*, «*M*5B3 Boride at the Grain Boundary of a Nickel-based Superalloy», *J. Mater. Sci. Technol.*, vol. 32, fasc. 3, pp. 265–270, mar. 2016, doi: 10.1016/j.jmst.2015.11.010.
[25] A. Mostafaei *et al.*, «Defects and anomalies in powder bed fusion metal additive manufacturing», *Curr. Opin. Solid State Mater. Sci.*, vol. 26, fasc. 2, p. 100974, apr. 2022, doi: 10.1016/j.cossms.2021.100974.
[26] M. Calandri, S. Yin, B. Aldwell, F. Calignano, R. Lupoi, e D. Ugues, «Texture and Microstructural Features at Different Length Scales in Inconel 718 Produced by Selective Laser Melting», *Materials*, vol. 12, fasc. 8, apr. 2019, doi: 10.3390/ma12081293.
[27] O. Adegoke, J. Andersson, H. Brodin, e R. Pederson, «Review of Laser Powder Bed Fusion of Gamma-Prime-Strengthened Nickel-Based Superalloys», *Metals*, vol. 10, fasc. 8, lug. 2020, doi: 10.3390/met10080996.
[28] F. Schulz, K. Lindgren, J. Xu, e E. Hryha, «Gamma prime formation in nickel-based superalloy IN738LC manufactured by laser powder bed fusion», *Mater. Today Commun.*, vol. 38, p. 107905, mar. 2024, doi: 10.1016/j.mtcomm.2023.107905.
[29] X. G. Zheng, Y.-N. Shi, e L. H. Lou, «Healing Process of Casting Pores in a Ni-based Superalloy by Hot Isostatic Pressing», *J. Mater. Sci. Technol.*, vol. 31, fasc. 11, pp. 1151–1157, nov. 2015, doi: 10.1016/j.jmst.2015.07.004.
[30] «Hot Isostatic Pressing: Improving quality and performance in AM», Metal Additive Manufacturing. Consultato: 14 marzo 2026. [Online]. Disponibile su: https://www.metal-am.com/articles/hot-isostatic-pressing-improving-quality-and-performance-in-3d-printing/
[31] A. Du Plessis e E. Macdonald, «Hot isostatic pressing in metal additive manufacturing: X-ray tomography reveals details of pore closure», *Addit. Manuf.*, vol. 34, p. 101191, ago. 2020, doi: 10.1016/j.addma.2020.101191.

[32] M. R. G. Prasad, S. Gao, N. Vajragupta, e A. Hartmaier, «Influence of Trapped Gas on Pore Healing under Hot Isostatic Pressing in Nickel-Base Superalloys», *Crystals*, vol. 10, fasc. 12, dic. 2020, doi: 10.3390/cryst10121147.
[33] P. A. Martelli, E. Bassini, e D. Ugues, «The effect of hot isostatic pressing pressure level and solution annealing cooling rate on CM247 LC nickel-based superalloy processed by laser-based powder bed fusion», *Prog. Addit. Manuf.*, vol. 10, fasc. 1, pp. 605–618, gen. 2025, doi: 10.1007/s40964-024-00645-6.
[34] E. Bassini *et al.*, «Effetto della pressatura isostatica a caldo (HIP) e del trattamento termico di leghe di Nichel fabbricate via Selective Laser Melting (SLM) = Effect of the Hot Isostatic Pressing (HIP) and heat treatment to nickel-based alloys obtained with Selective Laser Melting (SLM)», 2021, Consultato: 18 febbraio 2026. [Online]. Disponibile su: https://iris.polito.it/handle/11583/2955509
[35] Y. T. Tang, P. Karamched, J. Liu, J. C. Haley, R. C. Reed, e A. J. Wilkinson, «Grain boundary serration in nickel alloy inconel 600: Quantification and mechanisms», *Acta Mater.*, vol. 181, pp. 352–366, dic. 2019, doi: 10.1016/j.actamat.2019.09.037.
[36] M. F. Henry, Y. S. Yoo, D. Y. Yoon, e J. Choi, «The Dendritic Growth of γ′ Precipitates and Grain Boundary Serration in a Model Nickel-Base Superalloy», *Metall. Trans. A*, vol. 24, fasc. 8, pp. 1733–1743, ago. 1993, doi: 10.1007/BF02657848.
[37] L. Liu, Y. Tan, Y. Wang, P. Li, e Y. Gao, «Effect of heat treatment on the formation of serrated grain boundary and secondary γ′ phase in a high γ′ phase superalloy», *J. Alloys Compd.*, vol. 1027, p. 180489, mag. 2025, doi: 10.1016/j.jallcom.2025.180489.
[38] A. K. Koul e G. H. Gessinger, «On the mechanism of serrated grain boundary formation in Ni-based superalloys», *Acta Metall.*, vol. 31, fasc. 7, pp. 1061–1069, lug. 1983, doi: 10.1016/0001-6160(83)90202-X.
[39] T. Krol, D. Baither, e E. Nembach, «The formation of precipitate free zones along grain boundaries in a superalloy and the ensuing effects on its plastic deformation», *Acta Mater.*, vol. 52, fasc. 7, pp. 2095–2108, apr. 2004, doi: 10.1016/j.actamat.2004.01.011.